NASA Contractor Report 178059

Near-Field Testing of the 15-Meter Model of the Hoop Column Antenna

Volume I—
Final Technical Report

Martin Marietta Denver Aerospace
Denver, CO 80201

Contract NAS1-18016
March 1986

NASA

National Aeronautics and
Space Administration

Langley Research Center
Hampton, Virginia 23665

UTTL: Near-field testing of the 15-meter model of the hoop column antenna
    TLSP: Final Report
AUTH: A/HOOVER, J.;   B/KEFAUVER, N.;   C/CENCICH, T.;   D/OSBORN, J.;   E/OSMANSKI,
    J.
CORP: Martin Marietta Corp., Denver, Colo.
SAP: Avail: NTIS HC A06/MF A01
CIO: UNITED STATES
MAJS: /*ANTENNA RADIATION PATTERNS/*APERTURES/*HOOP COLUMN ANTENNAS/*LARGE SPACE
    STRUCTURES/*NEAR FIELDS/*PARABOLIC ANTENNAS/*STIFFENING
MINS: / CABLES (ROPES)/ ERROR ANALYSIS/ GOLD/ METRIC PHOTOGRAPHY/ MOLYBDENUM/
    STABILITY/ THEODOLITES/ WIRE CLOTH
ABA: Author

MCR-85-640
Contract No. NAS1-18016

Volume I

Final
Report   March 1986

Technical Report   NEAR-FIELD TESTING OF THE
                                         15-METER MODEL OF THE
                                         HOOP COLUMN ANTENNA

To

NASA Langley Research Center
Antenna and Microwave Research Branch

Authors:

John Hoover
Neill Kefauver
Tom Cencich

Jim Osborn
Program Manager and Author

Joe Osmanski
Manager
Environmental & Test Technologies

MARTIN MARIETTA
DENVER AEROSPACE
P.O. Box 179
Denver, Colorado 80201

N86-29115#

FOREWORD

This report, prepared by Martin Marietta Denver Aerospace, is submitted
to the NASA Langley Research Center, Antenna and Microwave Research
Branch, in response to Contract NAS1-18016, Near-Field Testing of the
15-Meter Model of the Hoop Column Antenna, CDRL Line Item I.D. Our re-
port consists of three volumes:

Volume I   Technical Report

Volume II   Near- and Far-Field Plots for the LaRC Feeds

Volume III   Near- and Far-Field Plots for the JPL Feed

CONTENTS

Figure

Table
_____

GLOSSARY

FFT   Fast Fourier Transformation
JPL   Jet Propulsion Laboratory
LaRC   NASA Langely Research Center
NFTL   Near-Field Test Lab
RF   Radio Frequency
TWT   Traveling Wave Tube

1.0   INTRODUCTION

This report documents the technical results from Contract NAS1-18016 between NASA Langley Research Center and Martin Marietta Denver Aerospace. The contract "Near-Field Testing of the 15-Meter Model of the Hoop Column Antenna" calls for near-field measurements on an uncommonly large scale on this uncommonly large space-deployable antenna. The objectives of this research program are to (1) demonstrate that relatively high-performance deployable antennas can be built and (2) demonstrate that the antenna performance can be accurately measured. Both objectives have been achieved with better-than-expected success.

The antenna is a multiple-aperture reflector with a furlable mesh surface (gold plated molybdenum wire mesh with a grid density of 10 wires/in.). During the program the antenna was tested with feed systems from two organizations--NASA Langley Research Center (LaRC), Hampton, VA, and the Jet Propulsion Laboratory (JPL), Pasadena, CA. Since the amount of information generated during the program is extensive, the report is divided into three volumes. This volume summarizes the testing and contains information to support the two research objectives. Volume II contains a complete set of near- and far-field pattern plots regarding the LaRC set of feeds and is intended for readers interested in detailed test data (Ref 1). Volume III contains similar test data regarding the JPL feeds (Ref 2).

The testing program began with deployment of the 15-meter antenna (49.2 ft) and progressed through a series of measurements to determine mechanical stability, trueness of the reflector surface, and electrical performance. Because the antenna is a semirigid structure, the effect of mechanical resonance on antenna performance is of major importance. Data are presented showing the effects of the two modes of oscillation-- torsional and bending. Three techniques for measuring mechanical tolerance of the surface were used (theodolites, stereo photography, and near-field phase). Trueness of the reflector surface is a major determinant of antenna performance and received much attention during the program. Three methods were used to measure the physical surface; only the near-field phase approach is included in this report (Ref 3).

Most of the information contained in this report is concerned with the near- and far-field performance of the antenna, examining far-field parameters including gain, radiation pattern, and axial ratio. A total of five feed systems were installed in the reflector covering test frequencies of 7.73, 11.60, 2.27, 2.225, and 4.26 GHz. In conjunction with the electrical measurements, an error analysis was performed, and near-field diagnostic methods were used. The diagnostics were performed concurrent with the testing and have been a major factor in the success of this program. Several examples of near-field diagnostics are presented in this report.

As mentioned above, the intent of this report is to present a summary of the measurements, and it is organized to demonstrate key aspects of antenna performance. We have presented a summary error analysis (more detailed version under a separate cover [Ref 4]) to support claims of measurement accuracy. We have not, however, presented the measurement theory which has evolved over a period of years. This theory is both elegant and extensive (Ref 5). It relies heavily on numerical methods and represents a new and powerful tool for analyzing and optimizing antenna performance.

2.0   MEASUREMENT SYSTEM/ANTENNA DESCRIPTION

Both the near-field measurement system and the antenna are unique in size. In the near-field system the scanner is planar, and the aperture fields are measured on an extremely large scan plane. At microwave frequencies, precision mechanisms and mass data handling and processing are basic requirements. To make near-field measurements on such a large scale, a stable transmitter, precision receiving system, laser measurement systems, high speed computers, and efficient algorithms are all needed. The antenna system must be able to control a large reflecting surface to a precision tolerance.

2.1   NEAR-FIELD RANGE

The near-field system is a large scale facility capable of measuring amplitude and phase over a 78x78 ft plane. Maximum antenna diameter is 54 ft, and the operating frequency range is 1 to 18 GHz. Figure 2-1 shows the major components of the system. During the measurements the antenna is mounted on a linearly translatable turntable with the aperture facing upward, transmitting into anechoic material that lines the ceiling and walls. The aperture fields are measured with multiple sampling probes (four open-ended waveguides) transversing across the ceiling. The scan raster is completed by incrementing the turntable after each overhead scan.

Two Hewlett Packard 1000 computer systems are dedicated to the facility. One performs the data collection operations; the second performs the processing operations. Because two operator consoles are available, collection and processing can proceed concurrently after the first collection is complete.

Near-field measurement, transformation, and graphics are shown schematically in Figure 2-2. The test antenna operates in a transmit mode, and the aperture fields are measured with four overhead probes sampled in sequence to give 40 ft of scan for 10 ft of mechanical travel. The scanner mechanism is controlled by one computer responding to keyboard input from the operator. Position and sampling time for each probe are commanded by the computer in response to laser ranging measurements of actual probe position. Overhead scanning provides individual scan lines in a raster completed by incrementing the antenna along a linear way system.

Near-field data processing is under control of the second computer. This allows data processing during data acquisition to support timely viewing of far-field patterns. It eliminates a potentially large backlog of unprocessed data. A hard-wired processor performing the Fast Fourier Transformation (FFT) is the key to low-cost rapid processing of the near-field data array. With this hardware, the HP 1000 can perform the FFT function with the speed of a large-scale, general-purpose computer for a fraction of the cost.

DATA STORAGE
DISK

• • •

TRANSFORM TO
FAR-FIELD DATA

HP 1000   HP 1000

ARRAY
PROCESSOR

CRT &
KEYBOARD
CONTROL

SCAN
CONTROLLER

COLLECT PHASE &
AMPLITUDE DATA IN
THE NEAR-FIELD OF
THE ANTENNA

— NETWORK
   ANALYZER
— RECEIVER

PLOT FAR-FIELD DATA
FOR ANTENNA
CHARACTERIZATION

X-Y PLOTTER
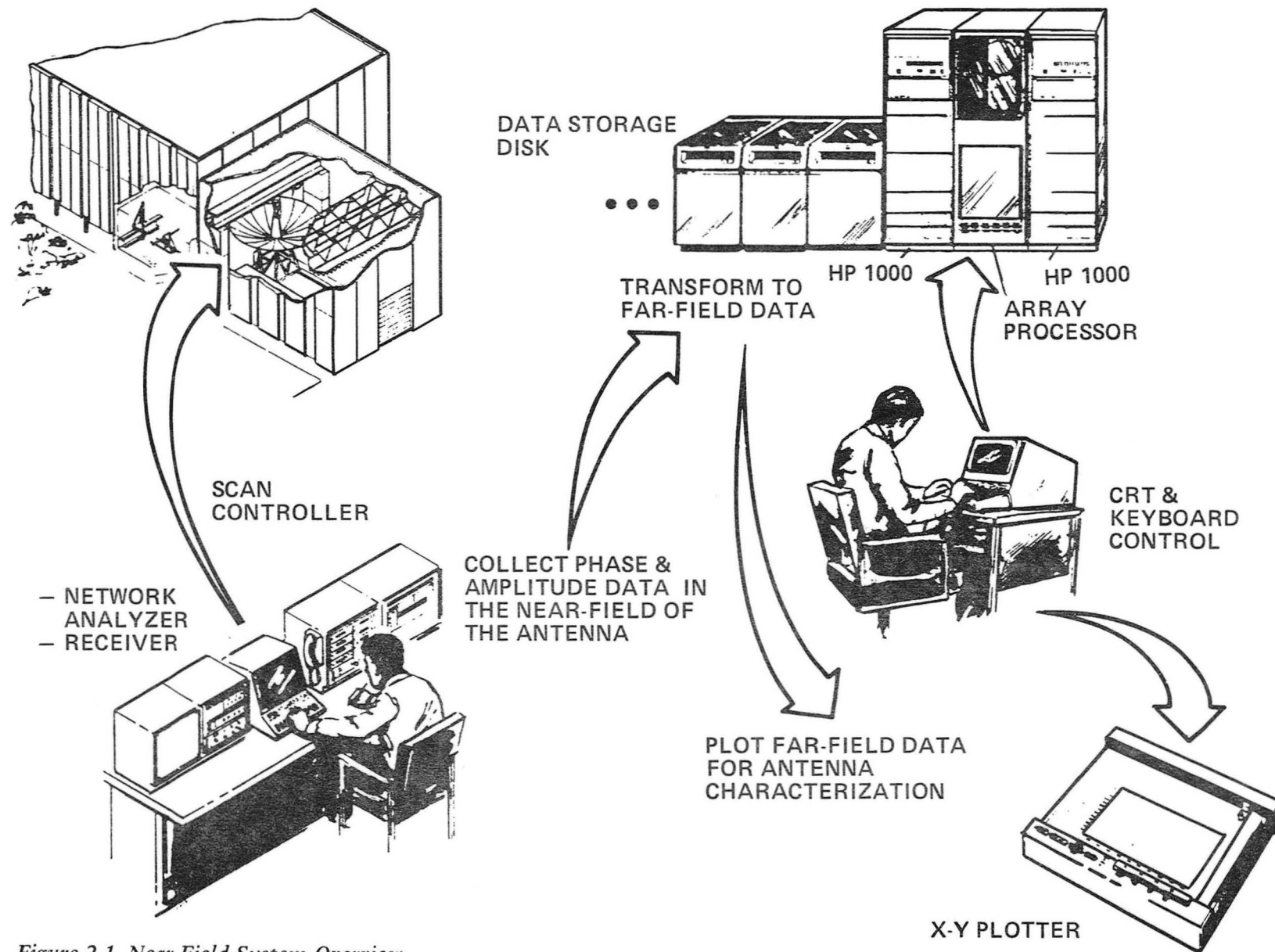
Figure 2-1 Near-Field System Overview
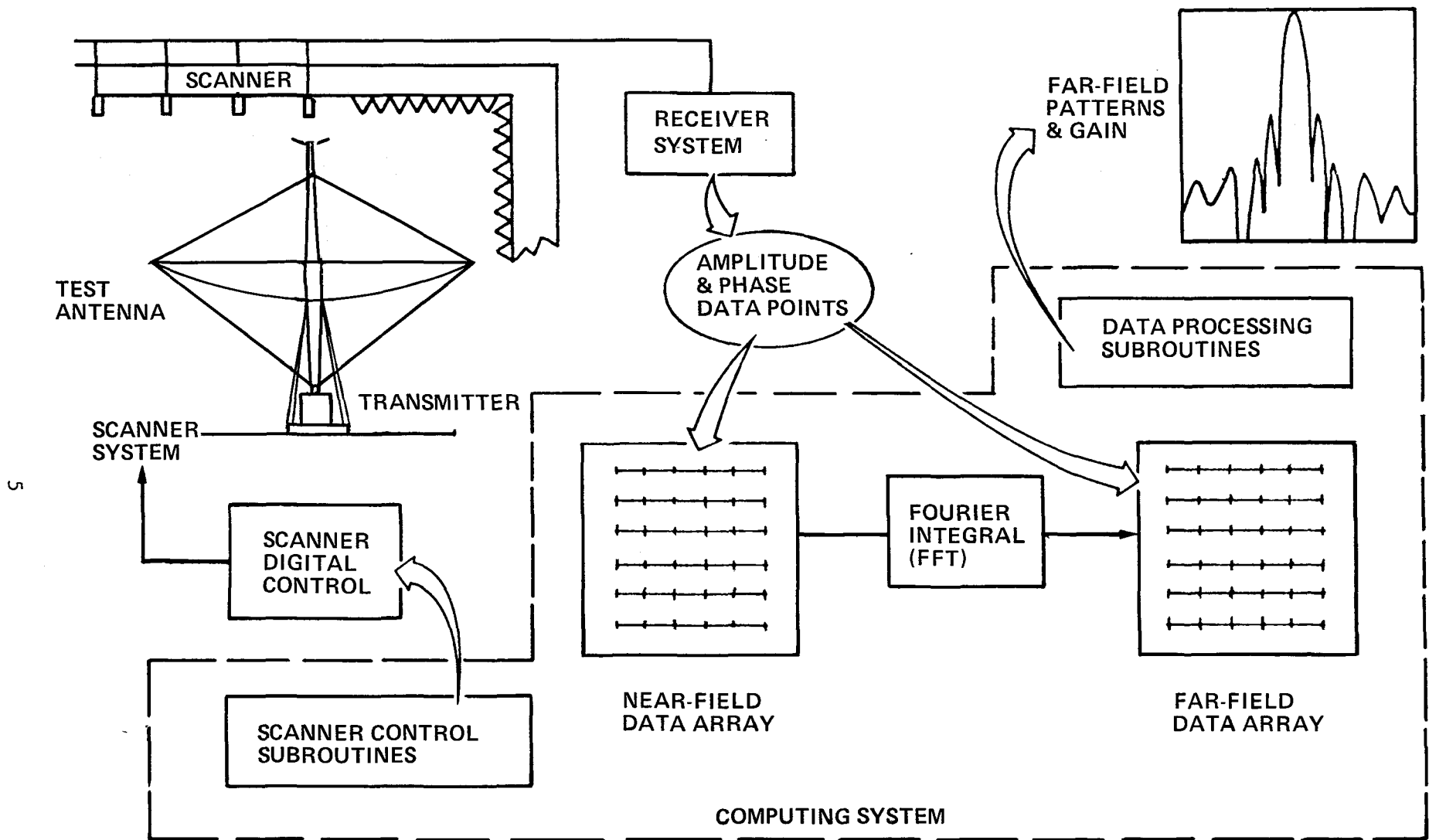
Figure 2-2 *Data Acquisition and Processing*

Both near- and far-field data can be displayed in a variety of formats, including principal plane patterns, contour plots, and 3-D plots. Far-field data are traditionally used to estimate gain, beamwidth, sidelobe levels, boresight angle, cross-polarization, and axial ratio. Near-field data offer new capabilities to directly view phase variations from axial or lateral feed defocusing, extraneous reflections and blockage effects, edge illumination levels, and the resulting diffraction patterns.

2.2   15-METER HOOP COLUMN ANTENNA

The antenna has been named "Hoop Column" after its dominant structural members: a central column supporting a coaxial ring (or hoop). Because both the column and hoop are furlable, the total antenna can be stowed in a minimal configuration. The essential structural elements are illustrated in Figure 2-3. In the deployed configuration, the hoop is supported by quartz cords attached to the top of the column and graphite cords attached to the bottom of the telescoping section. The reflecting surface (gold plated molybdenum wire mesh) is controlled by cord trusses and graphite control cords as illustrated in Figure 2-3. For this test program the entire antenna assembly is supported by a tripod extending from the center of the reflector to an adapter attached to the turntable.

It is important to realize that the reflector is a quad aperture design as opposed to a single paraboloid. With the graphite control cords attached to the ribbing, the reflector is contoured to form four parabolic sections having four focal points offset from the axis as illustrated in Figure 2-3. The purpose of this quad aperture configuration is to generate four interleaving beams for use in multiple beam applications. In its full operational configuration, multiple switched feeds are located at each focal point generating many beams, possibly 100 or more. Since beam steering is involved when the multiple feeds are used, the focal-length-to-diameter ratio is large (approximately 1.5) to minimize coma lobing, an inherent problem in beam steering, by displacing feeds in a parabolic reflector.

Figs. 2-4, 2-5, and 2-6 show the antenna in three successive stages of installation: stowed, partially deployed, and fully deployed. All three photos were taken in the Near-Field Laboratory representing steps in the installation and deployment of the antenna just prior to the near-field measurements.

In the stowed configuration, the hoop segments are folded vertically and are captured by the upper and the lower column hubs. The hoop sections are held secure by conic extensions integral to the hinges between hoop sections. In Figure 2-4, the antenna is shown in the stowed configuration suspended on a hoist ready for installation on the near-field system turntable. In the stowed configuration, the reflecting mesh is entirely contained within the cylinder formed by the vertical hoop segments and upper and lower hubs.

6

FEED

COLUMN

QUARTZ
SUPPORT
CORDS

HOOP

CORD
TRUSSES

REFLECTING
MESH

GRAPHITE
CONTROL
CORDS

FLOOR

TURNTABLE
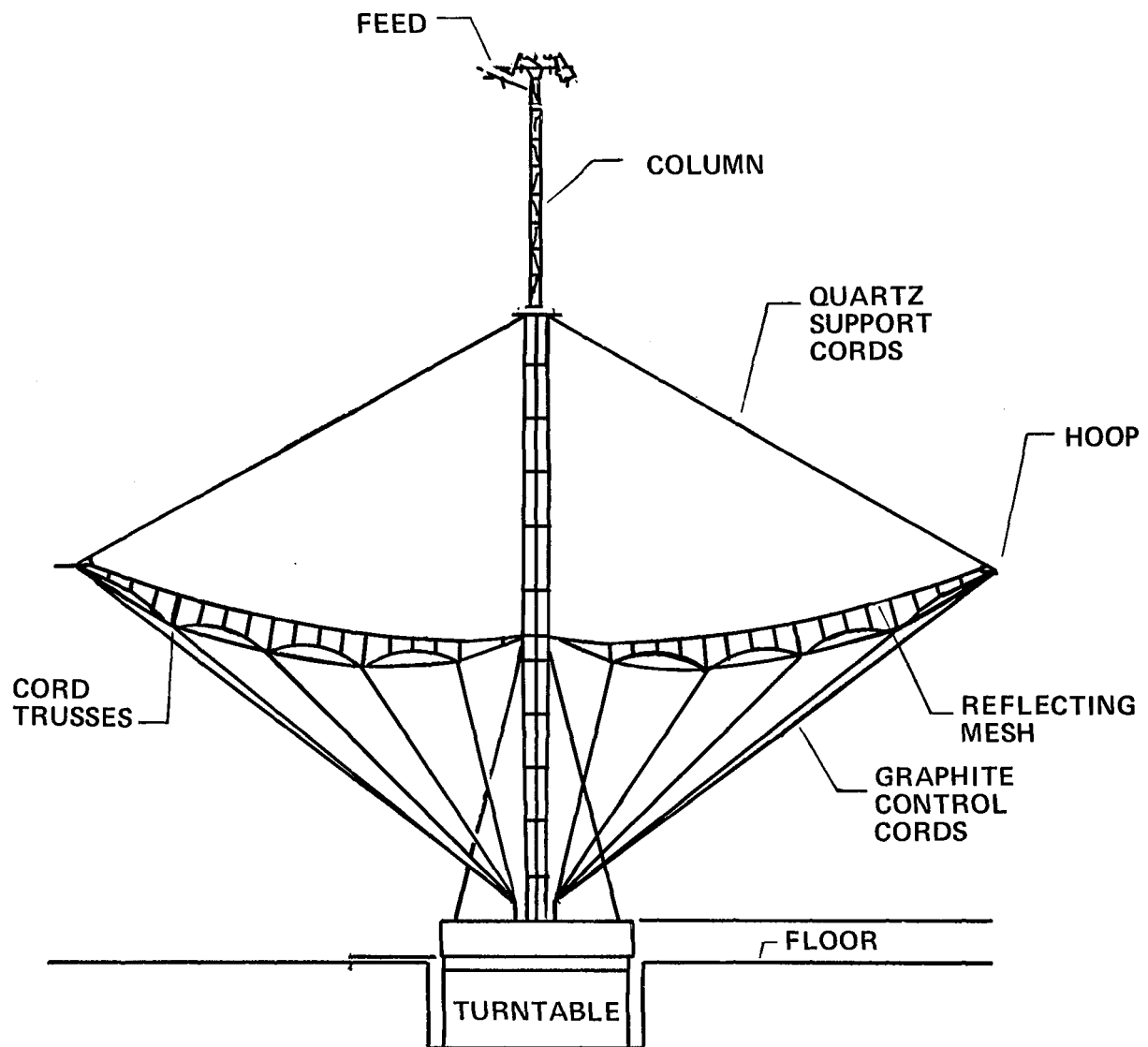
Figure 2-3 Basic Antenna Structure
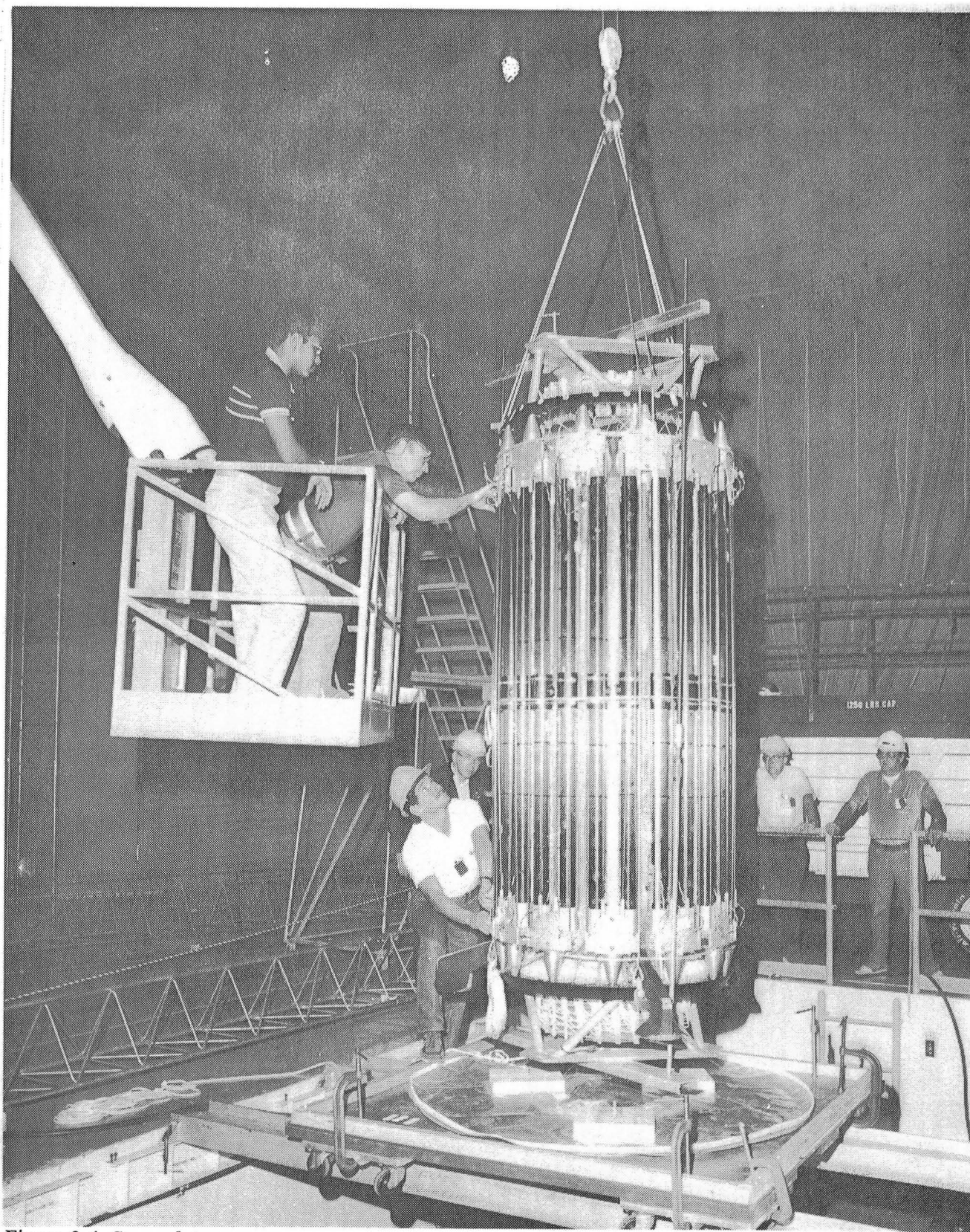
Figure 2-4 Stowed Antenna
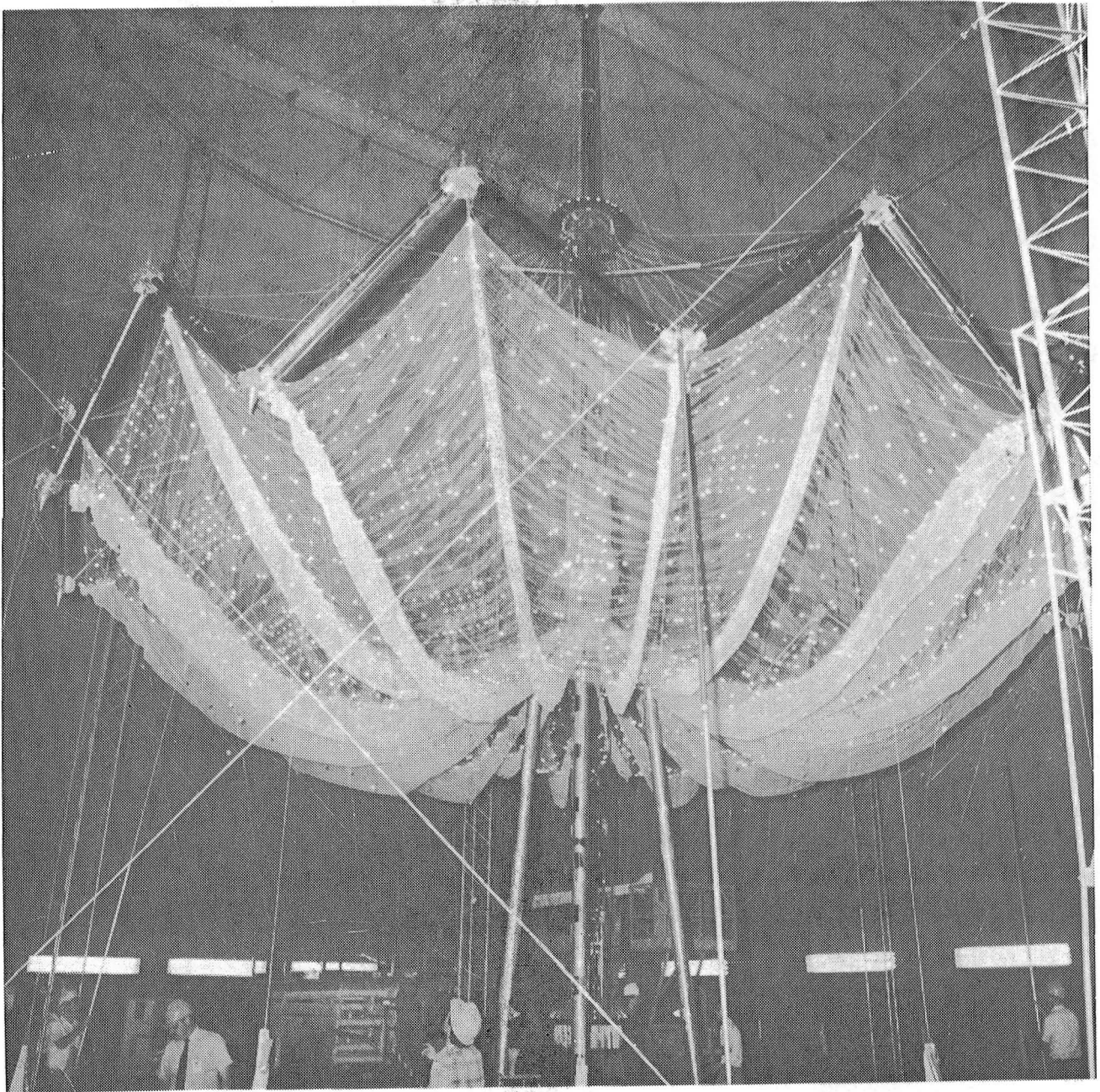
Figure 2-5 Partially Deployed Antenna
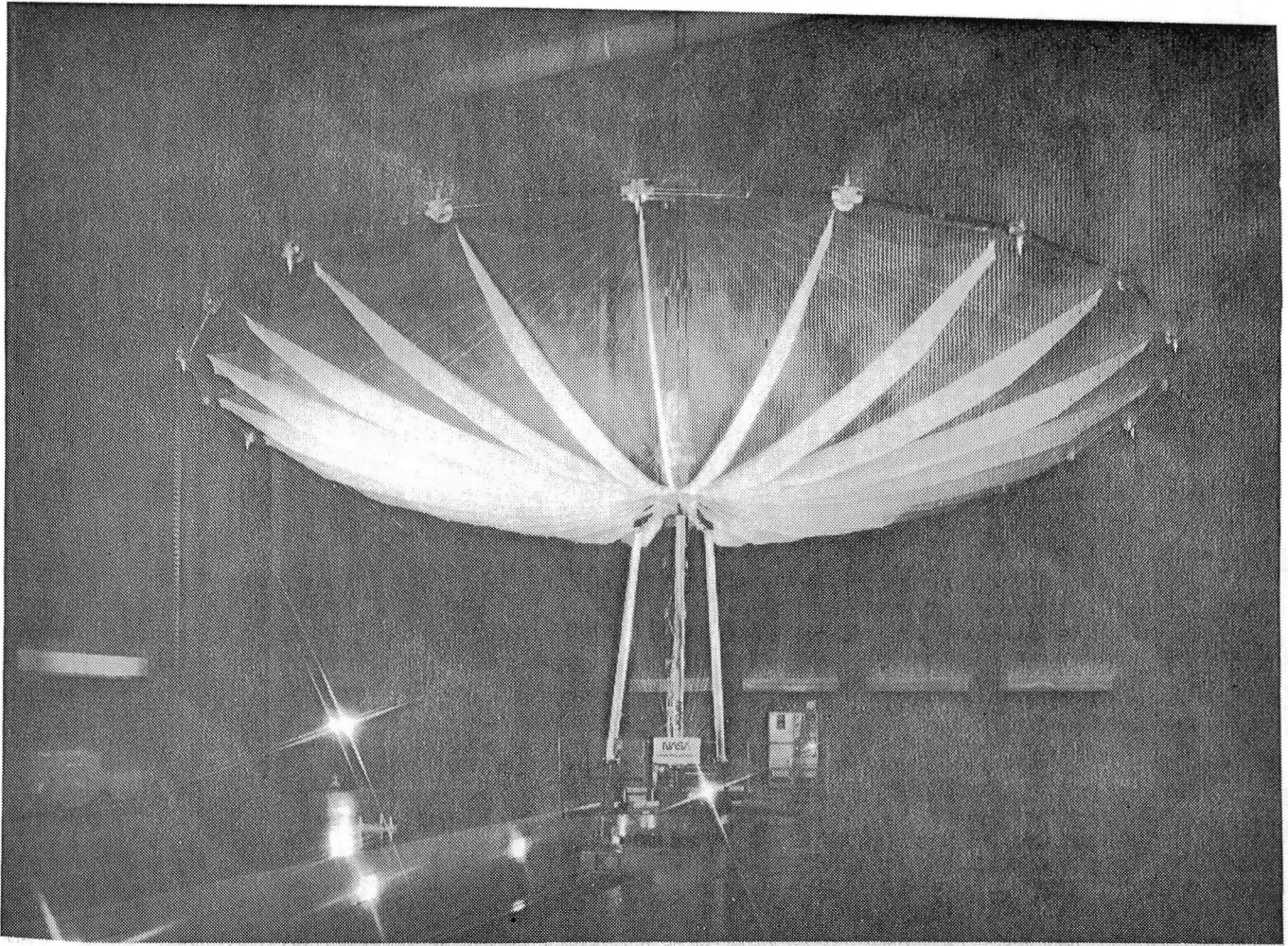
Figure 2-6 Fully Deployed Antenna

In Figure 2-5, the antenna is shown approximately two-thirds deployed. Since the hoop cannot support itself in a 1-g environment, a counterbalance system above the antenna is used in the deployment operations. The counterbalance system is a horizontal ring slightly larger than the antenna, supported by eight towers approximately 47 feet tall. Radial cables extend from a central hub to the counterbalance ring and function as linear tracks for pulleys used to support the hoop with counterweights. The column at this point is fully extended, the end points identified by the hubs mentioned earlier.

Figure 2-6 shows the antenna fully deployed, ready for measurement. The bright spots seen on the reflector are optical targets used in the stereo photography and theodolite measurements. Instrumentation on the turntable includes the transmitter and accelerometer, the latter to monitor acceleration and analyze the mechanical oscillations within the antenna.

3.0   LARGE-SCALE NEAR-FIELD MEASUREMENTS--PRELIMINARY CONSIDERATIONS

In planning the tests and in scheduling the collection/processing oper-
ations, a number of parameters must be defined as inputs to the meas-
urement system before near-field measurements begin. This is particu-
larly true when measurements are made on a large scale.

3.1   NEAR-FIELD MEASUREMENT PARAMETERS AND TIME ESTIMATES

Many parameters define near-field measurements; however, only the most
important ones are discussed here. The most basic parameter (maximum
calculable far-field angle) is defined in Figure 3-1. The maximum far-
field angle is determined by the scan plane size and position relative
to the antenna aperture (Ref 4) as follows:

$$\theta \simeq \tan^{-1} [(L - D)/2d]$$

Where

L = Scan length,
D = Antenna diameter,
d = Antenna-to-scan plane separation.

For this program L = 78 ft, D = 49.2 ft, d = 31.2 ft and θ = 24°.

Given the maximum scan length of 78 ft, the near-field measurement and
processing times are determined by the operating frequency. Given fre-
quencies of 7.73, 11.60, 2.27, 2.225, and 4.26 GHz, the most signifi-
cant parameters are those listed in Table 3-1. The first parameter in
the table, sample spacing, is normally one-half of the free space wave-
length at the given operating frequency. Near-field scan size is de-
termined by the physical scanner--in this case 78x78 ft, the maximum
available. Given the scan size and sample spacing, the near-field data
array is identified. Since the FFT algorithm calls for array sizes
equal to a power of two on a side, the array is appropriately zero
filled as one of the many processing operations (Ref 6). The scan
times listed are based on a collection rate of 112 scan lines/h, given
the array size and using the quadrant scan mode for the near-field sys-
tem. In this mode the near-field scan plane is divided into four equal
parts (quadrants) for data collection purposes. The processing times
are based on the array size and the computational rate of the FFT as
applied to the local computer system. The maximum far-field angle is
derived from Figure 3-1.
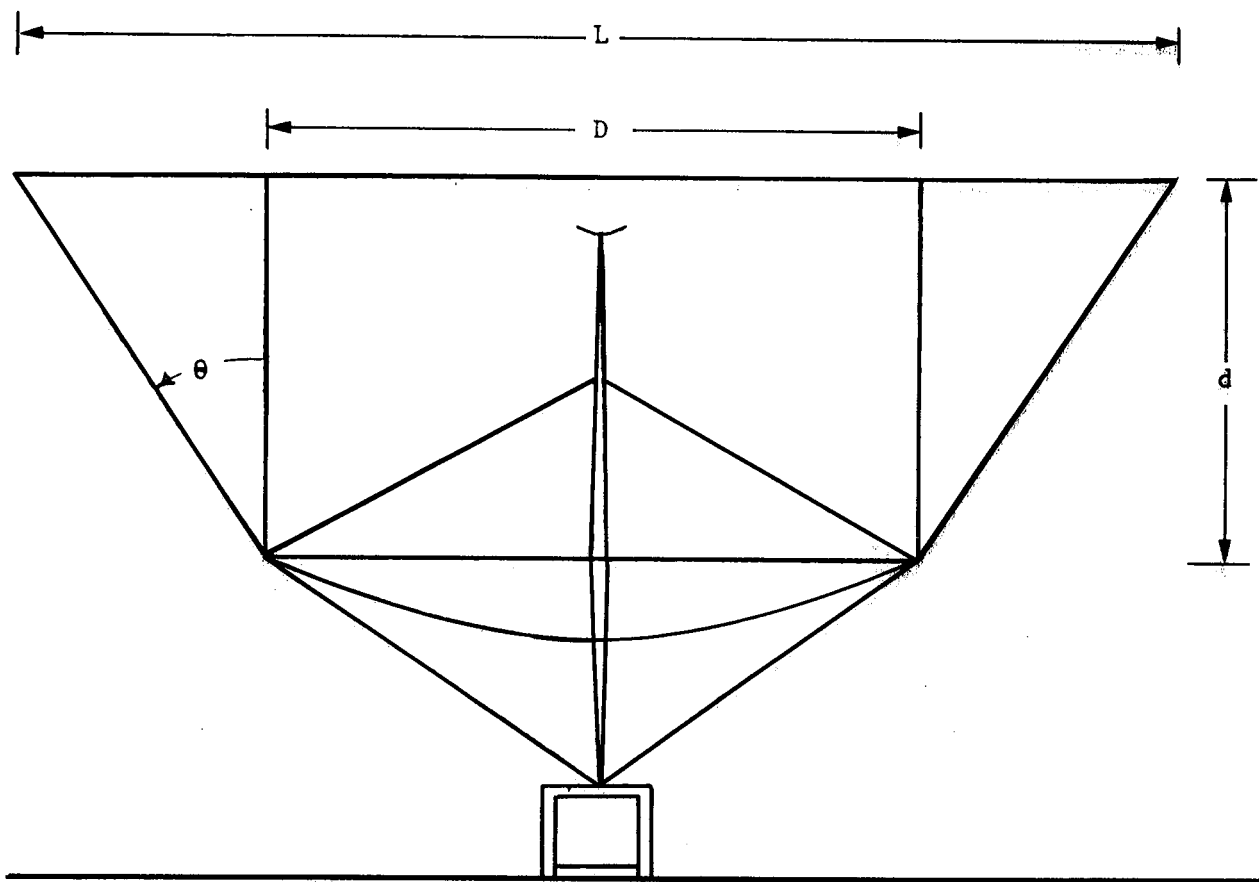
Figure 3-1 Maximum Far-Field Angle Definition

Table 3-1   Measurement Parameter Summary

Measurement Parameter	Frequency, GHz				
	2.225	2.27	4.26	7.73	11.60
Sample Spacing, in.	2.65	2.60	1.38	0.76	0.49
NF Scan Size, ft by ft	78x78	78x78	78x78	78x78	78x78
NF Array Size, Points by Points	353x353	360x360	687x687	1282x1282	1912x1912
Zero Filled Array, Points by Points	512x512	512x512	1024x1024	2048x2048	2048x2048
Scan Time, h	7.0	7.0	12.0	23.0	34.0
FFT Time, h	0.33	0.33	0.75	3.0	3.0
Maximum Far-Field Angle, °	24.0	24.0	24.0	24.0	24.0

Table 3-2(a) gives the approximate time necessary to configure the lab for each measurement frequency. Preparation consists of installing the instrumentation, primarily the transmitter, receiver, and sampling probes. Also, it is necessary to install coaxial and waveguide plumbing (some of which invariably must be fabricated) and adjust all of the micro- wave power levels to their optimum operating points. RF "clean up" is a necessary step to ensure that:

1) All cables and connections are sound, and

2) The transmitter (traveling wave tube [TWT] driven by a frequency syn- thesizer) portion of the facility does not "leak" a significant amount of radio frequency (RF) energy, which appears as a contaminant in the measured near-field data.

Table 3-2 Total Test Time Estimates

Activity	Frequency, GHz			
	2.27 or 2.225	4.26	7.73	11.60
Preparation	8	8	8	8
RF Cleanup	8	8	8	8
Total Prep	16	16	16	16
(a) Lab Preparation for Each Frequency, h				
Probe Balance	2.00	2	2	2
Scan Time	7.00	12	23	34
Probe Rotation	2.00	2	2	2
Insertion Loss	2.00	2	2	2
Total Collection	13.00	18	29	40
FFT	0.33	0.75	3	3
Other Processing	3.00	4.00	7	7
Plotting	1.00	1.00	1	1
Total	17.33	23.75	40	51
(b) Data Collection, Processing and Plotting, h				

Table 3-2(b) shows test, processing, and plotting times, based on experience allowing for routine delays. Probe balance is a process to ensure that each of the four separate probe antennas output an identical complex terminal voltage for identical incident fields. Scan time is based on the facility maximum collection speed and includes periodic drift checking and periodic near-field scan line plotting to confirm valid measurements. This speed is 112 lines/h, less for lower frequencies due to a longer step distance and acceleration constraints on moving the antenna. This speed includes the delay (long enough to allow the oscillation to subside) inserted after each x-axis step, which increases the total time approximately 25%.

Probe rotation is needed to align the probe's polarization vectors with the antenna's when measuring Quadrants 2 and 4 after measuring Quadrants 1 and 3 (Ref Sect. 4.1 [Fig. 4-1]). Insertion loss is a step to establish an absolute gain calculation.

In addition, experience shows that an average of one day per week must be reserved for near-field system maintenance and unscheduled problem solving for newly developed antennas. The developmental nature of the testing of the NASA Langley hoop column antenna suggested no exception to this rule. Therefore, a realistic multiplier of 1.25 is used to obtain the final time requirement estimate in Table 3-2(b).

3.2   ERROR ANALYSIS

Many near-field error sources contribute to far-field pattern and gain inaccuracy; however, the two most prominent errors are (1) probe z-position or nonplanarity (distance measured normal to a perfect scan plane), and (2) chamber reflections (Ref 5 and 6). We restricted the analysis, therefore, to the maximum error in the far-field pattern associated with these two error sources.

Probe z-position error is the mechanical deviation of the near-field probe relative to an ideal scan plane. It is primarily caused by small nonlinearities in the roundways supporting the probe carriage. These errors appear as artificial modulations of the near-field phase, which, in turn, generate nonexistent sidelobes in the far-field pattern. The level and position of these sidelobes with respect to the main beam depend upon the specific z-position error of the probe as a function of x and y position over the antenna's aperture and frequency of operation of the antenna and near-field system. However, the far-field envelope describing the peaks of the sidelobes depends only on frequency. Using 78 ft of scan and the test frequencies for this program, the peak error envelope in the far-field is plotted in Figure 3-2 normalized to the mainbeam maximum. To assess the error contribution to the 15-Meter Hoop Column Antenna measurements, the antenna's far-field pattern (also on a normalized scale) is superimposed on the same plot. Because the far-field patterns are not available at this point in the report, the comparisons are deferred to Section 5.5, Error Analysis. The amplitude difference between the error envelope and any computed sidelobe may be used to calculate the maximum possible inaccuracy in the computed sidelobe due to probe nonplanarity. This difference tends toward the 15- to 20-dB range indicating maximum possible sidelobe peak inaccuracies from ± 1 to ± 1.75 dB.
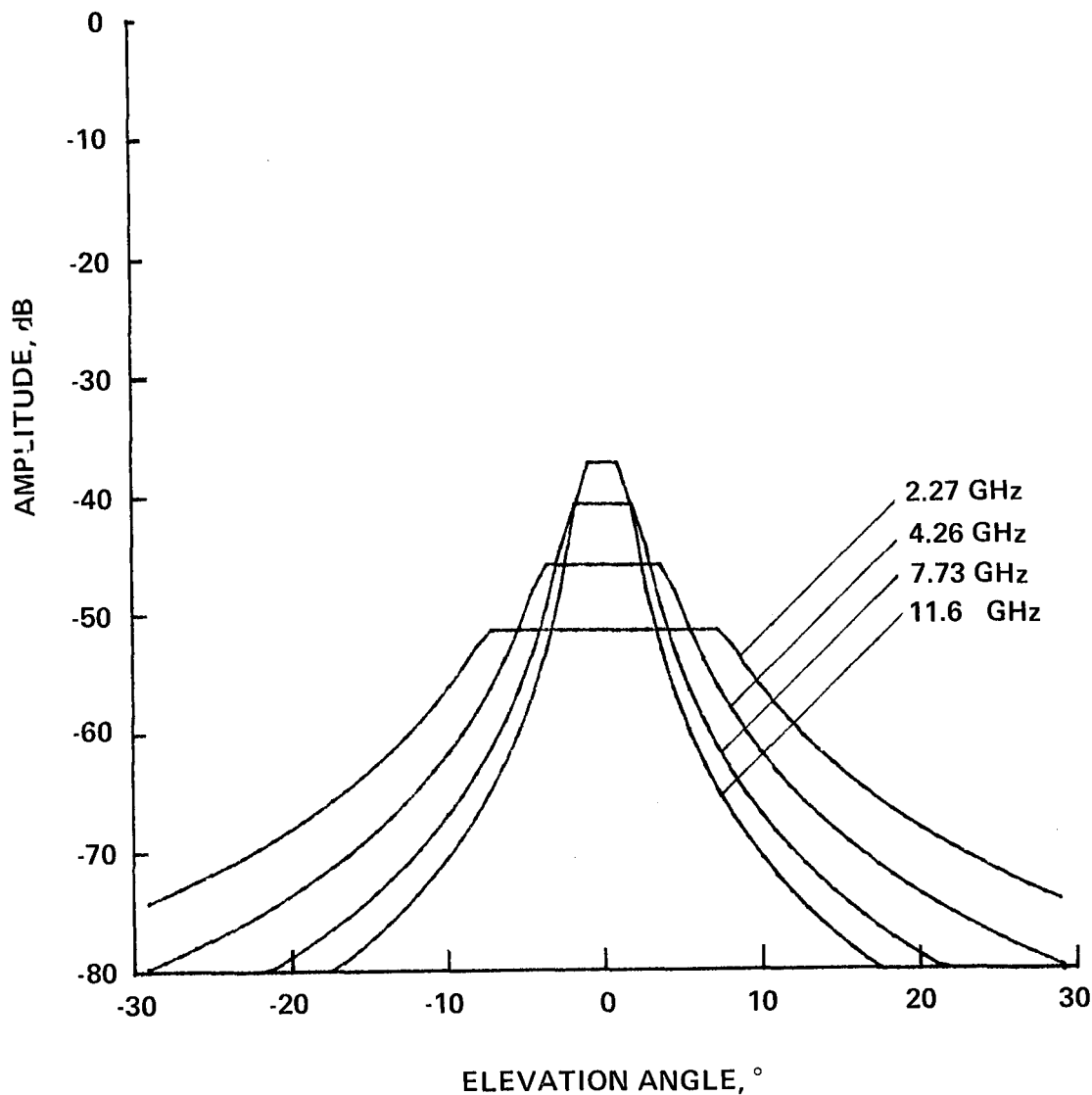
Figure 3-2 Probe Position Error Envelopes

Chamber reflections, present in any indoor antenna pattern measurement, represent the second dominant accuracy limitation to low sidelobe measurement. In discussing the effect of chamber reflections on the far-field pattern, two types of reflections should be recognized: specular and diffuse (referred to as isotropic). Because the ceiling and near-field scan plane are parallel to the antenna's near-field plane wave component generating the main beam, the specular component of reflection occurs in the far-field pattern coincident with the main beam. Hence, specular reflection has a slight effect on boresight gain measurement accuracy, but it does not contribute to sidelobe error. In contrast, the isotropically scattered reflection component does impose a far-field pattern sidelobe measurement limit. However, because it is isotropic scattering, its level in the far-field pattern is relative to the isotropic level of the antenna being measured. As the gain of the measured antenna increases, so does the far-field dynamic measurement range attributable to isotropic chamber reflection. The far-field measurement limit is the -15-dBi level of the measured antenna, regardless of size or frequency. Error levels for reflections have been included in the far-field plots in Section 5.5.

15

Significant errors in determining the boresight gain (Ref 7) are the following:

1) Probe position error,

2) Accuracy in measurement of insertion loss (defined to be the loss between the test antenna input terminal and the input to the receiver including impedance mismatches),

3) Tolerance on probe gain. (See Appendix C.)

For reference, the error contributions from these sources are tabulated in Table 3-3. For the on-axis gain error the contribution from probe position is taken from Yaghjian's upper-bound analysis using a maximum z-directed position error of 0.020 in. (Ref 8). This estimate is an upper-bound calculation, so the actual gain inaccuracy due to this mechanism is probably much less. The insertion loss uncertainity, the second listed contributor to gain inaccuracy, reflects both RF mate/demate repeatability and uncertainity in the attenuators used. The final listed contributor, probe gain uncertainity, arises from the error potentially generated in the measurement of absolute gain of the open-ended waveguide antennas used to probe the near-field. It contains both mate/demate repeatability and uncertainity of the absolute gain of the antenna used as a reference. The total gain inaccuracy is obtained by the RSS sum of each of the contributors in the bottom row.

Table 3-3 Antenna Gain Errors

Error Parameters	Frequency, GHz			
	2.27 & 2.225	4.26	7.73	11.60
Probe Positioner Error, dB	$\pm$0.003	$\pm$0.01	$\pm$0.03	$\pm$0.07
Insertion Loss Measurement Accuracy, dB	$\pm$0.10	$\pm$0.15	$\pm$0.20	$\pm$0.25
Tolerance on Probe Gain, dB	$\pm$0.10	$\pm$0.10	$\pm$0.10	$\pm$0.10
Total Gain Accuracy RSS, dB	$\pm$0.14	$\pm$0.18	$\pm$0.23	$\pm$0.28

4.0   TEST PLAN

The near-field tests were organized by priority with the most signifi-
cant at the beginning, the total test program consisting of 34 far-
field pattern measurements. Gain measurements were made at each fre-
quency but not each test. The frequencies (7.73, 11.60, 2.27, 2.225
and 4.26 GHz) are listed in Table 4-1 with associated information to
define the antenna configuration, polarization, beamscan and array size.

The tests began with 7.73 GHz, assumed to be the highest frequency for
which high performance could reasonably be expected from the antenna.
Before beginning the tests, NASA adjusted the surface using the 96 rear
control cords until the antenna surface was acceptable. The next fre-
quency (11.6 GHz) was selected to measure far-field pattern deteriora-
tion as the frequency is increased. Just before Test 18 the mesh sur-
face was readjusted in an attempt to refine it to its best possible
state.

The test program used two scan modes, referred to as: 1) quadrant scan
and 2) abbreviated scan. In the quadrant mode (not to be confused with
the quad apertures in the antenna) the scan plane was divided into four
equal parts, later combined in the processing with an algorithm named
"reformat." Figure 4-1 illustrates the quadrant scan mode. It shows
the antenna relative to the scan plane for the four quadrants. In
Figure 4-2 the scan planes are combined to show the final effective
scan relative to the antenna aperture.

Figure 4-3 shows the abbreviated scan relative to the antenna aper-
ture. In this case the scan is one-fourth the size of the previous
quadrant mode, reducing the scan time by about 80%. However, a penalty
is imposed on the far-field patterns generated from this type of scan.
It is valid for the main beam and first few sidelobes as opposed to
$\pm 24°$ for the quadrant mode. The abbreviated scan is most useful when
wide angles are not required. In the test plan in Table 4-1, Tests 11e
through 11h and 18 through 26 use the abbreviated scan; all others use
the quadrant mode.

ANTENNA APERTURE

ACTIVE QUADRANT

PROBE POLARIZATION

SCAN PLANE

QUAD 1

QUAD 3

QUAD 2

QUAD 4
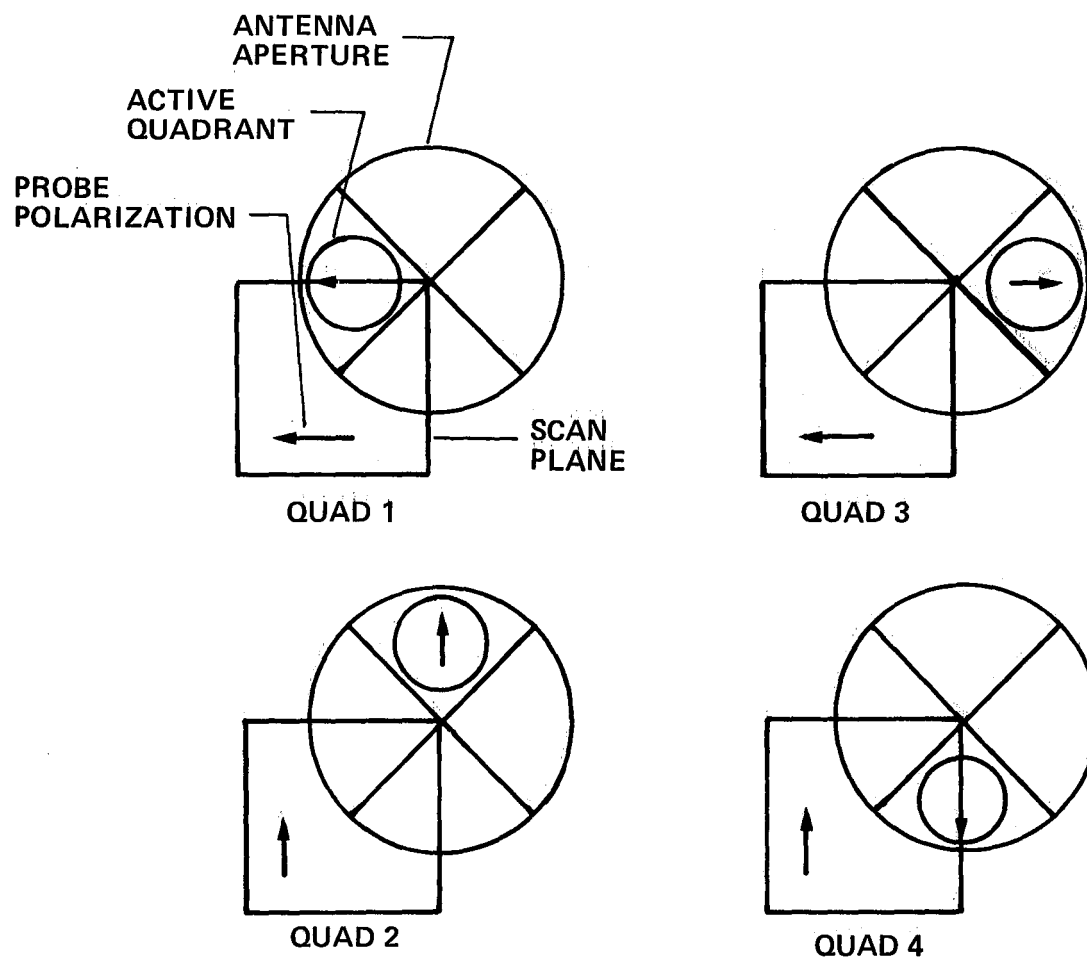
Figure 4-1 Quadrant Scan Mode

ILLUMINATED QUADRANT

QUAD 4

QUAD 3

QUAD 1

QUAD 2

TEST ANTENNA'S
COORDINATE SYSTEM
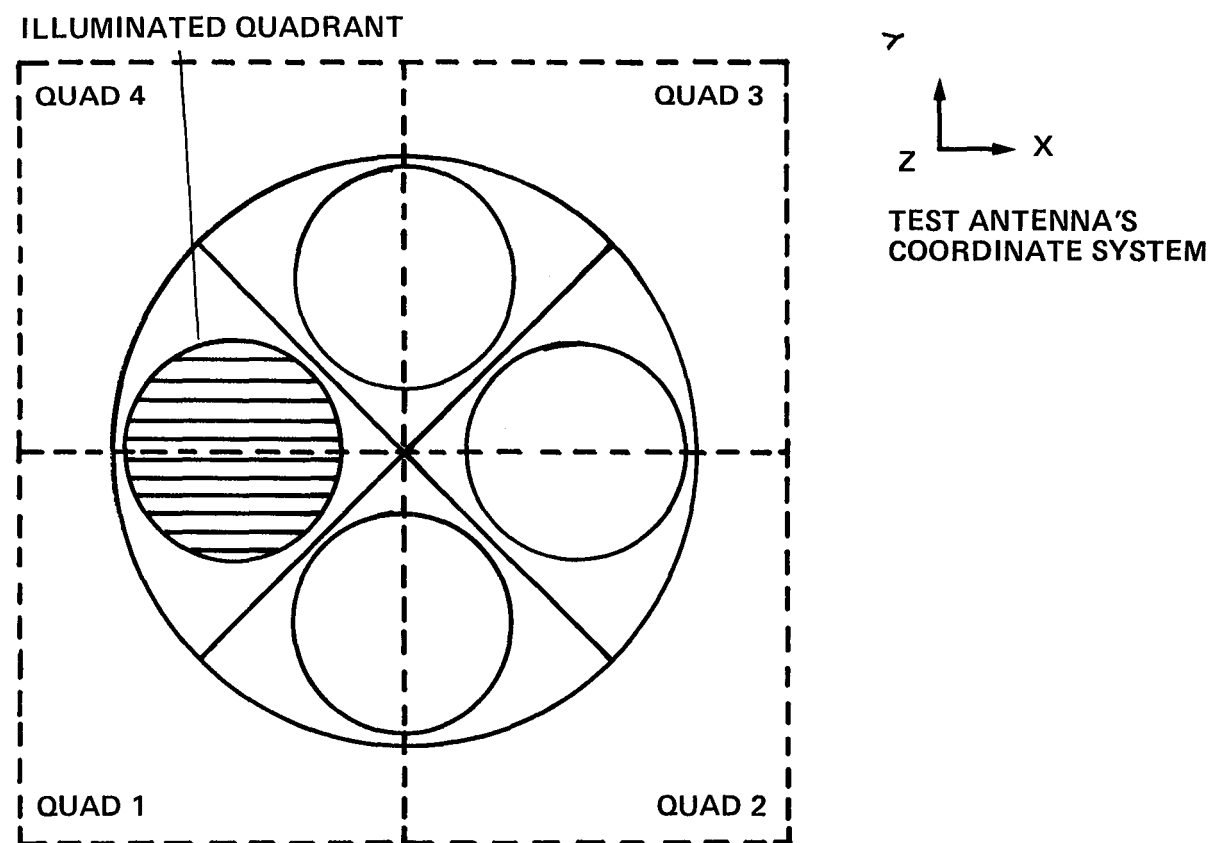
Figure 4-2 Complete Near-Field Scan with Quadrants Reformatted

ANTENNA
APERTURE

PROBE
POLARIZATION

ACTIVE APERTURE

SCAN PLANE
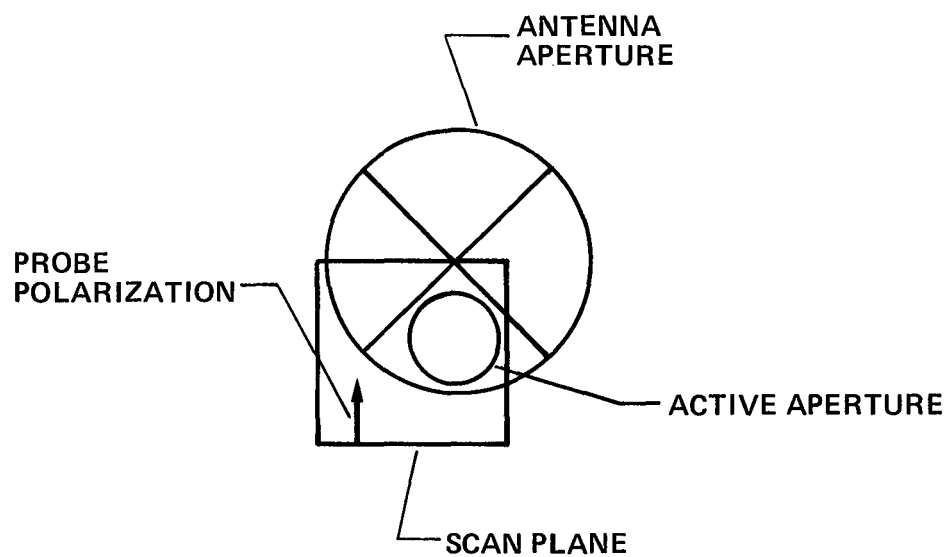
Figure 4-3 Abbreviated Scan Mode

Table 4-1   Test Plan

Test	Freq GHz	Feed Pos	Collection Polarization	Far-Field Polarization	Illum Quad	Beamscan, Beamwidths	Scan Size, Data Points
1	7.73	1	East*	Co	4	0	2048 x 2048
2	7.73	1	North	Cross	4	0	2048 x 2048
3	7.73	11	East	Co	4	6	2048 x 2048
4	11.60	1	East	Co	4	0	2048 x 2048
5	2.27	1	East	Co	4	0	512 x 512
6	2.27	1	North	Cross	4	0	512 x 512
7	2.27	2	East	Co	2	1	512 x 512
8	2.225	8	East	Cross	4	0	512 x 512
9	2.225	8	North	Co	4	0	512 x 512
10	2.225	2	East	Cross	4	2	512 x 512
11	2.225	2	North	Co	4	2	512 x 512
11a	2.225	4	East	Cross	4	1	512 x 512
11b	2.225	4	North	Co	4	1	512 x 512
11c	2.225	5	East	Cross	4	1	512 x 512
11d	2.225	5	North	Co	4	1	512 x 512
11e	2.225	8	East	Cross	4	0	512 x 512¶
11f	2.225	8	North	Co	4	0	512 x 512¶
11g	2.225	2	East	Cross	4	2	512 x 512¶
11h	2.225	2	North	Co	4	2	512 x 512¶
12	4.26	1	East	Co	4	0	1024 x 1024
13	4.26	8	East	Co	2	2	1024 x 1024
14	4.26	11	East	Co	4	6	1024 x 1024
15	4.26	1	East	Co	2	0	1024 x 1024
16	4.26	2	East	Co	2	1	1024 x 1024
17	4.26	3	East	Co	2	-1	1024 x 1024
18	7.73	1	East	Co	4	0	512 x 512¶
19§	7.73	1	East	Co	4	0	512 x 512¶
20§	7.73	1	East	Co	2	0	512 x 512¶
21§	7.73	1	East	Co	3	0	512 x 512¶
22§	7.73	1	East	Co	1	0	512 x 512¶
23§	7.73	1	North	Cross	4	0	512 x 512¶
24§	7.73	1	East	Co	4	0	512 x 512¶
25§	11.60	1	East	Co	4	0	1024 x 1024¶
26§	11.60	1	North	Cross	4	0	1024 x 1024¶

*   "X" in Figure 5.1 Corresponds to east in the Near-Field Laboratory.
§   After Final Cord Adjustment
¶   Abbreviated Scans

5.0 TEST RESULTS

In the test plan in Table 4-1, the far-field patterns and gain of the antenna were measured at five frequencies--2.225, 2.27, 4.26, 7.73, and 11.60 GHz, beginning with 7.73 GHz. For the near-field scanning, both the quadrant and abbreviated modes were used as indicated in Table 4-1. For the pattern plots in this section, we refer the far-field components and angles to the coordinate system shown in Figure 5-1. In this figure, the near-field components are identified by two vectors, E_x and E_y. After transformation into the far-field the components are identified as A_{az} and A_{el} on a sphere defined by an azimuth and elevation coordinate system. In these coordinates, the far-field patterns are referenced to the antenna by placing its vertex in the x, y plane with the active aperture and its co-polarized field vector aligned with the negative x-axis. In the far-field pattern plots that follow, the E-plane and H-plane correspond to azimuth and elevation planes, respectively. To align antenna polarization relative to the scanner, the feed was first centered on the column using a remote feed positioning system. Next the feed was aligned with the optical target in the center of the active quadrant. Following this, the antenna was aligned in the co-polarized direction with the scanner probes by theodolite sighting through the vertical plane containing the four scanner probes, Hoop Point 19, and the cord along this joint.

5.1 INITIAL ADJUSTMENTS (SURFACE AND FOCUSING)

After the antenna was deployed, the reflector surface was precisely adjusted by making small length changes in the control cords located on the back of the reflector. The adjustments were based on metric camera measurements taken before the antenna arrived at the Near-Field Test Lab (NFTL). After adjustment, metric photos were taken to measure surface trueness. After installation and alignment of the 7.73 GHz feed, Test 1 focus scans began. Based on signal near-field scans through the center of the aperture and near-field phase maps discussed in Section 5.4.3, it was determined that the surface needed further adjustment. In reality, a cord had been improperly adjusted in the above sequence. Concurrently, the same conclusion was reached based on results from the metric camera measurements. With information from the metric camera analysis, the surface was again adjusted, a total of 10 cordlengths being changed. After this adjustment (referred to as the 10-cord adjustment), near-field scans showed that the surface was acceptable for testing; this was the final adjustment for Tests 1 through 18. Feed changes and alignments were made during the tests, but no surface adjustments were made. After Test 18, a final adjustment was made, and the surface was again photographed. The objective of this final adjustment was to refine the surface to its best possible state for this antenna. The test data contained in following paragraphs show that improvement was achieved.

Each frequency used a separate feed. The antenna was configured prior to each test frequency by first installing the appropriate feed system. At the two highest frequencies (7.73 and 11.60 GHz), the feeds were conical horns; at all others they were microstrip patch subarrays generating a single beam in an eventual array of many beams. After the feed was installed, near-field diagnostic methods focused and aligned the feed. For these methods, the near-field amplitude and phase are measured across the center of the aperture by scanning across a center line. By observing the phase plots from two orthogonal centerlines, the feed is positioned for optimum reflector performance. Two centerline plots for Test 1 (7.73 GHz) are shown in Figure 5-2 and 5-3. Both were recorded after the focusing operations. In the figures, units are either amplitude in dB or phase in degrees plotted versus row and column number in the near-field data array. The widths of the plots are selected to approximately correspond to the physical dimensions of the active quadrant of the antenna.

In the focusing operation, lateral feed displacement gives a phase slope across the active aperture, while axial displacement gives a pseudo quadratic phase error appearing as bending in the phase plot. Both plots shown are after the focusing operation and represent best phase for the antenna. In the E-plane the total phase variation across the active aperture is approximately $\pm30°$. In the H-plane it is $\pm45°$. In the H-plane the phase is plotted across the reflector ribbing, the less precise of the two principal planes.

5.2   ANTENNA RADIATION PATTERNS

During this program a great many near- and far-field patterns were recorded--too numerous to be included in this volume. The following figures are selected plots that demonstrate essential antenna performance. The patterns follow the sequence in the test plan; however, several of the tests have been omitted. Refer to Volumes II and III for the complete set of recordings.

The first radiation pattern comes from Test 1, recorded after the 10-cord surface adjustment and feed alignment. In Figure 5-4, the far-field pattern is recorded over an 80-dB dynamic range versus azimuth angle over a $\pm30°$ sector. Azimuth angle corresponds to the E-plane, and the plot is for the principal (or co-polarized) field component plotted through the peak of the main beam.

As a first observation, the first two sidelobes are slightly more than 20 dB below the peak of the main beam. This represents high performance from the antenna and suggests that it could be used for many spaceborne applications. It will be shown later that the first sidelobe level is determined by the trueness of the mesh surface, and that the first sidelobe level for a perfect paraboloid is approximately 40 dB below the main beam peak.

A second major lobe occurs at the -32-dB level at approximately 6° azimuth. It is caused by illumination of the opposite quadrant as demonstrated in the diagnostics discussed later. Although the level of this lobe is relatively low, it could be further suppressed by reducing the illumination of the opposite quadrant.

The next important conclusion, although not apparent in the plot, concerns the mechanical stability of the antenna. The fully deployed configuration has two fundamental modes of oscillation--torsional (or rotational) and bending. During the near-field measurements these modes are being excited by air flow within the scanner room and by physical translation during the stepping operations in the near-field scanner. Mechanical motion from these two sources was not visible to the naked eye but is easily detectable when observed with a theodolite. Modes excited from the stepping operations are partially damped during the time elapsed between scans; however, those excited by air flow are continuous. Total antenna motion from oscillations as viewed on the hoop and at the top of the column were approximately +0.1 inches for Test 1. The diagnostic methods discussed later examined the effects of this in both the near- and far-field results. In the plot in Figure 5-4, oscillation within the antenna caused no measurable error within the main beam and first few sidelobes. On a test-to-test basis, these higher level elements of the pattern are highly repeatable. Mechanical oscillations within the antenna do, however, appear as pseudorandom errors in the wide-angle, low-level sidelobes. Referring to Figure 5-4, sidelobes below approximately -50 dB and at angles greater than +8° do not repeat on a test-to-test basis. Conceptually, mechanical motion within the antenna causes the low-level, wide-angle sidelobes to continually shift in angle and level but contributes little or no error to the main beam and principal sidelobes.

Figure 5-5 plots the far-field versus elevation angle (H-plane) for Test 1. Similar to the previous plot, the first sidelobe level is below the -20 dB level, slightly lower than the previous E-plane plot. One primary difference in the two patterns is apparent in the lobe structure. In this principal plane, the pattern is plotted across the ribbing of the antenna which induces a periodic mechanical error in the reflecting surface. Again, from the diagnostic methods used, the periodicity in the surface produces grating lobes not apparent in the previous E-plane plot. These lobes occur principally at the -30 dB level and at approximately +5° in elevation. While these lobes present no physical problem or concern, the mechanism for reducing them is to reduce or eliminate periodicity in the antenna structure. With respect to oscillation with the antenna, comments from the previous section also apply to the H-plane radiation pattern.

Figures 5-6 and 5-7 plot the far-field for the two planes diagonal to the E- and H-plane, referred to as the -45° and 45° diagonals. Some grating lobes are apparent in these two plots; however, the major departure from the previous plots occurs in Figure 5-7. Here the first sidelobe has increased to approximately the -17-dB level, a surface effect appearing in this plane. This increase in sidelobe level was the prime consideration for Tests 18 through 26. In these tests the surface was readjusted to minimize surface errors, and the results are presented later in this section.

When the near-field data are transformed into the far-field, pattern information is known and available over a solid angle. Contour and 3-D plot routines can show the far-field pattern in its entirety. In Figure 5-8 the far-field is contour plotted over $\pm 6°$ shaded at 10-dB levels from the beam peak to a -40 dB in 10-dB increments. Starting with beam peak (angle 0,0) it is shown from 0 to -10 dB. From -10 to -20 dB the first sidelobe structure becomes apparent. The dominant features are the higher lobes and negative-to-positive diagonal. In the section on diagnostics the antenna aperture is separated by quadrant to show the essential features on the contour plot associated with each quadrant. For example, the opposite quadrant generates the lobe at angle (6,0) at level -30 to -40 dB (darkest shading). Lobes associated with the adjacent quadrants can also be identified using this method. See Section 5.4.3.

In Figure 5-9, the far-field pattern is plotted in three dimensions over $\pm 5°$ in the azimuth, elevation coordinate system. Constant level contours at 10-dB increments have been superimposed on the plot to enhance it quantitatively. The first sidelobes above the 20-dB level in the diagonal plane previously referenced are apparent. For the aspect angle used, however, one is on the front of the main beam, while the other is on the back.

All plots to this point have been concerned with the co-polarized component as defined by the azimuth and elevation coordinate system in Figure 5-1. The next five plots are concerned with the cross-polarized component defined in the same coordinate system (Test 2). Beginning with Figure 5-10 the cross-polarized far-field component is plotted over 80 dB of dynamic range and $\pm 30°$ spatial angle with zero dB corresponding to the main beam peak on the previous co-polarized plots. For the E-plane the cross-polarized maximum is approximately 24 dB below the co-polarized beam maximum. From the cross-polarized measurements it is apparent that the maximum value of the two principal lobes is not highly dependent on the reflector surface trueness; however, the null position and depth between the two lobes is very dependent on the surface. This is, of course, a fundamental property of far-field patterns in that maximums are created by in-phase summations and differences by out-of-phase summations, the latter being more sensitive to errors generated within the antenna. Wide angle, low level lobes are shifted in angle and level by mechanical oscillation in the antenna similar to the previous co-polarized measurements.

Figure 5-11 plots the cross-polarized component for the H-plane over the same dynamic range and spatial angles. Comments similar to the E-plane apply with one exception: The peaks of the plot are approximately 8 dB lower.

Figures 5-12 and 5-13 plot the cross-polarized component in the two diagonal planes. In these plots illumination of the two adjacent reflector quadrants creates the lobe occurring at approximately 5°.

Figure 5-14, a contour plot of the principal lobes, provides an overall perspective of the cross-polarized far-field. In this plot the 0-dB level is again referenced to the co-polarized beam peak. The highest level (lightest shading) covers a dynamic range of -20 to -30 dB, which range is sufficient to show the beam peaks (approximately -24 dB).

Test 3 demonstrates beam steering at 7.73-GHz. In this test the feed was laterally displaced 6 beamwidths (see Table 4-1) on the feed positioner by manually placing it in the steered position. The feed is displaced in the H-plane (elevation), shifting the beam negatively in elevation. Only one far-field plot has been selected to demonstrate beam steering. Figure 5-15 plots the far-field using constant level contours similar to the unsteered case in Figure 5-8. A comparison of the two plots (steered and unsteered) shows that the beam steering operation causes very little beam distortion. Over the angles and dynamic range in Figure 5-15 the pattern is essentially unchanged as the beam is steered over 6 beamwidths of scan even at relatively low pattern levels.

In a multiple or interleaved beam application this distortion-free beam steering is especially important, because it implies that cross-talk between beams will be minimal. Another important point with respect to beam steering is that no coma lobes have been generated, an inherent problem with feed displacement in a parabolic reflector.

Figure 5-15 completes the data reported here for the 7.73-GHz measurements, and a number of important points arise regarding antenna performance at this frequency. The plots in Figures 5-2 through 5-15 show that antenna performance is good. While improvements can be made, basic performance of the antenna has been demonstrated at this point.

In the next series of measurements, the frequency was increased to 11.60 GHz, beyond the predicted highest satisfactory operating frequency of 7.73 GHz. This test intends to show the type and magnitude of degradation that occurs as the frequency is increased. The graphical information to follow is organized parallel to the 7.73-GHz tests; however, no plots are given at this point for the cross-polarized component which was measured after the final cord adjustment in Test 26 (see Table 4-1). For this series, the feed horn is of like design (scaled up), so that differences in reflector illumination are minimal.

Like the previous series, the first pattern is far-field, E-plane plot over 80 dB of dynamic range and +30° of spatial angle. In Figure 5-16, this first plot has features similar to the previous test, and it should be compared with Figure 5-4 to see the effects of increased frequency, in this principal plane. At the increased frequency, surface effects are more important, and errors caused by antenna motion are more significant. The increased sensitivity to surface tolerance appears in the slightly higher first few sidelobes, now -18 dB relative to beam peak as compared to a -21 dB for the 7.73-GHz series. The wide angle sidelobe level has increased by a similar amount, because antenna motion translates into a larger phase error in the measurements. From an overall viewpoint, these two observations are the most significant results of the increased operating frequency.

In Figure 5-17 the far-field pattern is plotted for the H-plane, and similar observations are apparent; however, grating lobes must now be considered. Like the first few principal sidelobes, the grating lobes level has increased somewhat. A most important conclusion is that errors appear to scale with frequency without creating new or unexplained lobes.

Figures 5-18 and 5-19 are plots of the two diagonal planes through the far-field beam peak and are included for comparison to the previous tests. In the two diagonal planes the primary sidelobes, grating lobes, and wide angle lobes have increased with frequency without generating other or unexplained lobes: Frequency scaling has created no apparent anomalies.

The contour plot in Figure 5-20 shows that the lobe structure over the main beam and principal sidelobes is similar to the 7.73 GHz, the essential difference being an overall increased level outside the main beam. The 3-D plot in Figure 5-21 supports a similar conclusion. Allowing for frequency scaling, the patterns at 11.60 and 7.73 GHz are essentially the same.

The next series of tests demonstrates antenna performance at a logical low frequency limit, 2.27 GHz. The feed system for this series is a patch subarray rather than a conical horn. Beam steering is achieved by positioning the subarray at points on a 2x4-ft panel having locational points for a total of 11 subarrays. Again, the ultimate application in this case is multiple overlapping beams, individually selectable. These tests used one subarray physically positioned to simulate switched subarrays.

As in previous test results, the graphics begin with the 2-D far-field plotted in the E-plane over an 80-dB dynamic range and over +30° spatial angles. Allowing for the decrease in operating frequency, the most significant changes in the results are attributed to the feed illumination. While the feed structure had no apparent effect near boresight, the edge diffractions and parasitic apertures have a major effect on the lobes near boresight. The illumination of the back aperture causes the asymmetry seen in the far-field envelope of Figure 5-22. The surface errors still dominate the far-field at angles greater than a nominal 5° off boresight although the effects are reduced 10 dB from the 7.73-GHz collection.

In Figure 5-23, there is minimal contribution from the opposite quadrant, since it is an H-plane plot. In Figures 5-24 and 5-25, the diagonal plots have first sidelobes higher than the principal planes. While in the previous tests these lobes were due to surface errors, in this collection they were due to the aperture edge diffractions combined with the effect of the adjacent apertures.

Paralleling the previous tests, Figure 5-26 plots the far-field patterns at 2.27 GHz as constant level contours and Figure 5-27 plots in 3-D. Both are co-polarized field components, and conclusions concerning these plots are similar to the previous tests.

In the cross-polarized far-field data for the 2.27-GHz tests, only one plot has been included. It is the contour plot in Figure 5-28. The levels given in the figure title are referenced to the main beam peak of the co-polarized field component.

The principal purpose of the 4.26-GHz measurements, Tests 12-17, is the demonstration of the antenna's beam steering capabilities. Pattern performance at this frequency closely resembled that of the 2.27-GHz collections. This volume of the report has no pattern data from the 4.26-GHz collections; Volume II covers these collections in detail. The collections did show conclusively that the antenna pattern steered to predicted angles by offsetting the feed from focus. This method of steering for the hoop column antenna over small angles (less than 5°) resulted in no observable coma-lobing.

Before proceeding with the next series of pattern plots, note that all data presented to this point were collected without adjusting the mesh surface. The feeds were, of course, changed and focused for each frequency, but the mesh surface was unchanged from Tests 1 through 18. The surface was mechanically and electrically measured several times during the series of tests to monitor it for trueness; however, no cord adjustments were made. After Test 18, the tensioning cords were adjusted based on information from metric camera measurements. The intent of these adjustments was to refine the surface to its best possible state for this antenna, realizing that it is a developmental model with minimal provision for fine adjustments. Tests 19 through 26 occurred after the surface adjustment, all using the abbreviated scan method to minimize near-field collection time. Since higher frequencies provide the most accurate measure of reflector trueness, 7.73 and 11.60 GHz are the two frequencies selected. In the pattern plots for this series, one contour plot is included for each quadrant at 7.73 GHz beginning with Quadrant 4. At 11.60 GHz one plot is included for the co-polarized component and one for the cross-polarized component. In the plots to follow, contour graphics are used exclusively; one plot for each test has been included. In evaluating the following plots, it should be recalled that surface tolerance is a primary determinant of close-in sidelobes, assuming other factors such as aperture distribution are unchanged.

27

To establish a reference for the far-field patterns after cord adjustment, one data set was recorded at 7.73 GHz for Quadrant 4 using the abbreviated scan method. The contour plots begin with this test (Figure 5-29), because it provides a reference for evaluating the performance gained by the final cord adjustments. Again, this is a reference plot and occurs before the final cord adjustments; others to follow occur after final cord adjustments. Figure 5-29 is similar to the full scan given in Figure 5-8; however, the valid far-field angles for the abbreviated scan must exclude the unscanned parasitic apertures. From the diagnostics it has been shown that all the data on these contour plots are valid, excluding the azimuth and elevation angle positions of (2.5,2.5), (2.5, -2.5) and (0.0,5.0). These positions are dominated by the unscanned apertures.

Comparing Figures 5-29 and 5-30 (before and after final cord adjustment) shows that the first sidelobe level has been reduced, most notably along the minus to plus diagonal. After adjustment, the first sidelobe's peak is essentially at the -20-dB level reduced from the -17-dB level.

The next three contour plots (Fig. 5-31, 5-32, and 5-33) are for Quadrants 2, 3 and 1, respectively. These figures show after-adjustment performance on a quadrant-to-quadrant basis. For each of these plots the feed was positioned for best focus using near-field center lines as a basis for feed location. A comparison of Figures 5-30 through 5-33 shows that there is much similarity; however, Quadrant 1 has higher sidelobe structure than the others.

Figure 5-34 plots the cross-polarized component to demonstrate this performance after final cord adjustment. This plot is for Quadrant 4, and the most significant feature is an improved symmetry between the two principal lobes that characterize the cross-polarized far-field. They are now approximately equal in shape and height, while in earlier plots they were substantially unbalanced.

Test 24 appears in the plan as a reference check in the near-field testing and contains no new information. For this reason no plot appears here for the test.

The final two plots in Figures 5-35 and 5-36 are for the 11.60-GHz frequency, Quadrant 4. As the previous plots, they show performance after the final cord adjustment.

5.3   ANTENNA GAIN/BANDWIDTH

For these two measures of antenna performance it is important to realize that the hoop column antenna in this program has been configured for quad aperture operation. The reflecting surface has been contoured to form four parabolas having four focal points in a single structure. Figure 4-1 graphically illustrates the illuminated quadrant and the mechanism for scanning it. Most of the measurements used one quadrant (Quadrant 4) extensively; however, all were tested to some extent.

In the gain values listed in this section it should also be realized that true antenna gain in dBi is being given, not to be confused with or interpreted as directivity of the various parameters measured in a near-field system. Accurate antenna gain is difficult to measure, primarily because of its inherent sensitivity to impedence match and reflections within the probe circuitry. Because the probe radiation pattern is relatively wide, reflection external to the probe can also produce significant errors. In the measurements that follow, great care has been taken to produce accurate, state-of-the-art results.

Table 5-1 lists antenna gain versus test number for the first 17 tests. The accuracy of the gain measurements throughout the program was consistent with the error analysis in Section 3.2. The values given for gain are peak values in dBi for both the co- and cross-polarized field components. The actual cross-pol peak in Test 2 was determined to be 26.85 dB when polarization was aligned more accurately in Test 23, although Test 2, due to initial alignment, had an apparent cross-pol of 29.75 dBi.

Table 5-2 tabulates the 3-dB beamwidth in the two principal planes for each frequency for the co-polarized field component. The primary error source in beamwidth is the resolution of the far-field data (density of the data points). For this report the error is within +2% of the true value.

Table 5-1   Measured Antenna Gain

Test No.	Freq GHz	Feed Position	Feed Polari- zation	Probe Polari- zation	Illum- ination- Quadrant	Beamscan Beamwidth	Peak Gain, dB
1	7.73	1	Linear	Co-Pol	4	0	50.86
2	7.73	1	Linear	X-Pol	4	0	26.85
3	7.73	11	Linear	Co-Pol	4	6	51.52
4	11.60	1	Linear	Co-Pol	4	0	53.85
							31.00 Cross-pol
5	2.27	1	Linear	Co-Pol	4	0	39.65
6	2.27	1	Linear	X-Pol	4	0	15.43
7	2.27	2	Linear	Co-Pol	2	1	39.35
8	2.225	1	Circular	Co-Pol*	4	0	31.76
9	2.225	1	Circular	X-Pol*	4	0	14.2
10	2.225	8	Circular	Co-Pol*	4	2	32.02
11	2.225	8	Circular	X-Pol	4	2	14.7
12	4.26	1	Linear	Co-Pol	4	0	45.57
13	4.26	8	Linear	Co-Pol	2	2	45.03
14	4.26	11	Linear	Co-Pol	4	6	44.75
15	4.26	1	Linear	Co-Pol	2	0	45.07
16	4.26	2	Linear	Co-Pol	2	1	44.91
17	4.26	3	Linear	Co-Pol	2	-1	44.91

*RHC and LHC response computed from orthogonal linear measurements

Table 5-2   Measured Beamwidth

Test No	Freq, GHz	E-Plane Beamwidth, °	H-Plane Beamwidth, °
1	7.73	0.43	0.50
4	11.6	0.29	0.35
5	2.27	1.55	1.30
8	2.225	1.64	1.38
12	4.26	0.78	0.73

5.4 NEAR-FIELD DIAGNOSTICS

The planar near-field technique is an accurate method for determining
the far-field radiation characteristics of high gain antennas. Perhaps
more importantly, the measurements contain information necessary to
diagnose problems associated with antenna design and fabrication.
Additionally, since the sampled field data may be converted easily to
physical antenna sources, they provide an accurate simulation of physi-
cal changes to an existing antenna. This section describes the decom-
position of the far-field pattern of the NASA Langley Hoop Column
Antenna into the physical mechanisms responsible for its generation.

5.4.1   Near-Field Measurement Plane Projection

Fundamental to the diagnostic techniques described in this section is
the ability to compute the complete electric fields on any plane paral-
lel to the original measurement sample plane projection used for the
results of such a computation. Appendix D describes this computation
method in detail to clarify the mathematical operations used.

Figure 5-37 shows the geometry of the sample plane projection used for
the results of this section. The aperture fields were calculated in
the plane containing the hoop of the antenna assuming that no forward
radiating sources were contained in the volume between the two planes.
Significant direct feed radiation toward the measurement sample plane
could contaminate the computed aperture fields, contributing to error
in their interpretation. There are techniques for reducing this con-
tamination, but because the 7.73-GHz feed horn used on this antenna has
very low back radiation, the error in the computed aperture fields is
insignificant. The need for and usefulness of this field projection
will be explained in the sections that follow.

5.4.2   Reflector Surface Mapping

The electrical phase of the projected sample plane field may be used to
map the mechanical reflector deviation from its ideal surface shape.
It is a well-known fact that a point source of radiation placed at the
focus of a parabolic reflector generates, upon reflection, a planar
wavefront. Any deviation of the reflector surface from a paraboloid
either advances or delays the reflection of the incident ray, degrading
the planarity of the reflected wavefront. This is illustrated by a

30

blister on the surface of the otherwise ideal reflector in Figure
5-37. The electrical phase in the projected sample plane is a good
representation of the surface deformation. However, the divergence of
the rays by the convex blister degrades the electrical phase in the
measurement sample plane.

The contour phase plots of the Hoop Column Antenna in Figures 5-38 and
5-39 show these effects. Figure 5-38 shows the electrical phase at the
measurement sample plane, and Figure 5-39 at the aperture projected
sample plane. While the two plots are similar in the slowly varying
error, the projected phase clearly shows the details of mesh tie points
and pillowing. The more lightly shaded contours represent low regions
in the mesh surface; the dark contours are high regions as viewed from
the front side of the reflector.

Comparison of these two plots shows an important point that could be an
advantage for surface adjustment capability. The electrical phase at
the measurement sample plane is a reasonably good representation of the
slowly varying surface deformation, the primary mechanism generating
the first sidelobes of the far-field of this antenna. If a local por-
tion of the surface of the reflector were adjusted while monitoring the
electrical phase over that region, (i.e., positioning the probe to that
point in the near-field array and reading the network analyzer) the
slowly varying deformation could be quickly and accurately removed.
This process is analogous to real-time minimization of the first side-
lobe in the far-field of the antenna, an easy and effective solution to
a classical antenna problem.

The phase contour of Figure 5-39 can be converted, if desired, to
dimensional reflector deviation with an application of the geometry
illustrated in Figure 5-40. This drawing is an expanded view of the
blister shown on the reflector in Figure 5-37. A deviation d from the
ideal reflector surface will cause a path length difference of approxi-
mately 2d in the two paths illustrated, inducing a phase change in the
sample plane of approximately 720 d/L degrees, where L is the free
space wavelength of the RF frequency of operation. The dimensional
deviation of the surface can be calculated as

$$d = PL/720$$

where   d = deviation of reflector surface in inches from ideal
             paraboloid normal to surface;
         p = deviation of phase in sample plane in degrees;
         L = free space wavelength in inches of RF of operation.

The ability to map the surface deviation from RF measurements may have
a significant influence on the future manufacture of large space-
deployable mesh antennas, namely, extension of the technique to map the
surface of antennas already deployed in space.

5.4.3 Aperture Decomposition

The hoop column antenna measured at the Denver Aerospace Near-Field
Laboratory has the unique characteristic of employing four separate
offset reflectors in a single section of circular mesh. Each offset
reflector has its vertex located approximately 20 inches from the mast

31

center with an aperture shaped as a 90° pie section as shown in Figure 5-41. Each aperture is illuminated with a separate feed with a fundamentally circular pattern. The geometrical mismatch between the aperture shape and feed illumination pattern generates unintentional illumination of the adjacent and opposite apertures (hereafter referred to as "parasitic apertures") in addition to the intentionally illuminated (or primary) aperture. This section separates the far-field pattern contribution of the parasitic apertures from that of the primary aperture.

Figure 5-42 shows an amplitude contour plot of the projected aperture fields of the antenna at 7.73 GHz with only the primary aperture's feed horn radiating. Note the resemblance to the physical mesh geometry shown in Figure 5-41, particularly the mesh scalloping at the outer edges, the absence of mesh at the center, and some trace effects from the hoop itself. This plot shows that the illumination of the reflector from the feed extends beyond the boundaries of the primary quadrant, generating the far-field pattern shown in the contour plot of Figure 5-43. This far-field pattern can be represented as the superposition of the far-field patterns of two apertures, the first being the primary aperture, and the second the combination of the three parasitic apertures. The far-field contribution of the primary quadrant alone may be computed by setting all aperture fields outside the primary quadrant's boundaries to zero as shown in Figure 5-44, then computing the far-field pattern of the result, shown in Figure 5-45. Likewise, the contribution of the parasitic quadrant alone, Figure 5-46, can be computed as shown in Figure 5-47. It can be seen that the combination of each parasitic quadrant with the primary quadrant's feed produces a parasitic "main beam," defocused and steered at angles constant with respect to the primary quadrant's main beam. It is also clear that reduction of these parasitic beams with this reflector design may only be accomplished through reduction of illumination of the parasitic apertures.

5.4.4 Far-Field Measurements at Extremely Low Levels (Scattering from the Hoop Support Cords).

The hoop column antenna derives its mechanical rigidity in part from hoop control cords tensioned between the hoop and points above and below the mesh on the column. This design inherently requires radial cords in the aperture of the antenna. The antenna measured at the near-field facility uses quartz cords to minimize the effect on the far-field pattern, and this material works so well that the cords are almost transparent. The effect on the far-field pattern can, however, be measured.

Figure 5-48 shows a contour plot of the co-polarized far-field pattern of the antenna operated at 11.6 GHz. Only one range is plotted, everything above -65 dB, relative to the main beam maximum. This level highlights the effect of the cords in the aperture above the apparent pattern noise floor. The antenna in this case was oriented as shown in Figure 5-41, with horizontal polarization as viewed by the reader. Maximum currents will be induced on the cords aligned with the incident polarization, horizontal, or azimuth direction. The effect of a horizontal cord is therefore a vertical line in the far-field contour plot. This is the predominant effect of the cords in the pattern shown

32

in Figure 5-48. The actual cords are at right angles to their respectively generated lines, and their effect falls off rapidly as the cord's alignment with the incident polarization decreases.

Figure 5-49 shows the cross-polarized far-field pattern of the same antenna and frequency, producing a striking result. This contour plots fields above -75 dB relative to the main beam maximum, producing greater cord effect highlighting due to a lower noise floor than that experienced in the co-polarized pattern. In contrast to the plot of the co-polarized pattern, the 45° lines are more prevalent. The explanation for this phenomenon is a little more involved. A vertical cord, illuminated with horizontal polarization, generates almost no currents and therefore no far-field pattern effect. A horizontal cord, illumination with horizontal polarization, has a large horizontally polarized (co-polarized) far-field pattern effect, but almost none on the vertically polarized (cross-polarized) far-field pattern. However, a 45° cord is excited by that component of the incident horizontal polarization, which upon reradiation has a significant vertically polarized far-field pattern effect, shown in the plot of Figure 5-49 to be greater than either a horizontal or vertical cord.

The quartz hoop-control cords in the aperture of this antenna represents a significant measurement challenge in the far-field, appearing at the -60 to -75 dB level relative to the main beam maximum. The scattering level was established by observing successive level slices in the contour plots until the cord scattering patterns appeared, then all points above that level were plotted in Figures 5-48 and 5-49. The near-field measurement method provides the only known way to definitively measure their effect. They are shown to dominate the far-field beyond 10° from boresight in both the co- and cross-polarized patterns. At these levels, they represent no significant degradation of the pattern impacting any system for which the antenna might be used.

5.5 ERROR ANALYSIS

Having presented the measured patterns, the error analysis introduced in Section 3.2 can now be related to specific test results. In Figures 5-50 through 5-53, far-field patterns for the 15-Meter Hoop Column Antenna are superimposed on error curves for the near-field facility. As recalled in Section 3.2 there are two dominant error sources in the measurements; isotropic scattering from the facility ceiling and z-position (out-of-plane) probe errors.

Beginning with 7.73 GHz, the H-plane far-field pattern is superimposed on the peak error envelopes for the two error sources. Comparing far-field pattern to error envelope level shows that errors in the first few sidelobes are dominated by z-probe position, while wide angle errors are dominated by ceiling reflections. Similar conclusions apply to other frequencies; however, the level of reflection error increases with respect to the peak of the far-field pattern at the lower frequencies. As described in Section 3.2, the level of reflection error is at a constant -15 dBi, relative to the isotropic level of the antenna. Since, at lower frequencies, the gain of the antenna decreases, the isotropic level and hence the reflection error level increase with respect to main beam maximum.

33

In the error curves in Figure 5-50 thru 5-53, it should be noted that they establish a lower limit on the far-field dynamic range. System errors are below the antenna patterns except at wide angles at the lower frequencies.
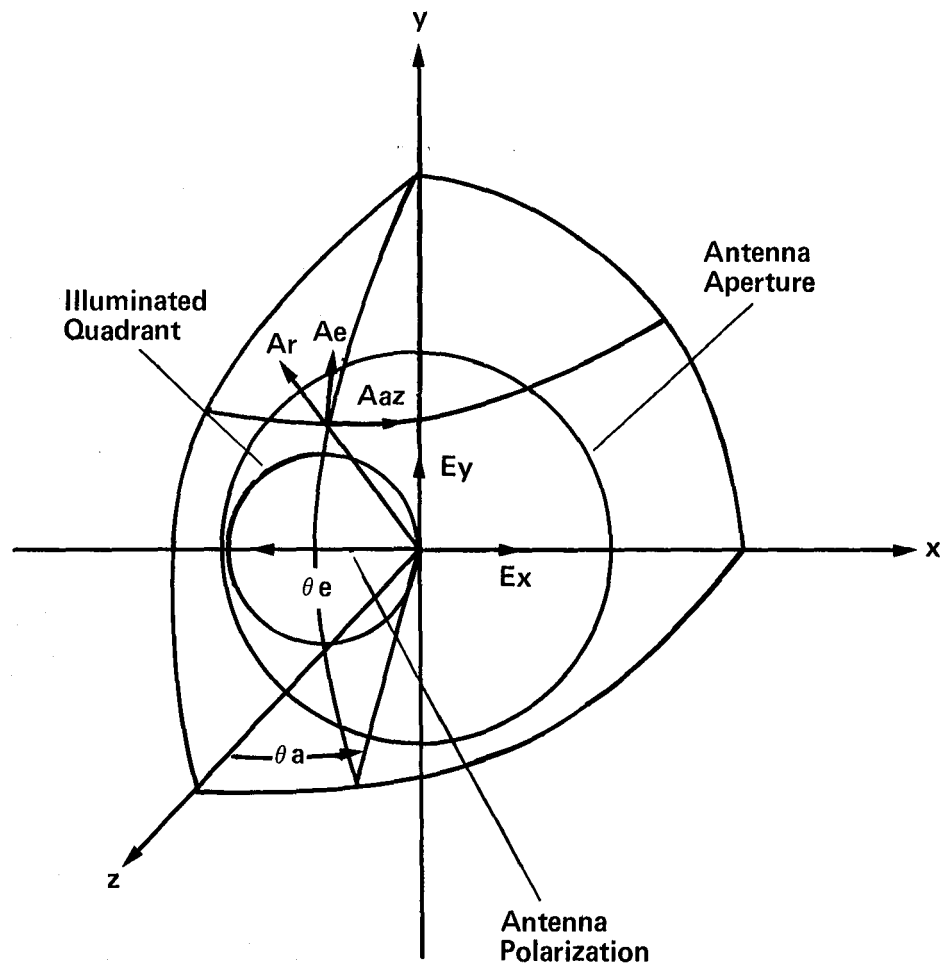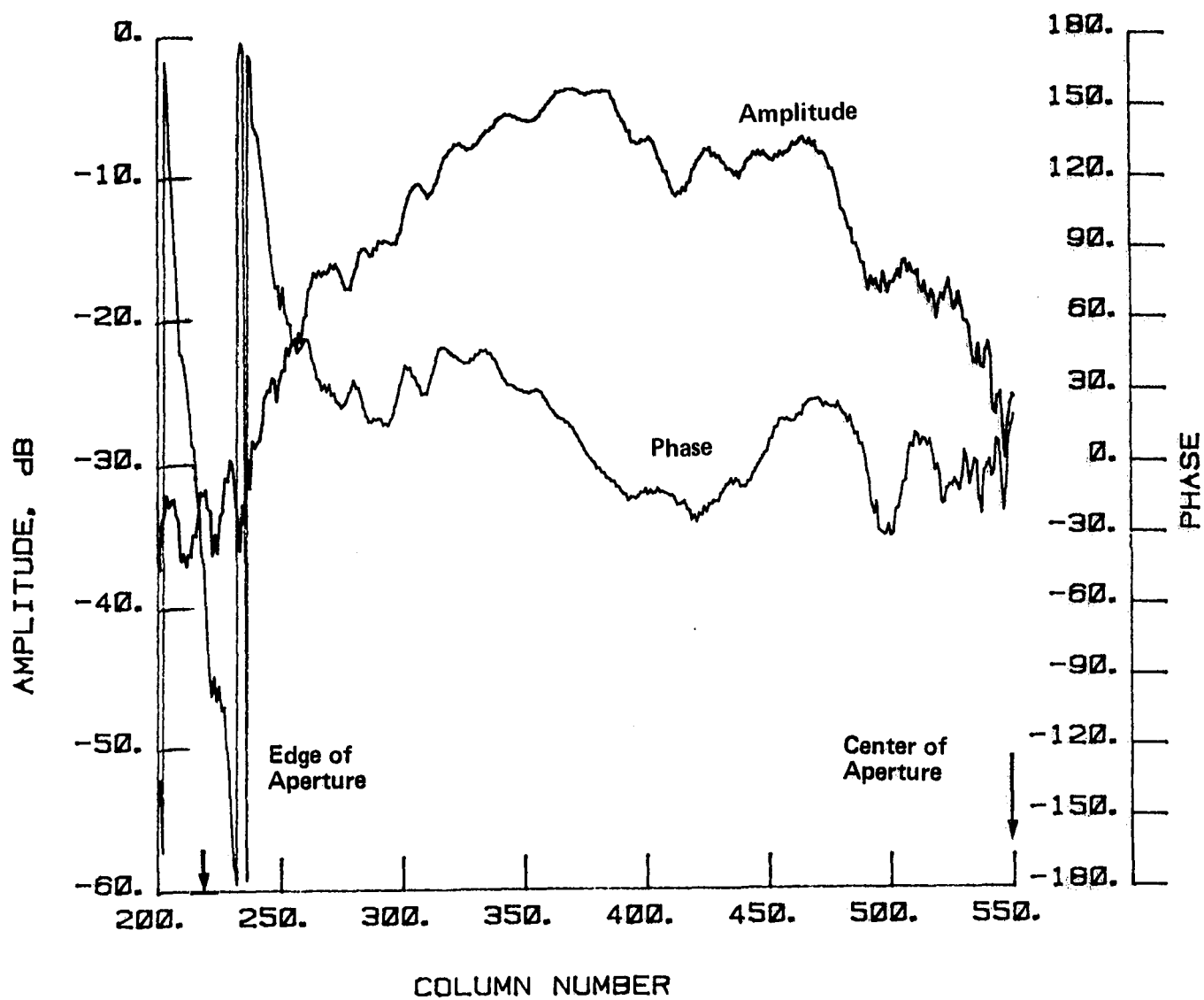
Figure 5-1 Far-Field Coordinate System

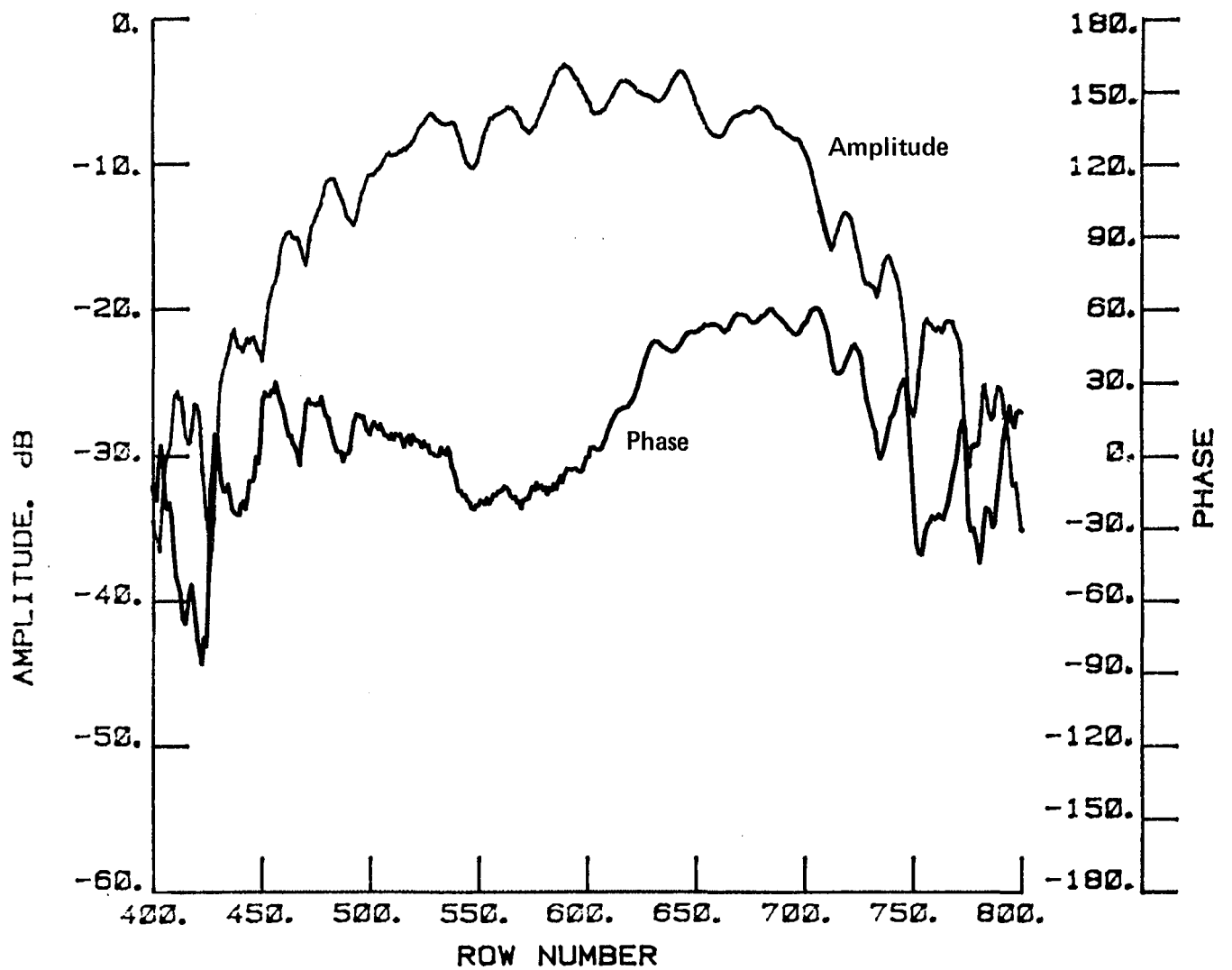*Figure 5-2 Near-Field Pattern, 7.73 GHz, Co-Pol, E-Plane, Test 1*

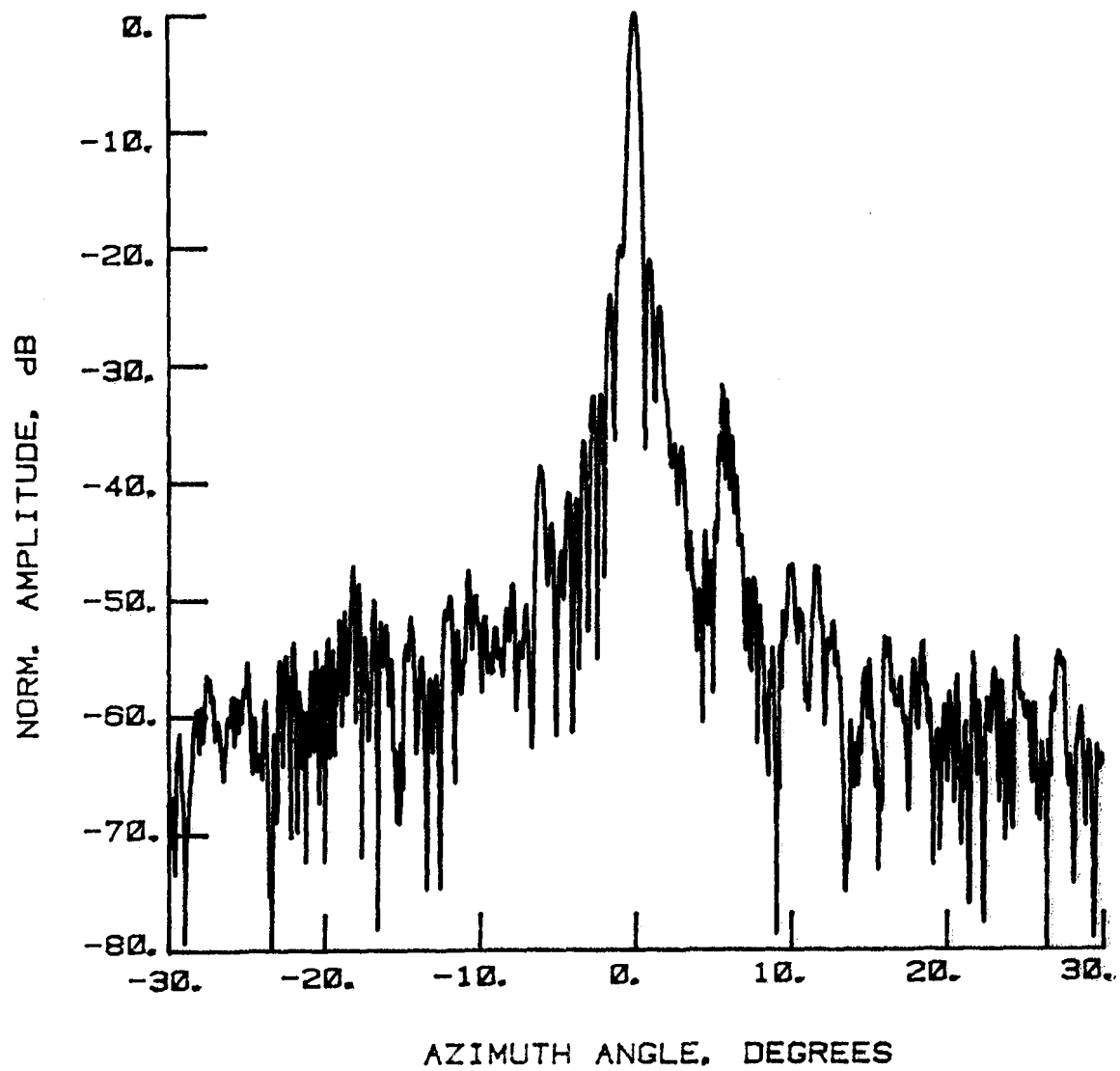*Figure 5-3 Near-Field Pattern, 7.73 GHz, Co-Pol, H-Plane, Test 1*

Figure 5-4 Far-Field Pattern 7.73 GHz, E-Plane, Co-Pol, Test 1, ±30° Scale
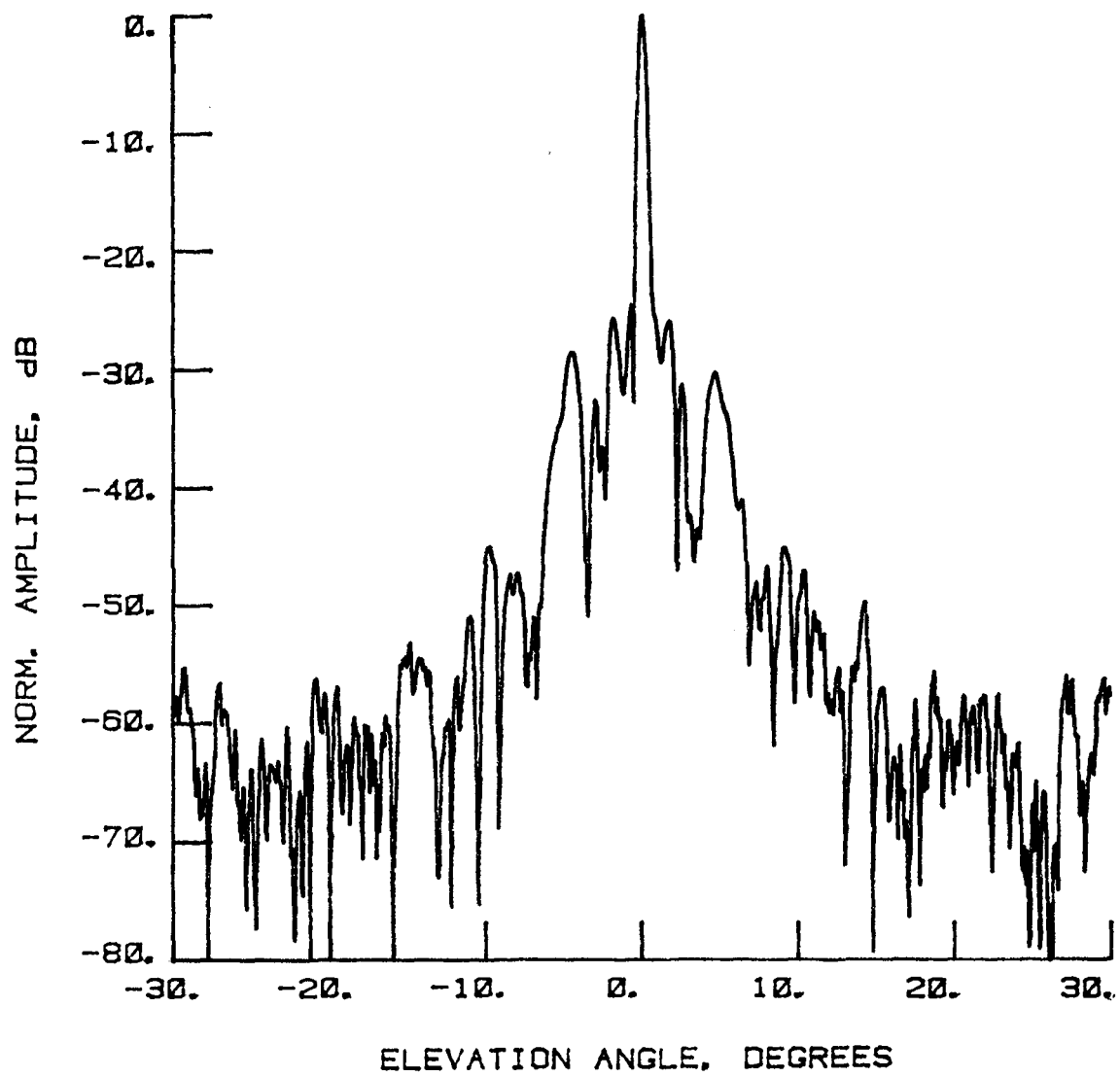
Figure 5-5 Far-Field Pattern, 7.73 GHz, H-Plane, Co-Pol, Test 1, ±30° Scale

39
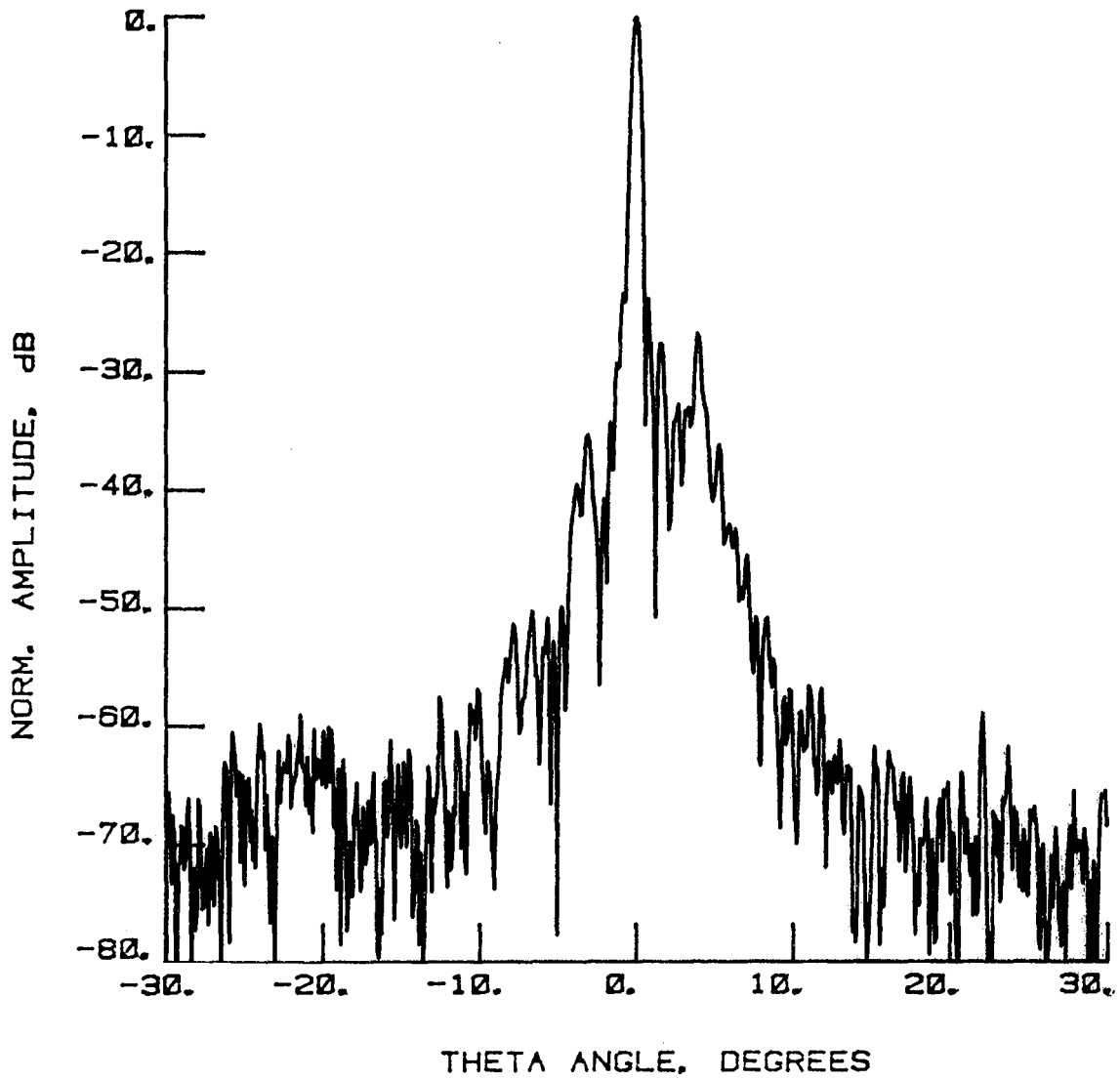
Figure 5-6 Far-Field Pattern, 7.73 GHz, -45° Diagonal, Co-Pol, Test 1, ±30° Scale

40
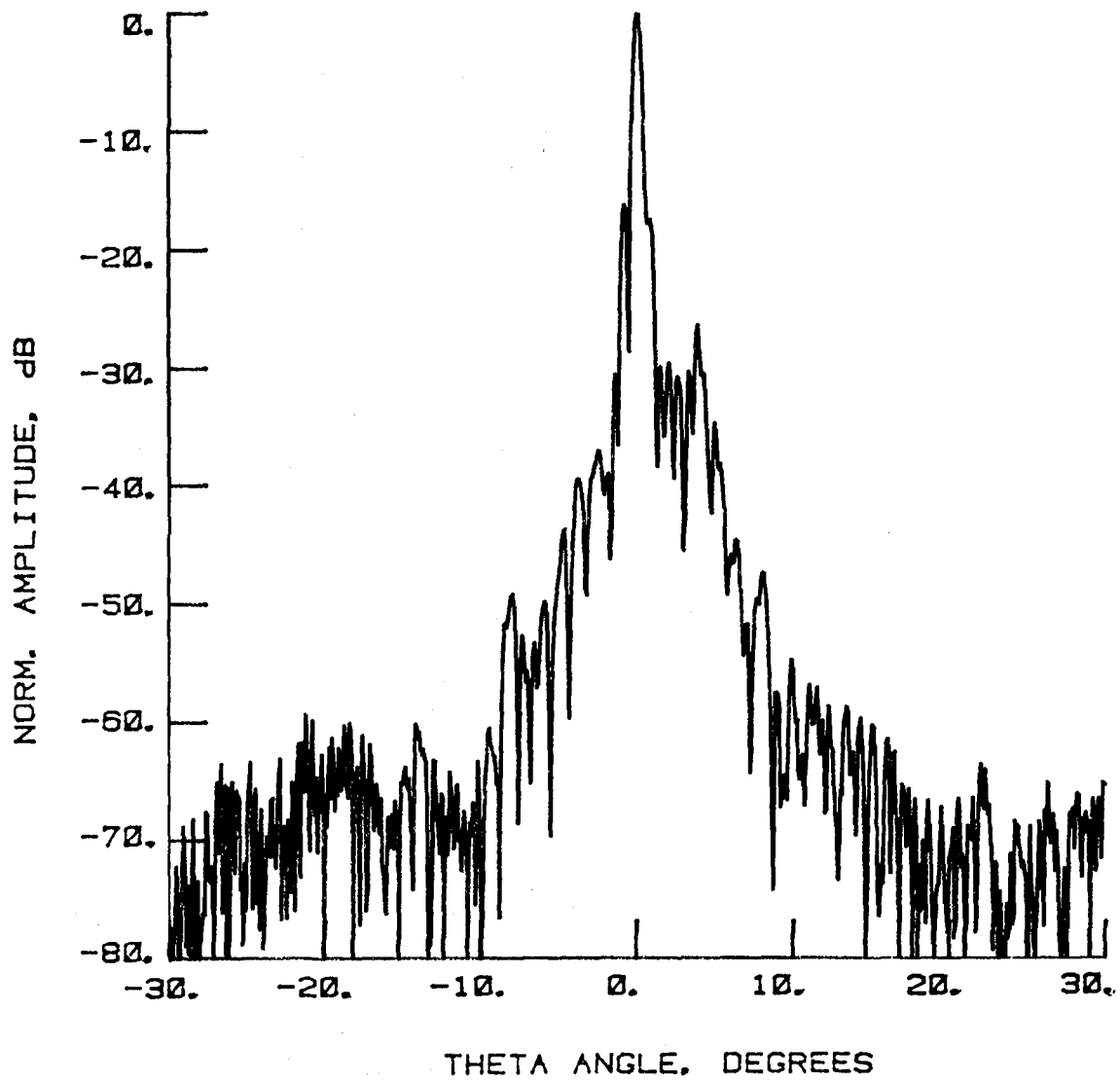
Figure 5-7 Far-Field Pattern, 7.73 GHz, 45° Diagonal, Co-Pol, Test 1, ±30° Scale

41
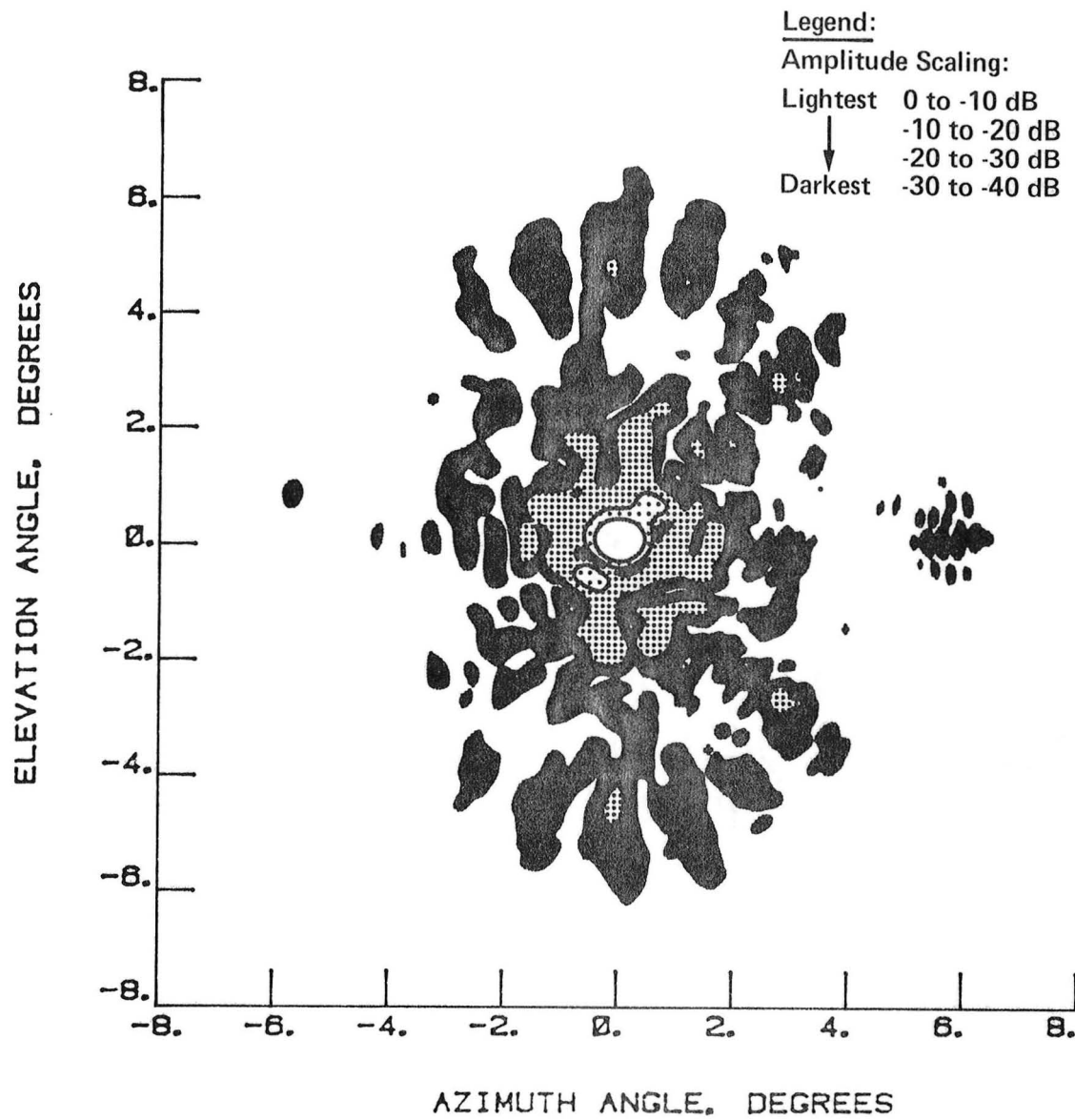
Figure 5-8 Far-Field Contour, 7.73 GHz, Co-Pol, Test 1, ±6° Scale
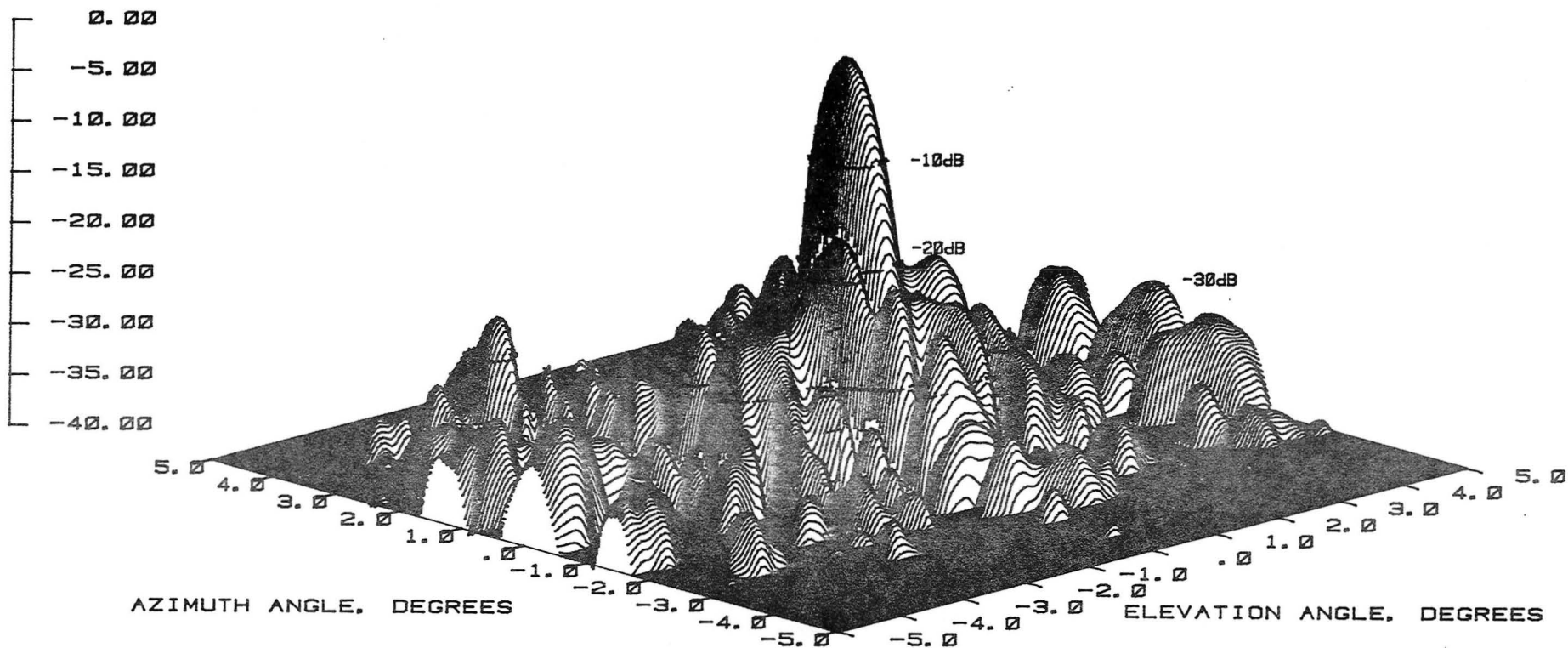
Figure 5-9 Far-Field Pattern, 7.73 GHz, 3-D Plot, Co-Pol, Test 1, ±5° Scale

43 and 44
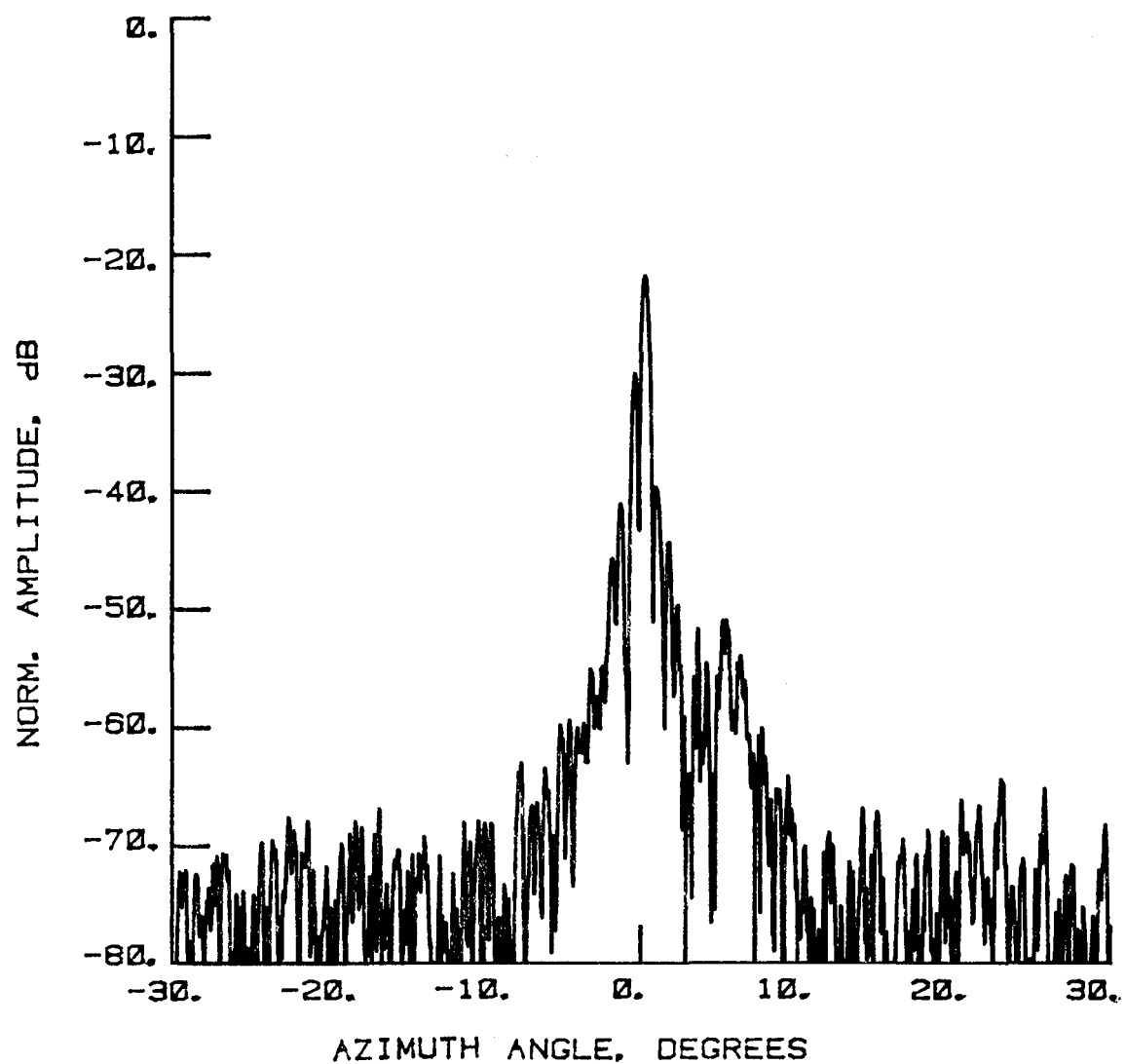
Figure 5-10 Far-Field Pattern, 7.73 GHz, E-Plane, Cross-Pol, Test 2, ±30° Scale
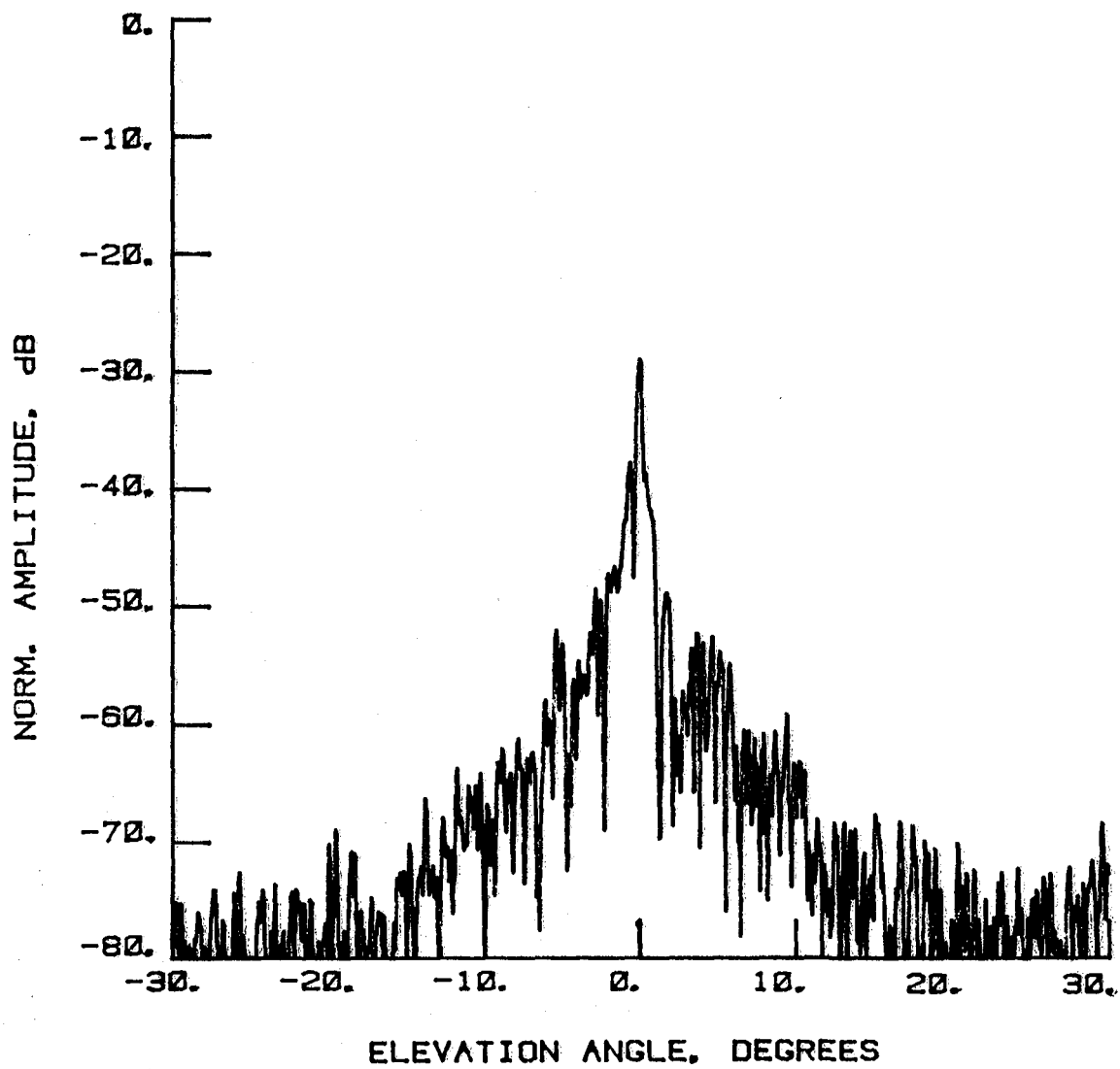
Figure 5-11 Far-Field Pattern, 7.73 GHz, H-Plane, Cross-Pol, Test 2, ±30° Scale
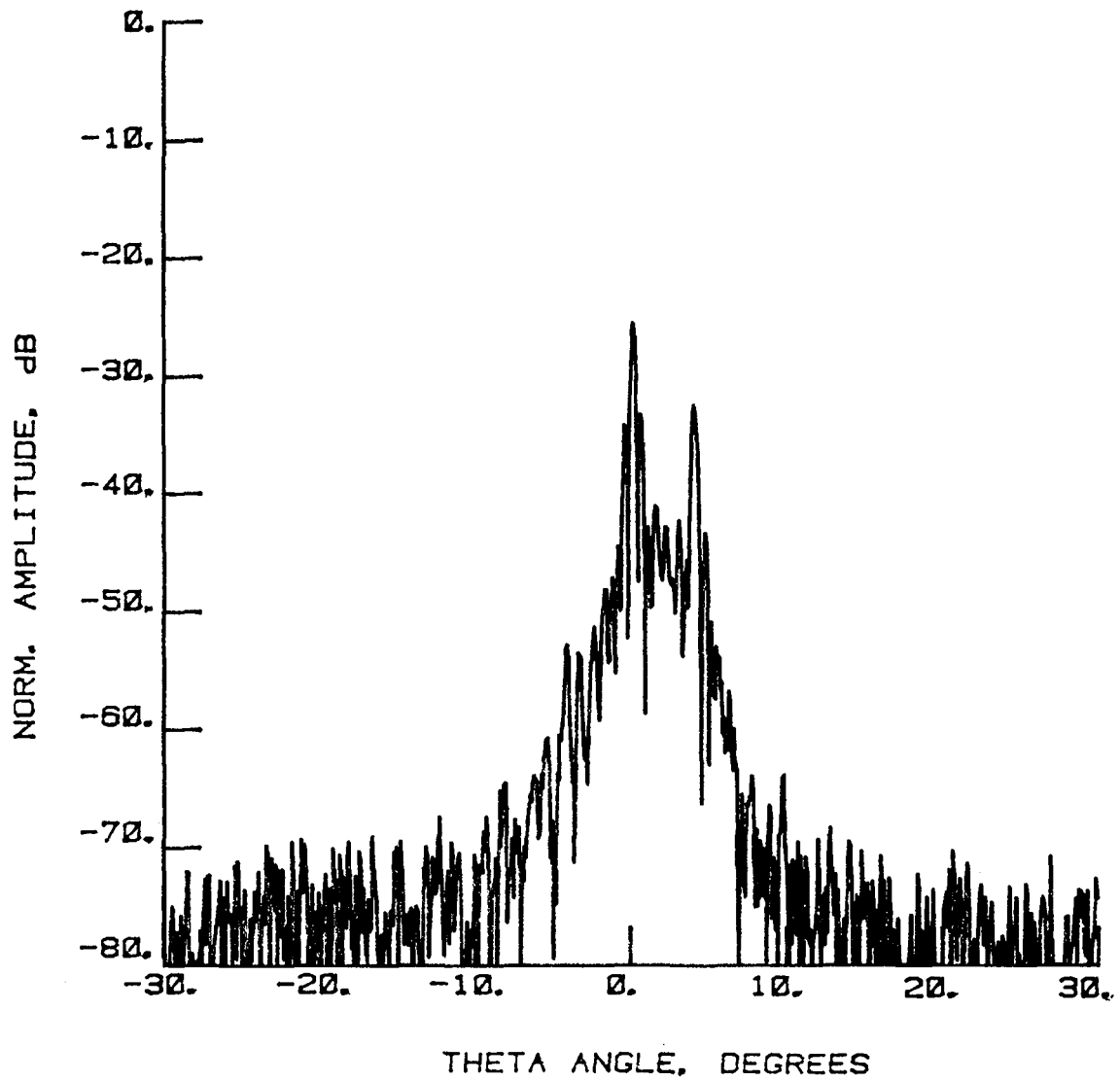
Figure 5-12 Far-Field Pattern, 7.73 GHz, 45° Diagonal, Cross-Pol, Test 2, ±30° Scale
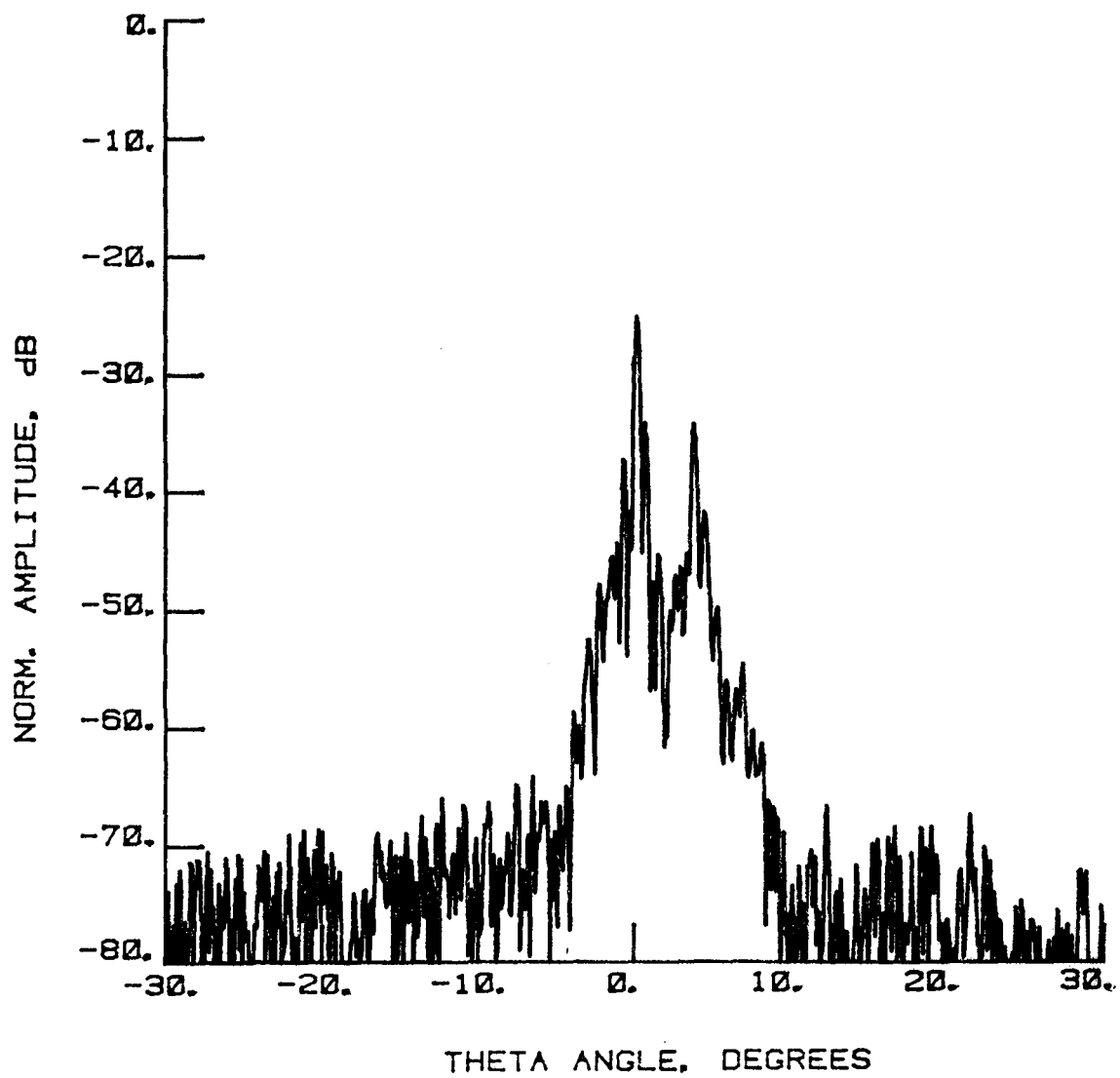
Figure 5-13 Far-Field Pattern, 7.73 GHz, -45° Diagonal, Cross-Pol, Test 2, ±30° Scale
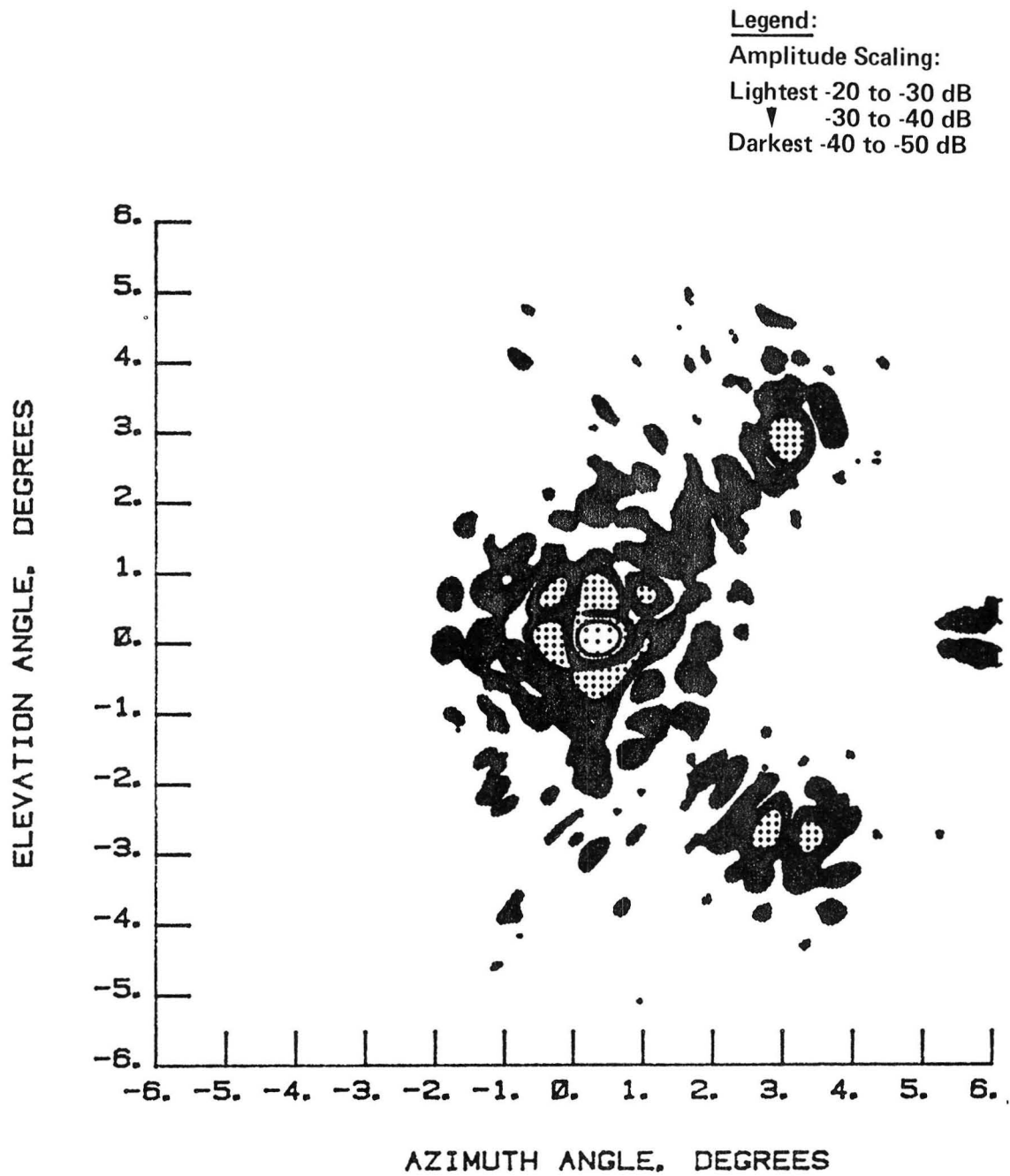
Figure 5-14 Far-Field Contour Plot, 7.73 GHz, Cross-Pol, Test 2, ±6° Scale

49

Legend:
Amplitude Scaling:
Lightest   0 to -10 dB
            -10 to -20 dB
            -20 to -30 dB
Darkest   -30 to -40 dB

ELEVATION ANGLE, DEGREES

AZIMUTH ANGLE, DEGREES
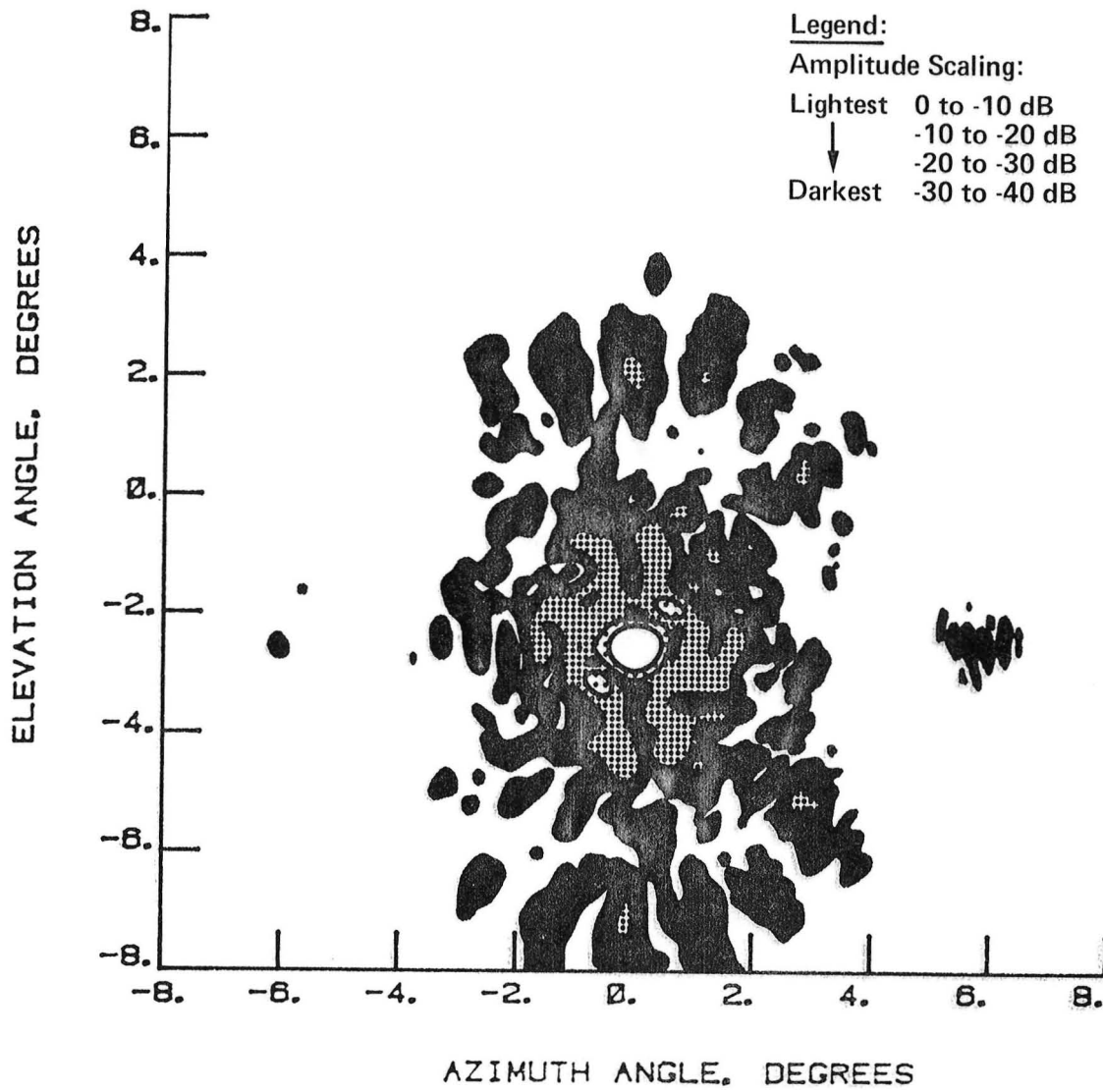
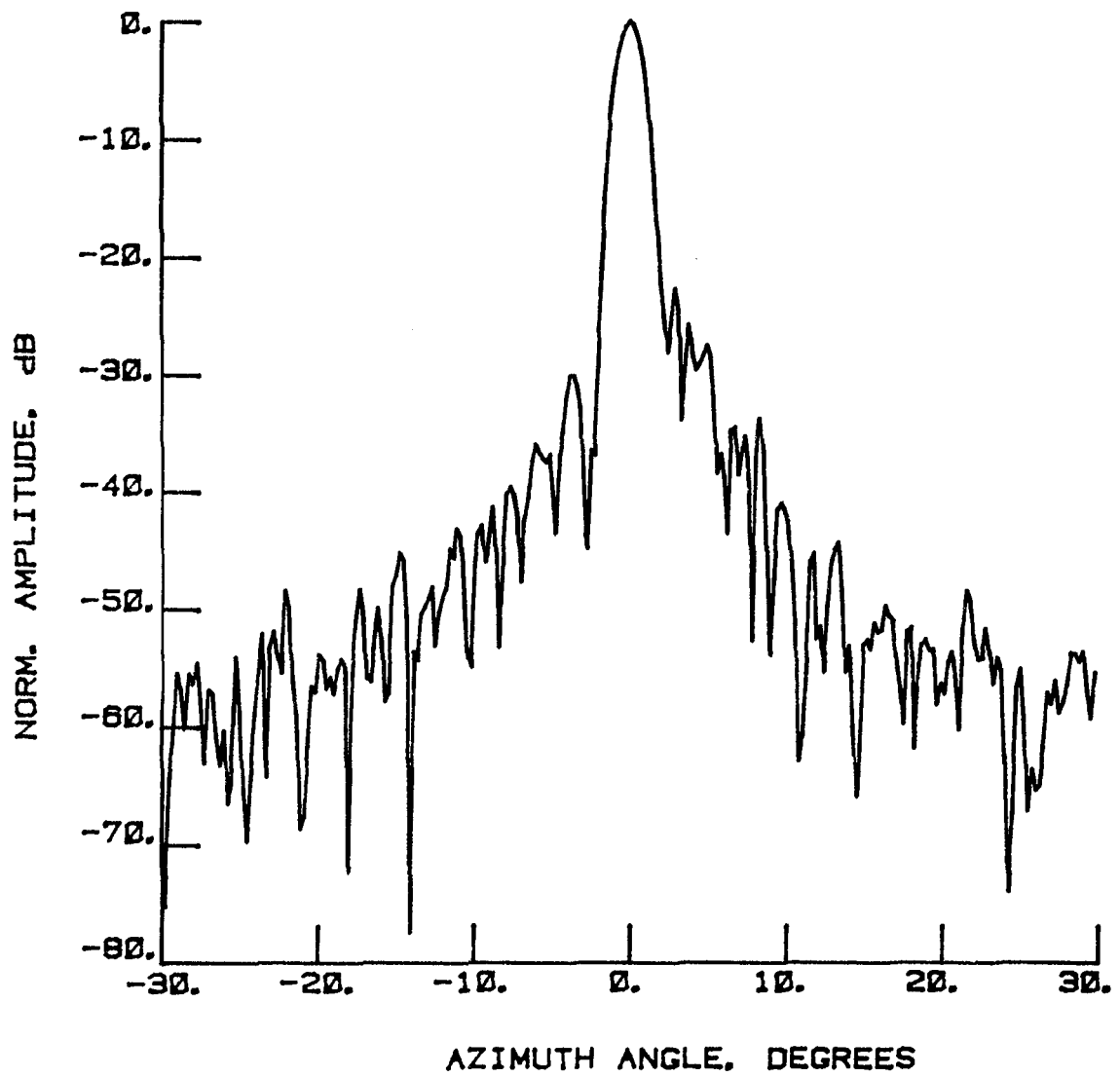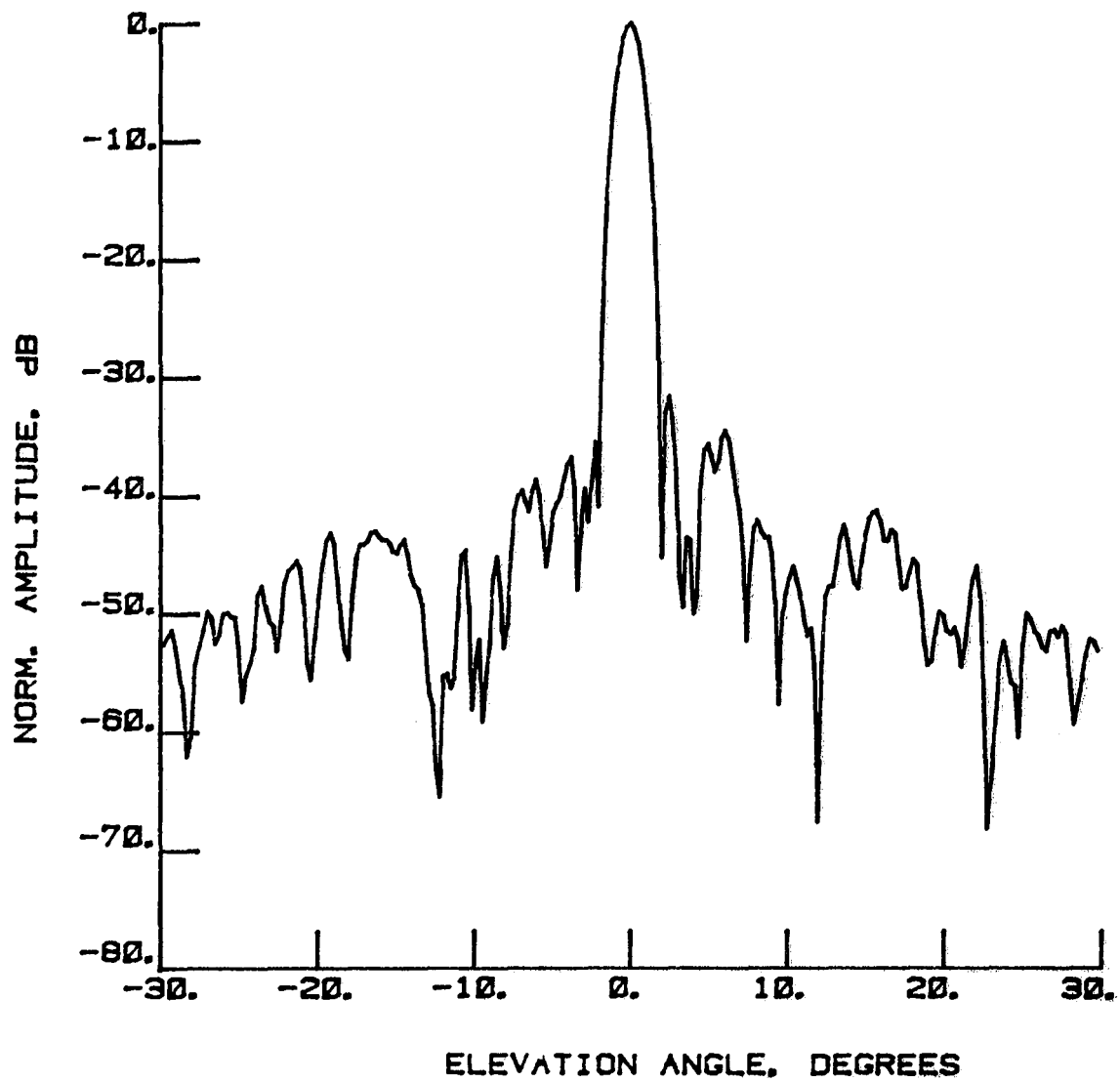*Figure 5-15   Far-Field Contour Plot, 7.73 GHz, Co-Pol, Test 3, ±8° Scale*
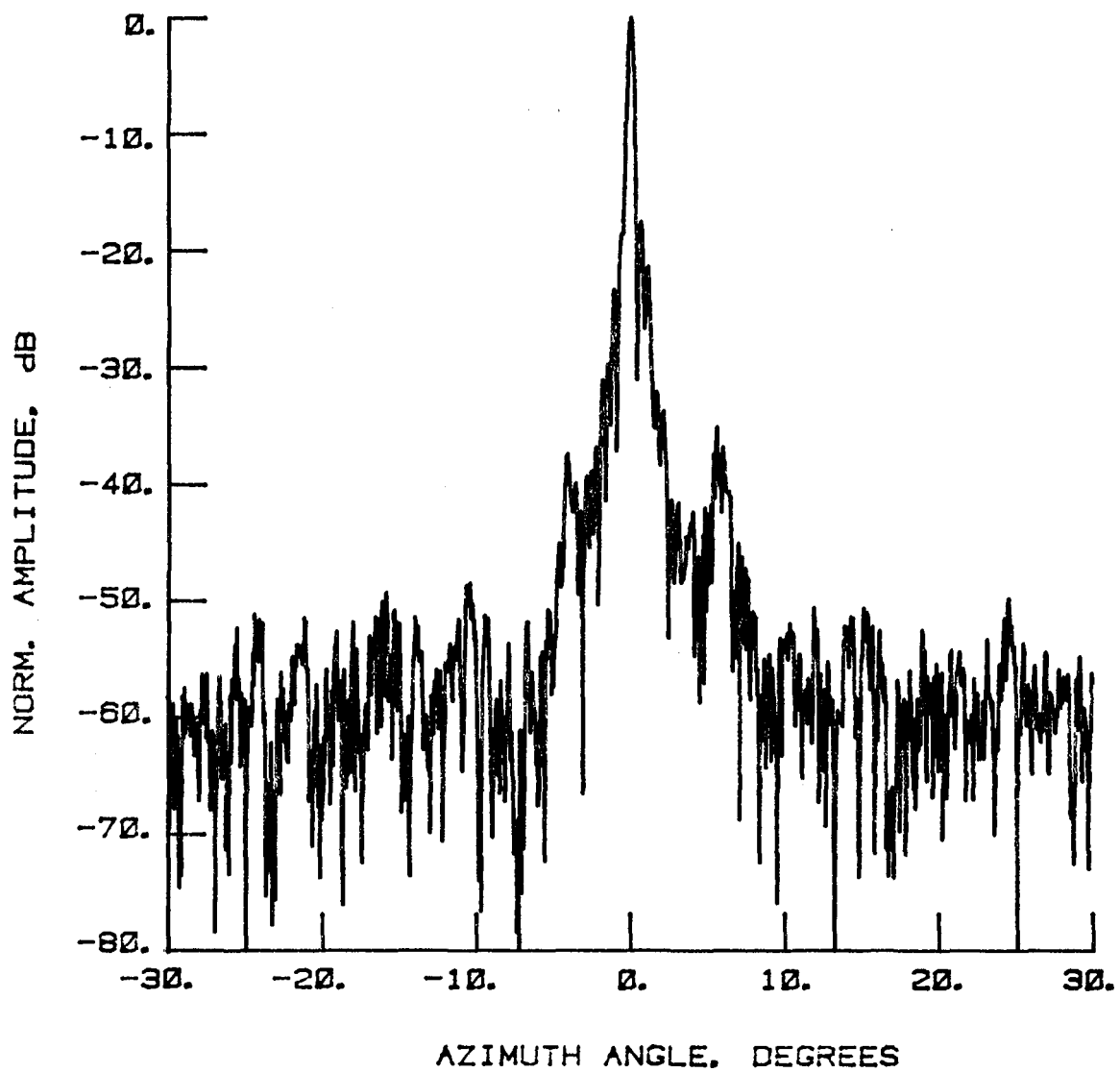
Figure 5-16 Far-Field Pattern, 11.6 GHz, E-Plane, Co-Pol, Test 4, ±30° Scale

51
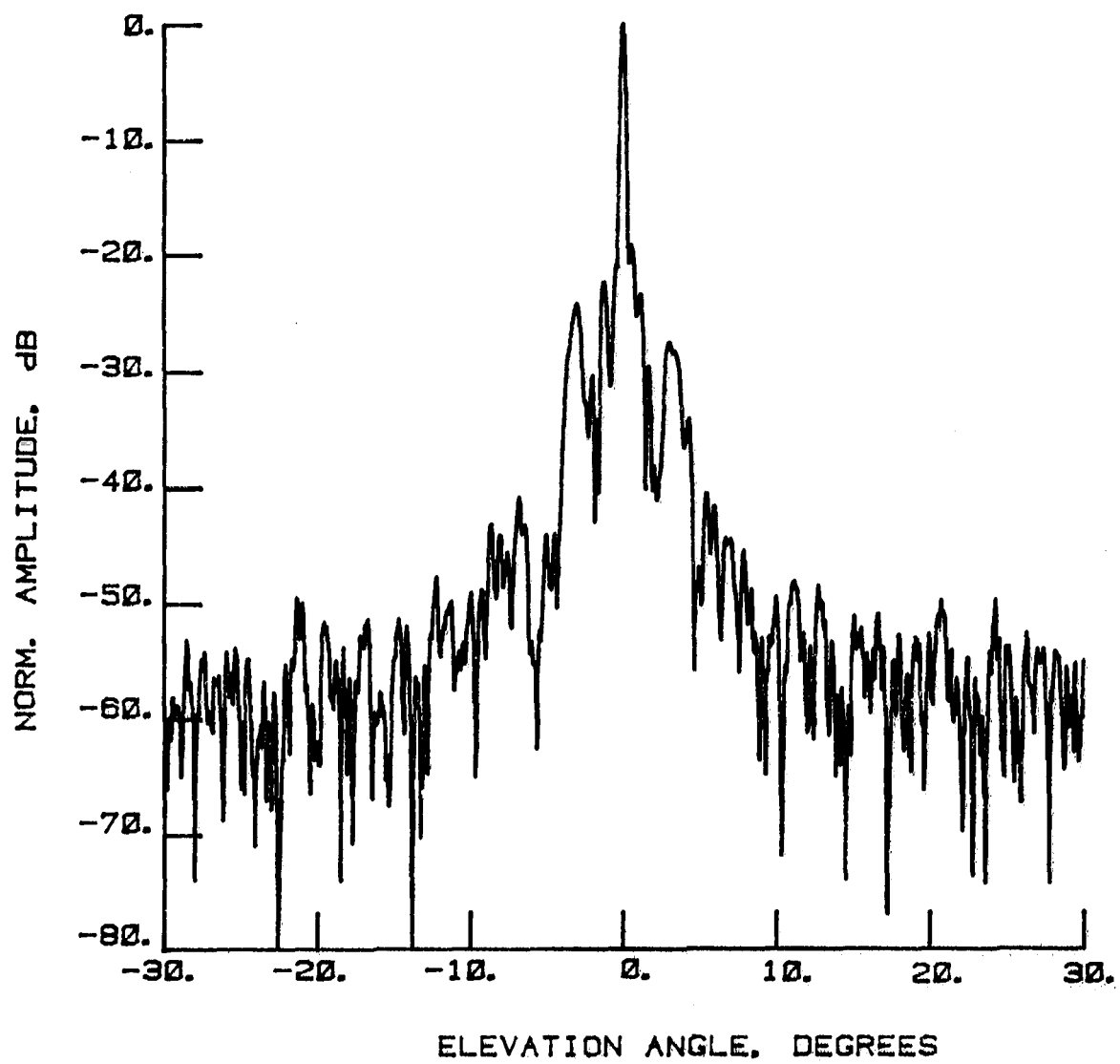
Figure 5-17 Far-Field Pattern, 11.6 GHz, H-Plane, Co-Pol, Test 4, ±30° Scale
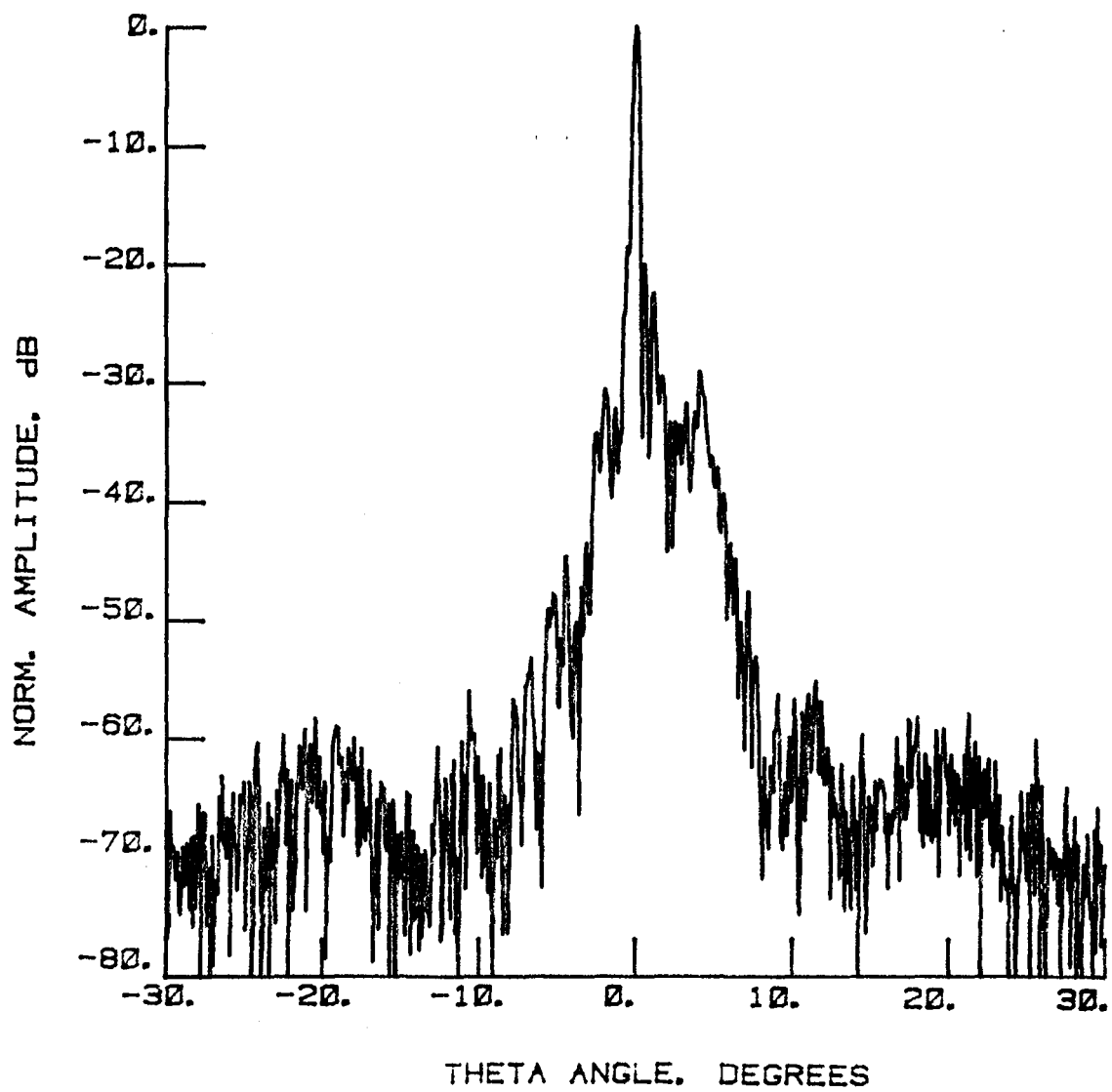
Figure 5-18 Far-Field Pattern, 11.6 GHz, 45° Diagonal, Test 4, ±30° Scale
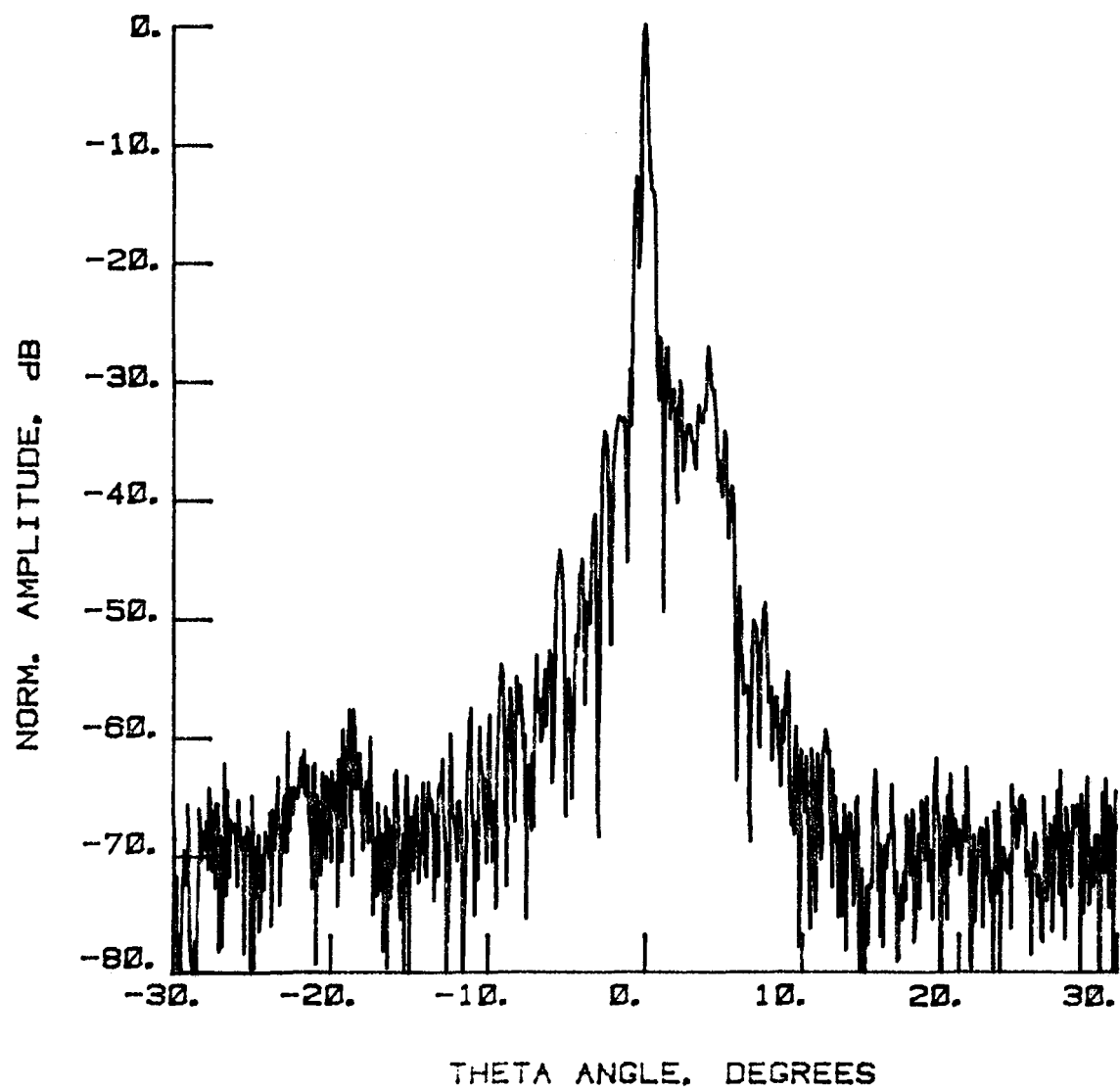
Figure 5-19 Far-Field Pattern, 11.6 GHz, -45° Diagonal, Test 4, ±30° Scale

54
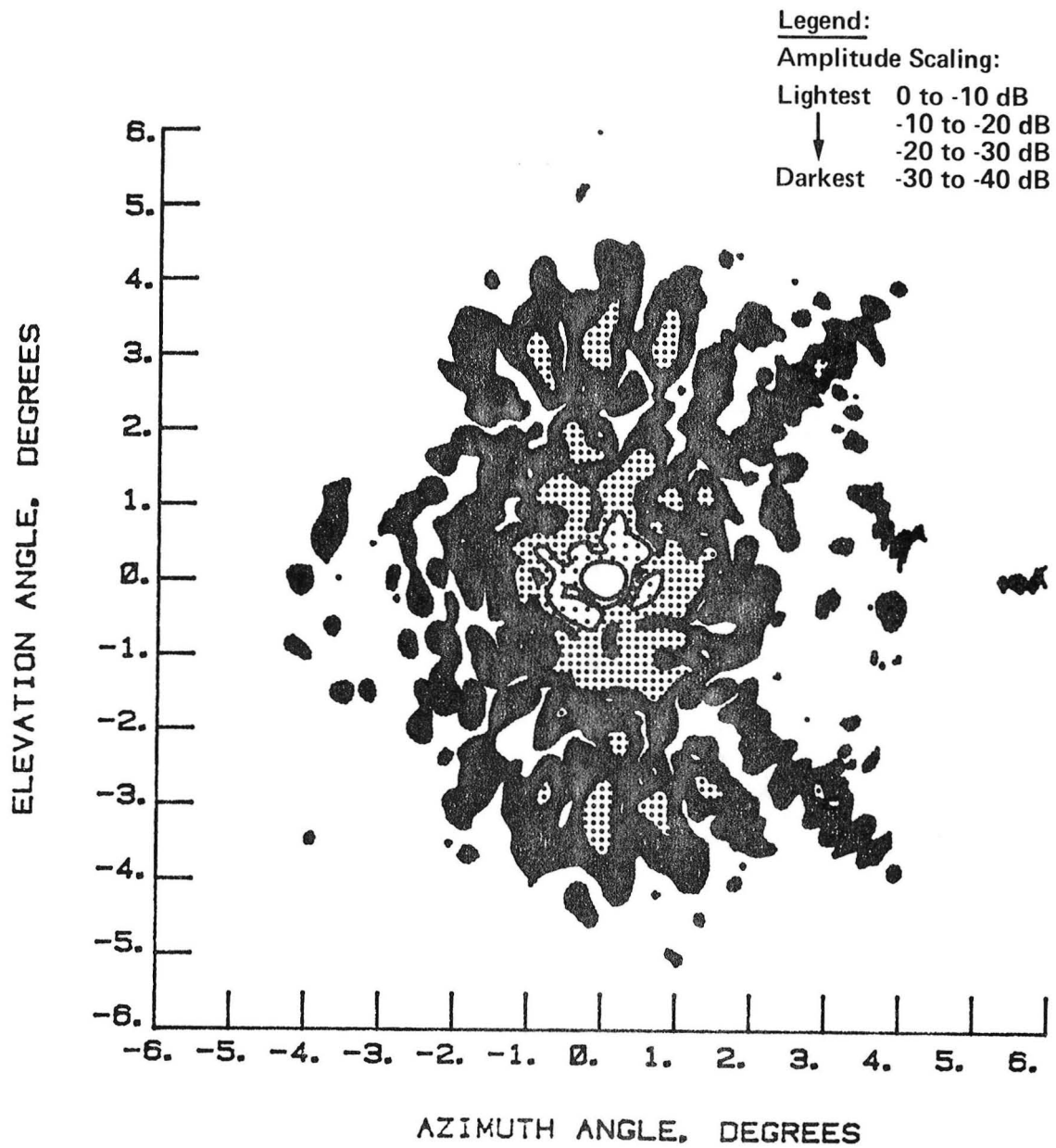
Figure 5-20 Far-Field Contour, 11.6 GHz, Co-Pol, Test 4, ±6° Scale

This Page Intentionally Left Blank

NORMALIZED LOG
AMPLITUDE. dB

Ø. ØØ

−5. ØØ

−1Ø. ØØ

−15. ØØ

−2Ø. ØØ

−25. ØØ

−3Ø. ØØ

−35. ØØ

−4Ø. ØØ

-10dB

-20dB

-30dB

AZIMUTH ANGLE. DEGREES

ELEVATION ANGLE. DEGREES
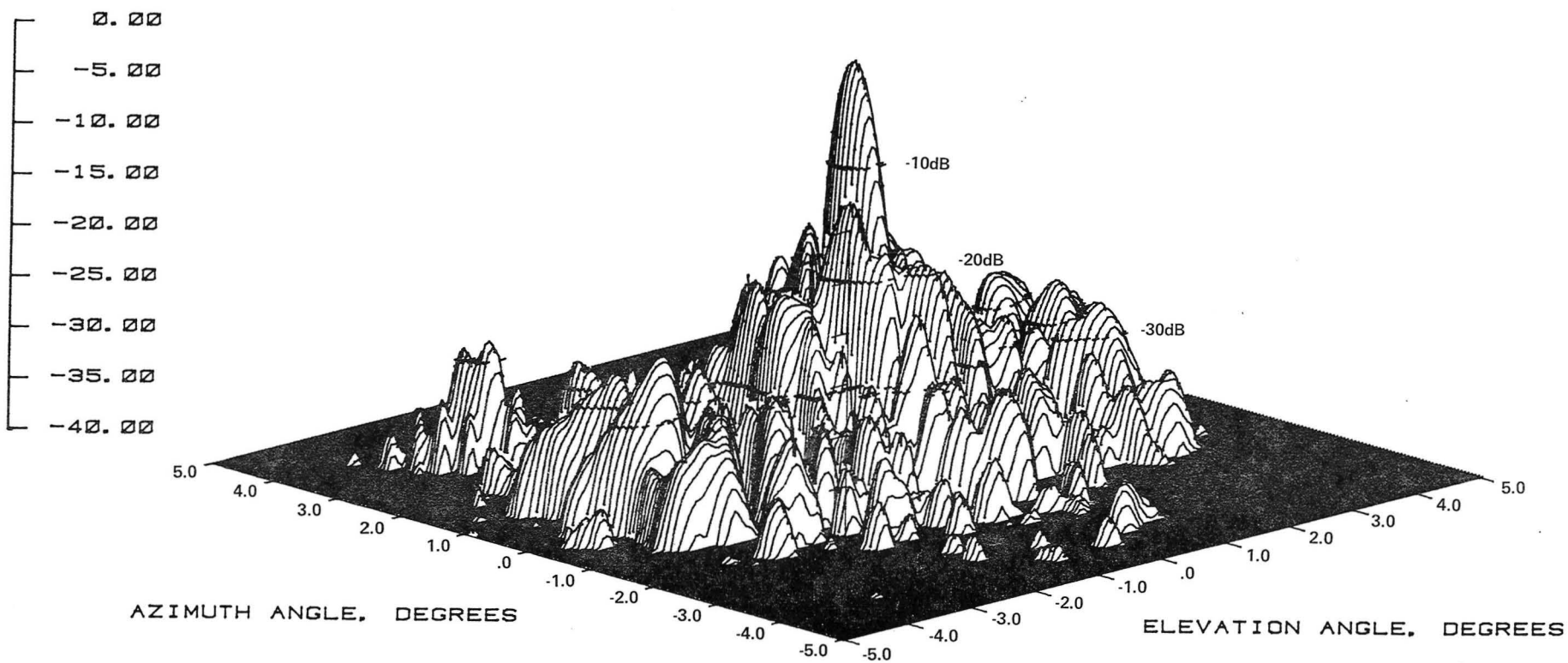
Figure 5-21 Far-Field Pattern, 11.6 GHz, 3-D Plot, Co-Pol, Test 4, ±5° Scale

57 and 58

Figure 5-22 Far-Field Pattern, 2.27 GHz, E-Plane, Co-Pol, Test 5, ±30° Scale

59

Figure 5-23   Far-Field Pattern, 2.27 GHz, H-Plane, Co-Pol, Test 5, ±30° Scale
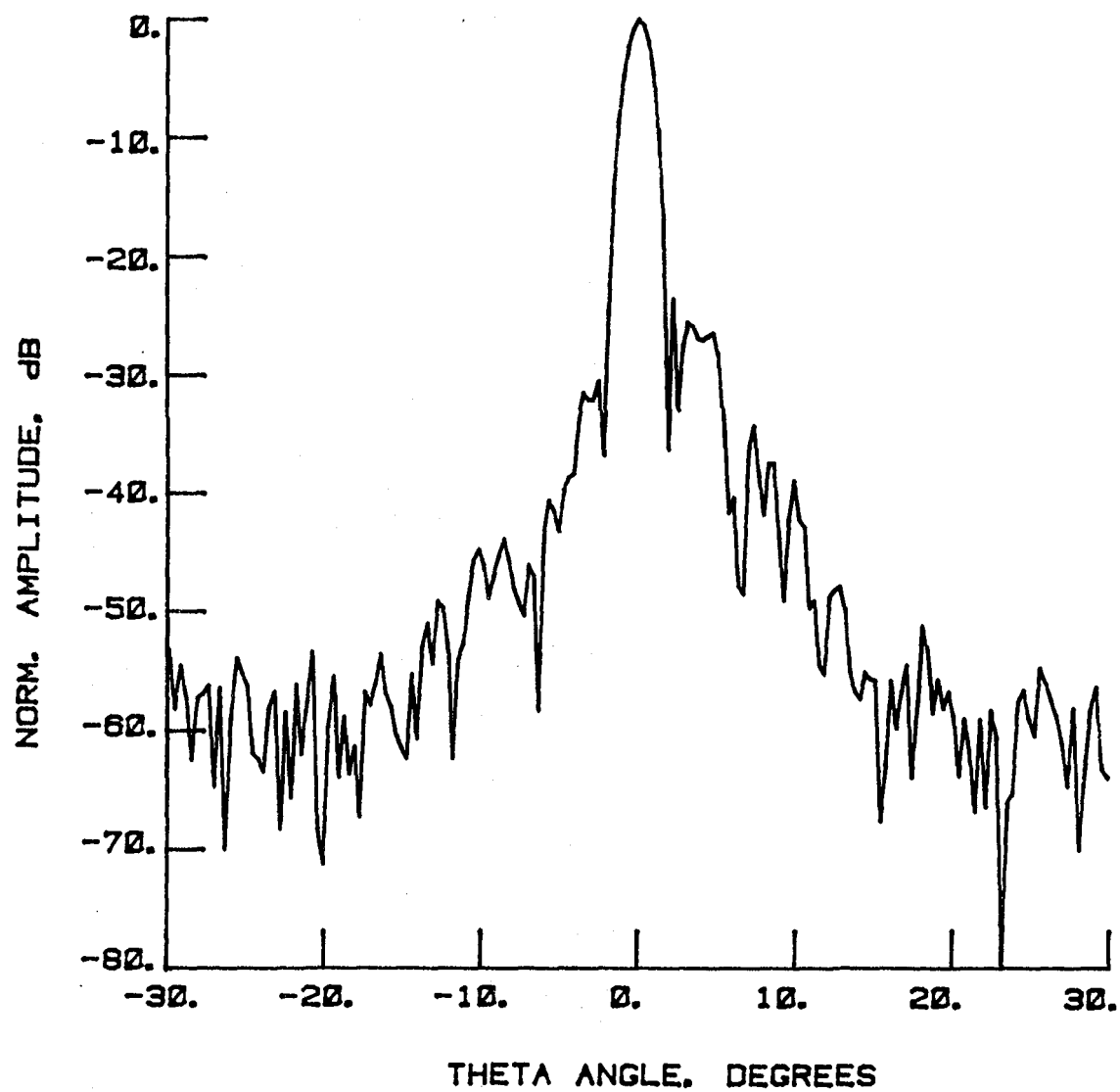
Figure 5-24 Far-Field Pattern, 2.27 GHz, -45° Diagonal, Co-Pol, Test 5, ±30° Scale

61
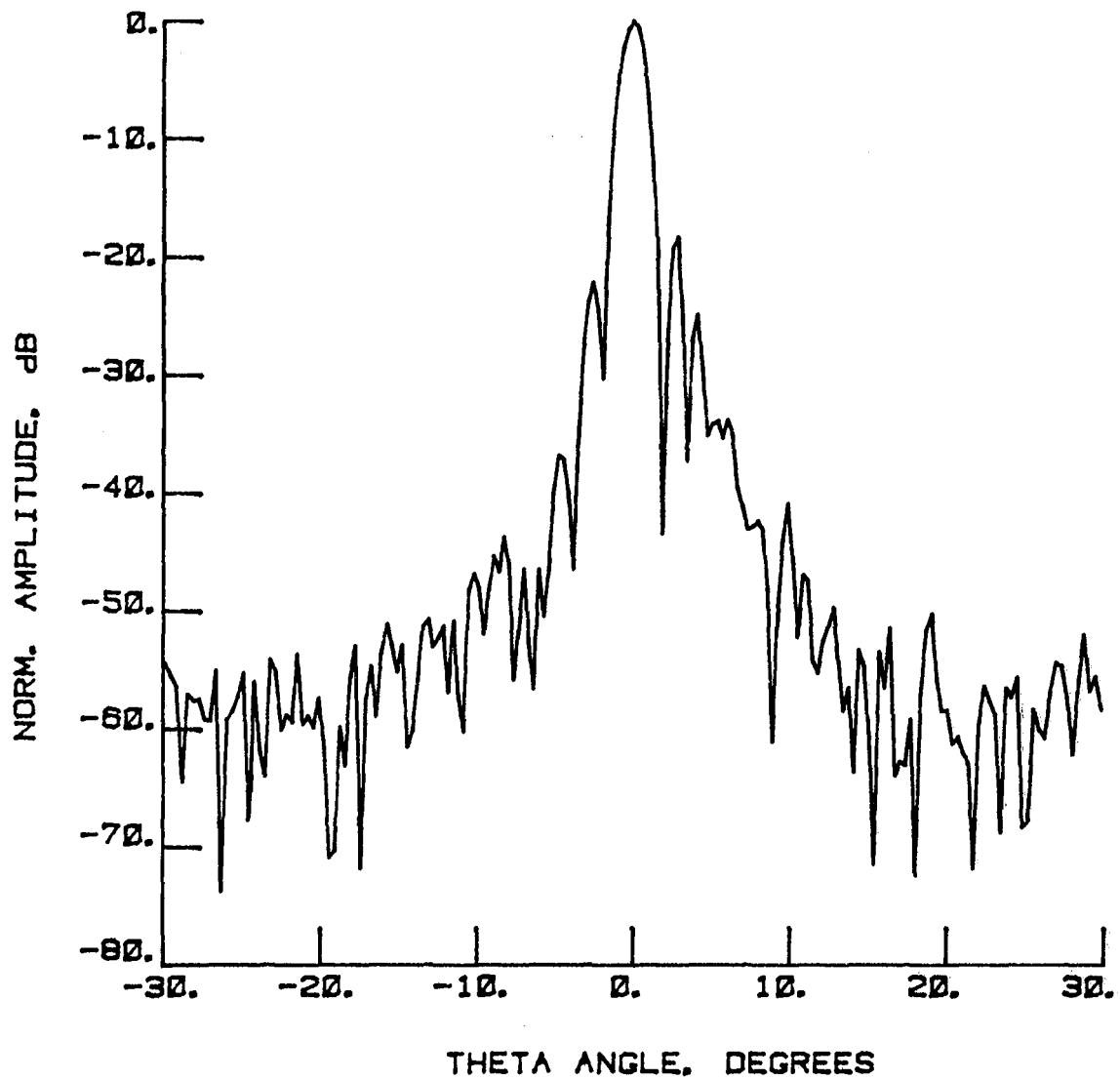
Figure 5-25 Far-Field Pattern, 2.27 GHz, 45° Diagonal, Co-Pol, Test 5, ±30° Scale

62

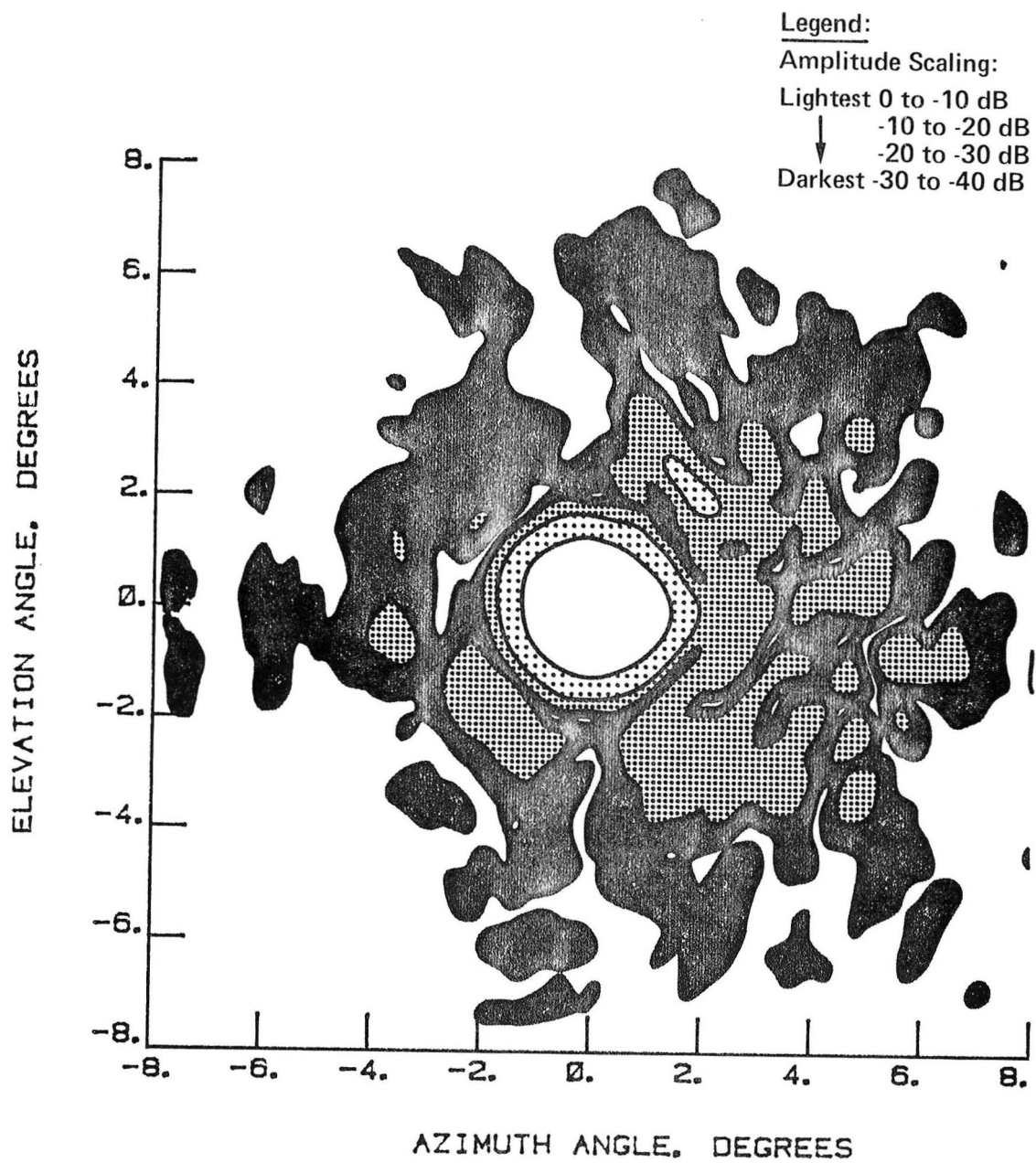This Page Intentionally Left Blank
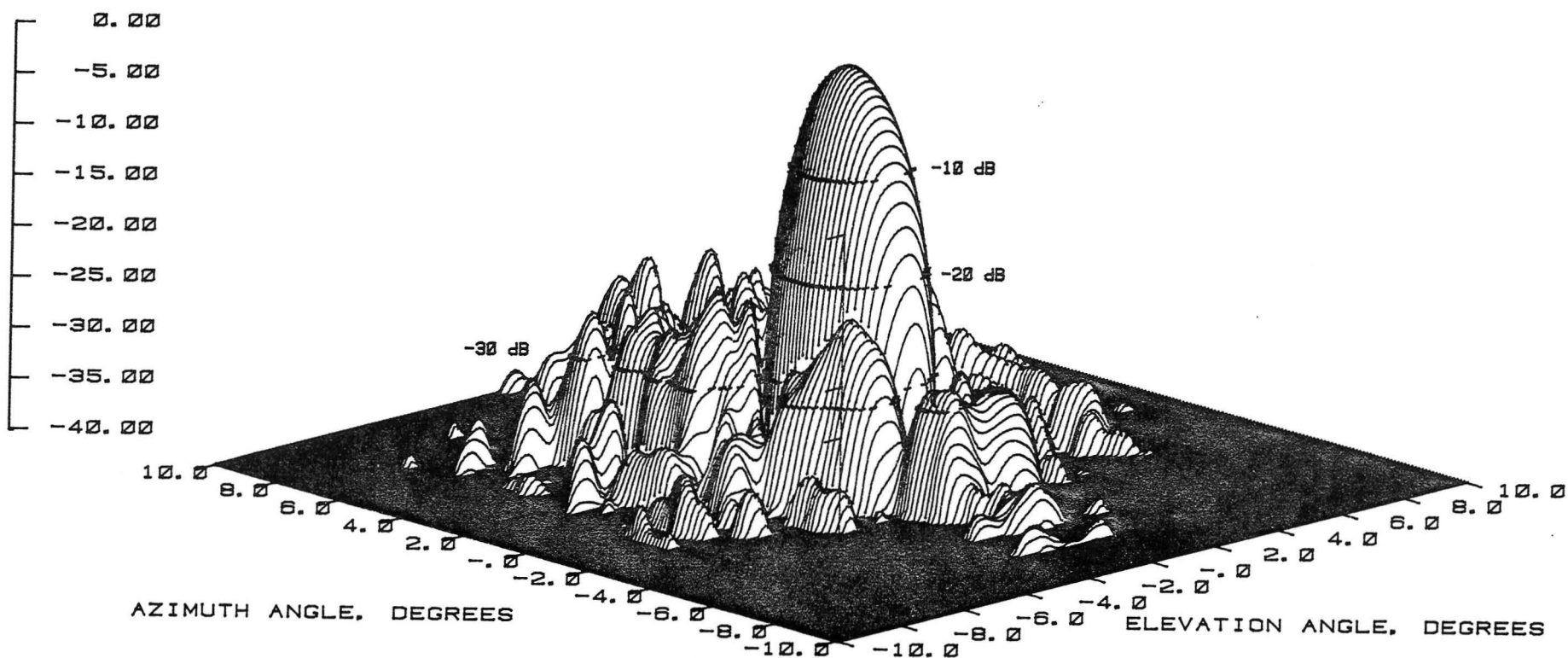
NORMALIZED LOG
AMPLITUDE. dB

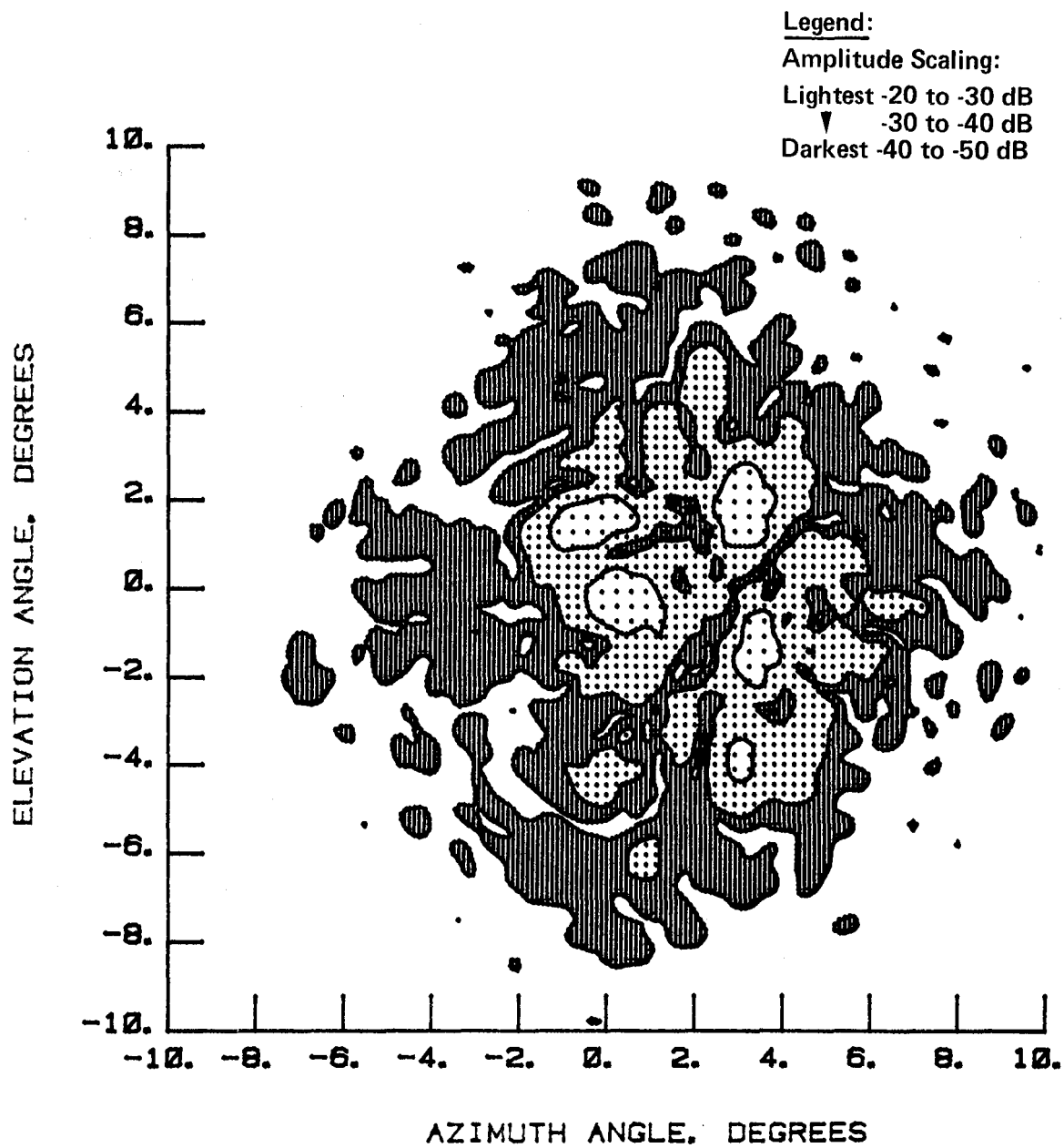Figure 5-27 Far-Field Pattern, 2.27 GHz, 3-D Plot, Co-Pol, Test 5, ±10° Scale

65 and 66

Figure 5-28 Far-Field Contour, 2.27 GHz, Cross-Pol, Test 6, ±10° Scale

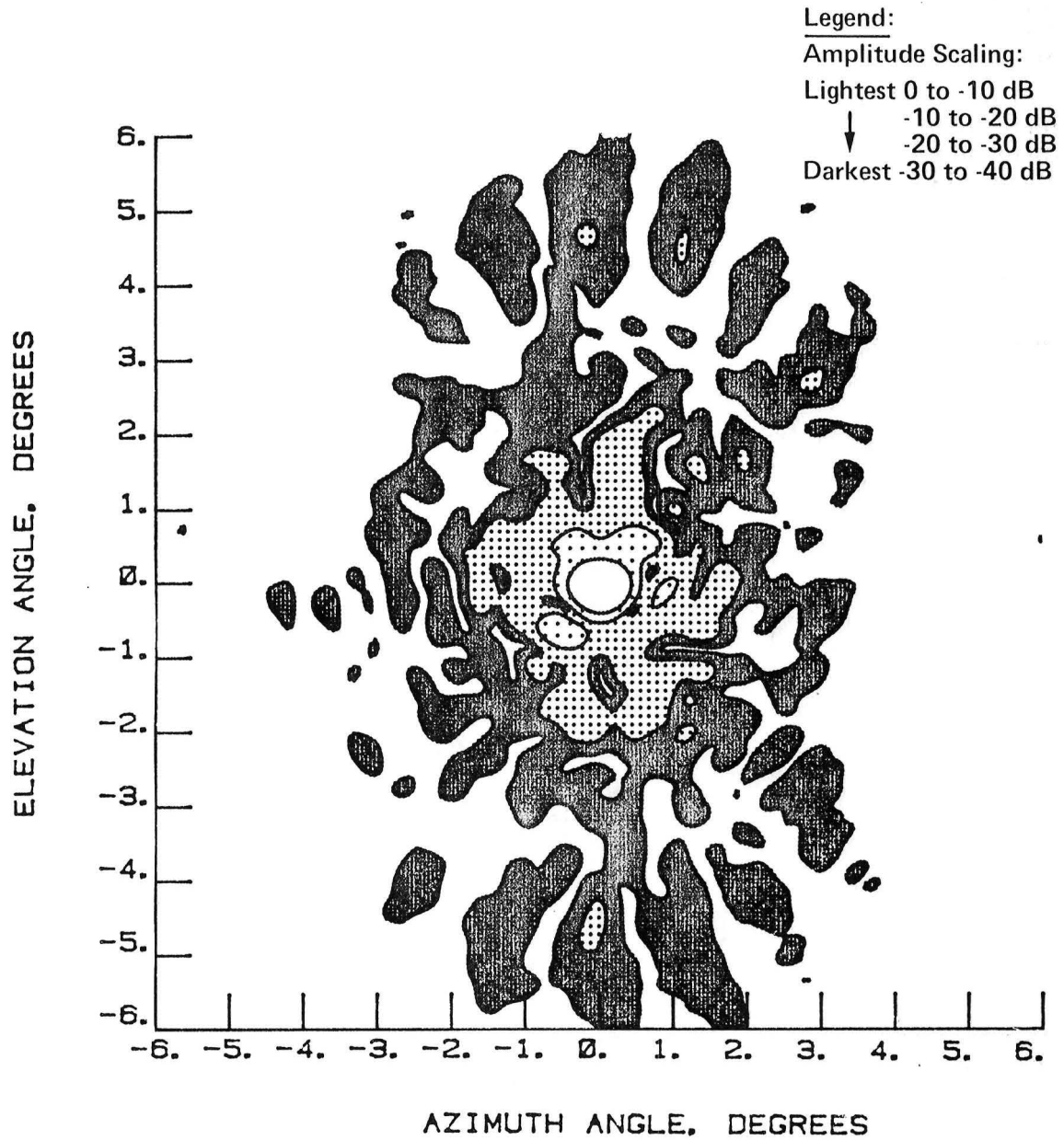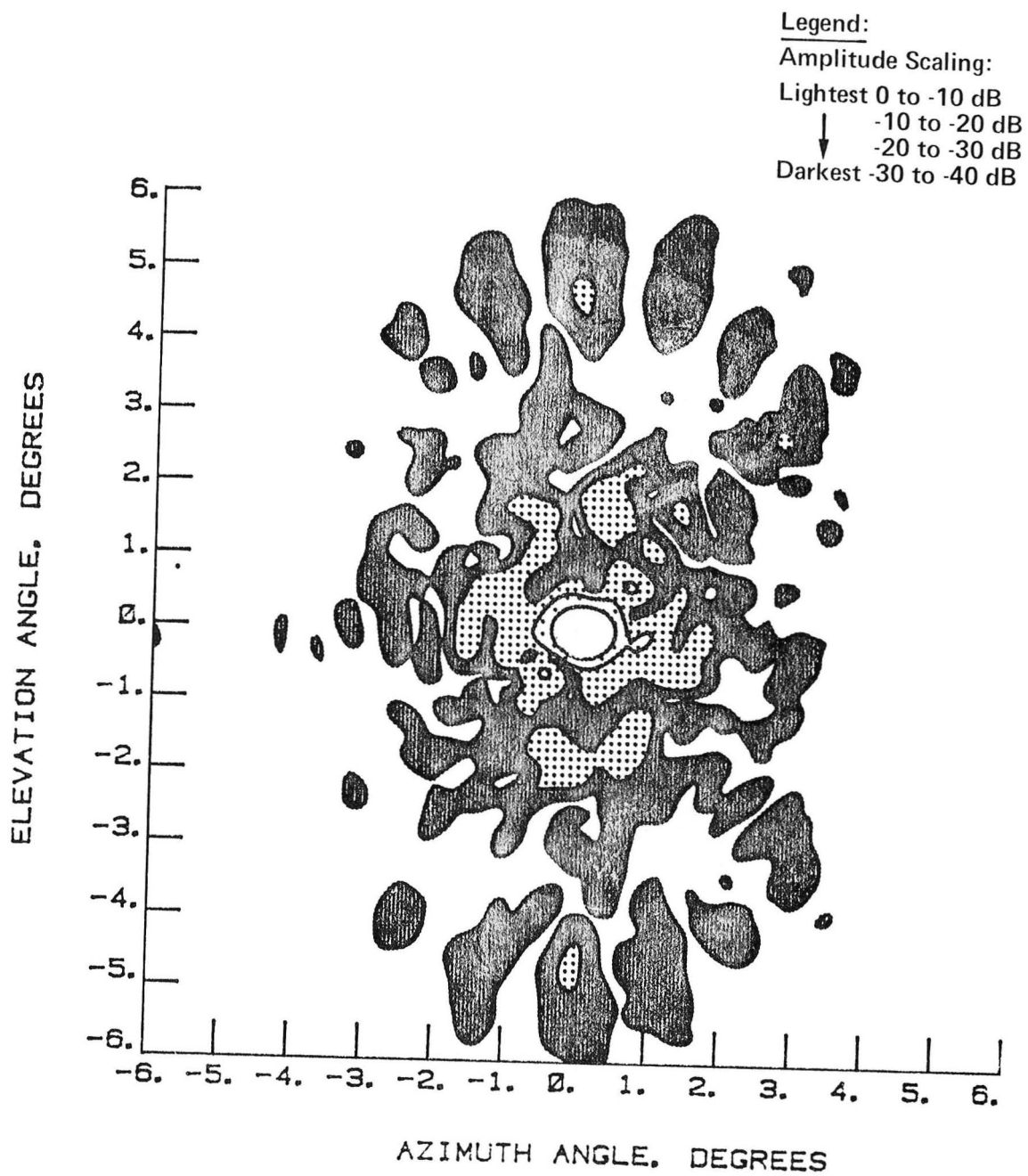*Figure 5-29 Far-Field Pattern Contour, 7.73 GHz, Co-Pol, Test 18, ±6° Scale*

Figure 5-30 Far-Field Contour, 7.73 GHz, Co-Pol, Test 19, ±6° Scale

Figure 5-31 Far-Field Contour, 7.73 GHz, Co-Pol, Test 20, ±6° Scale

Legend:
Amplitude Scaling:
Lightest 0 to -10 dB
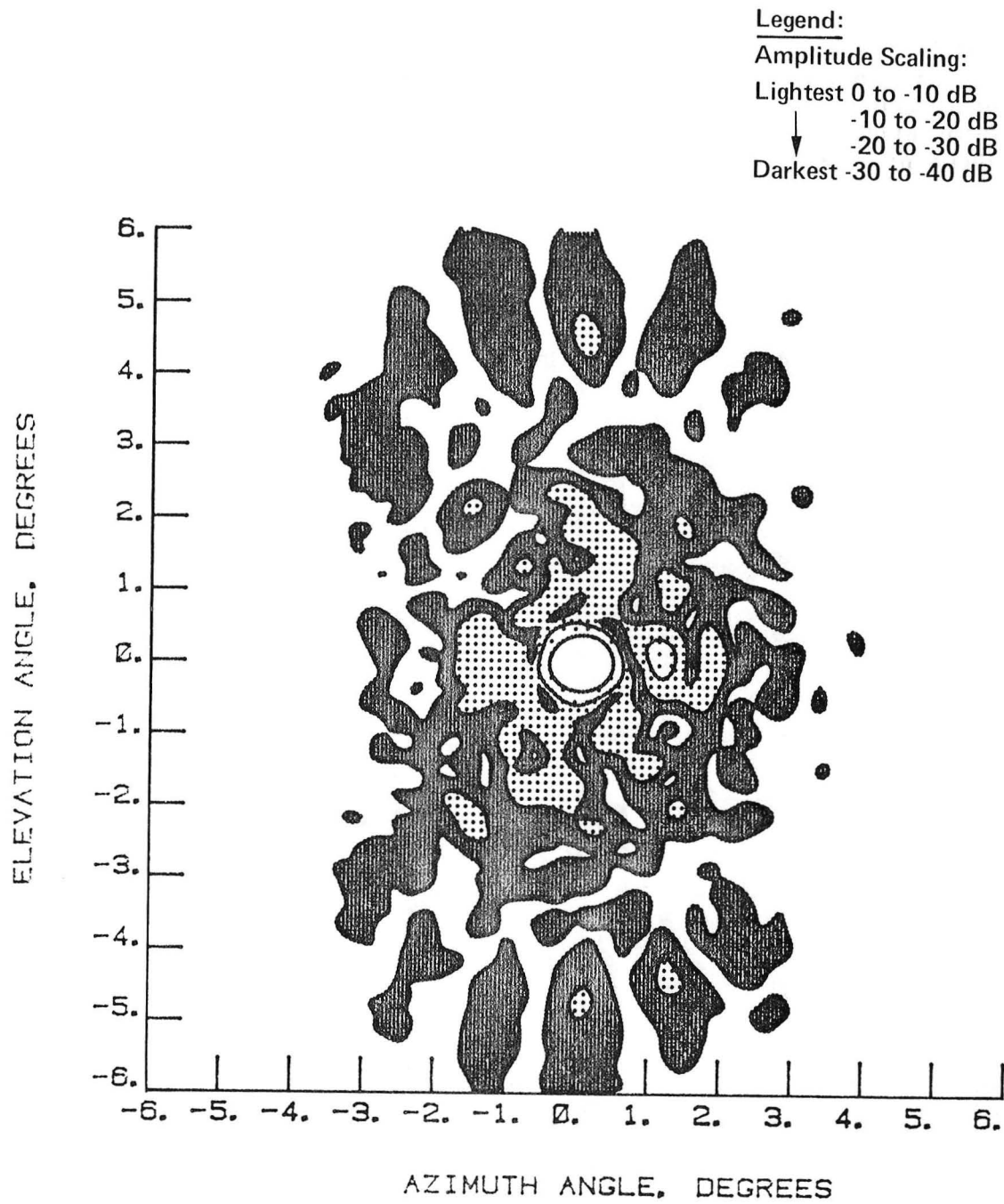   -10 to -20 dB
        -20 to -30 dB
Darkest -30 to -40 dB

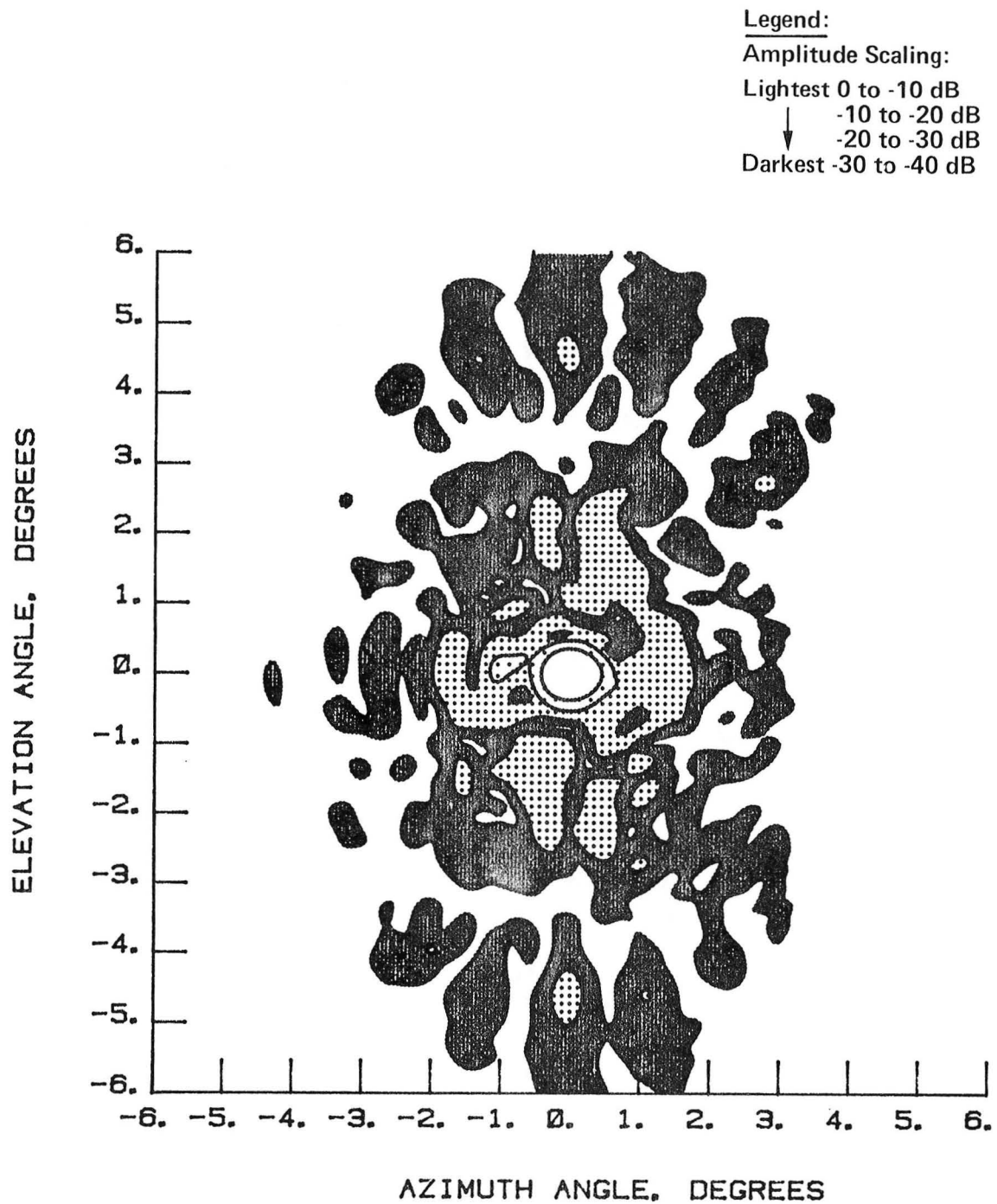*Figure 5-32 Far-Field Contour, 7.73 GHz, Co-Pol, Test 21, ±6° Scale*

71
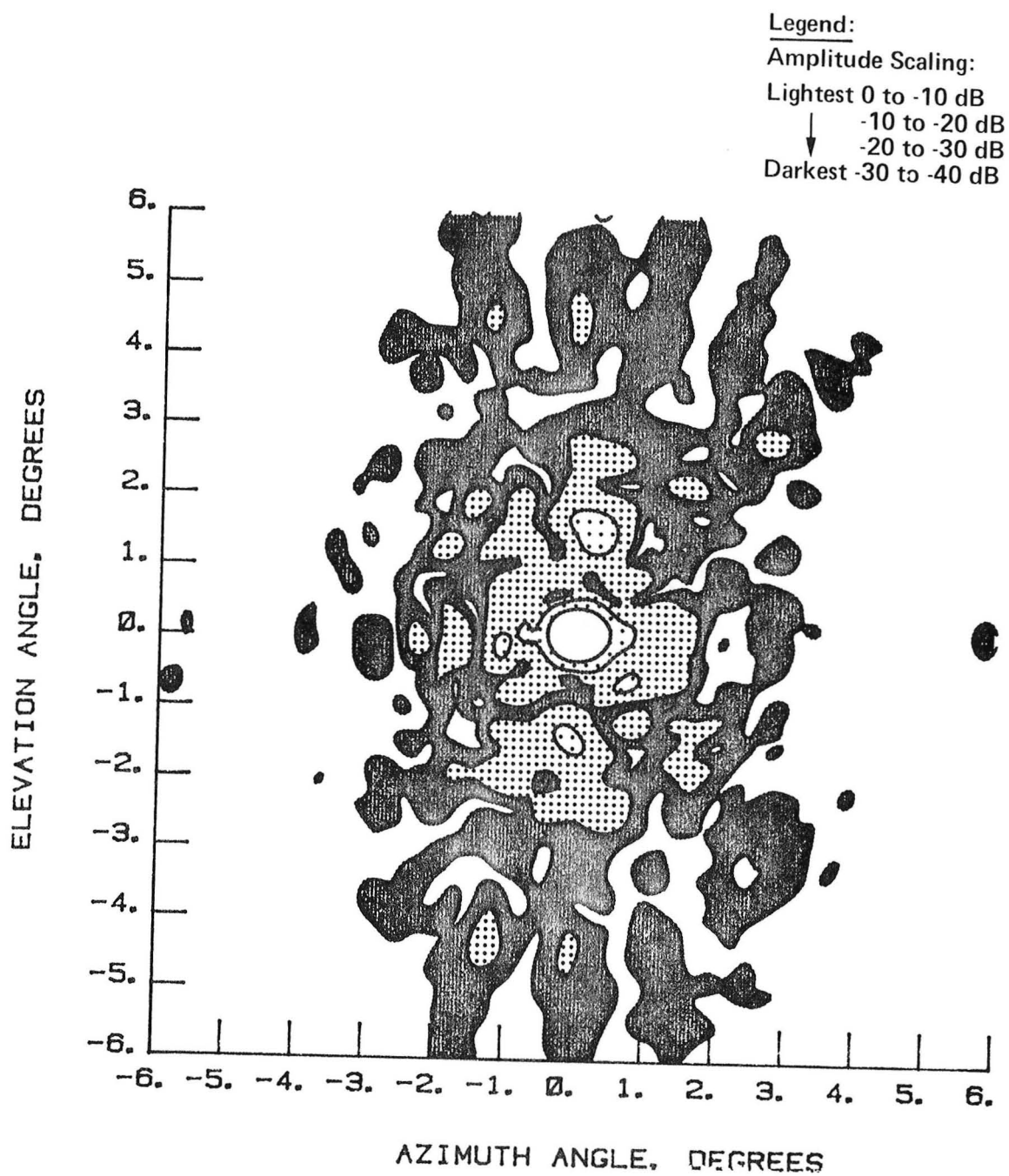
Figure 5-33 Far-Field Contour, 7.73 GHz, Co-Pol, Test 22, ±6° Scale
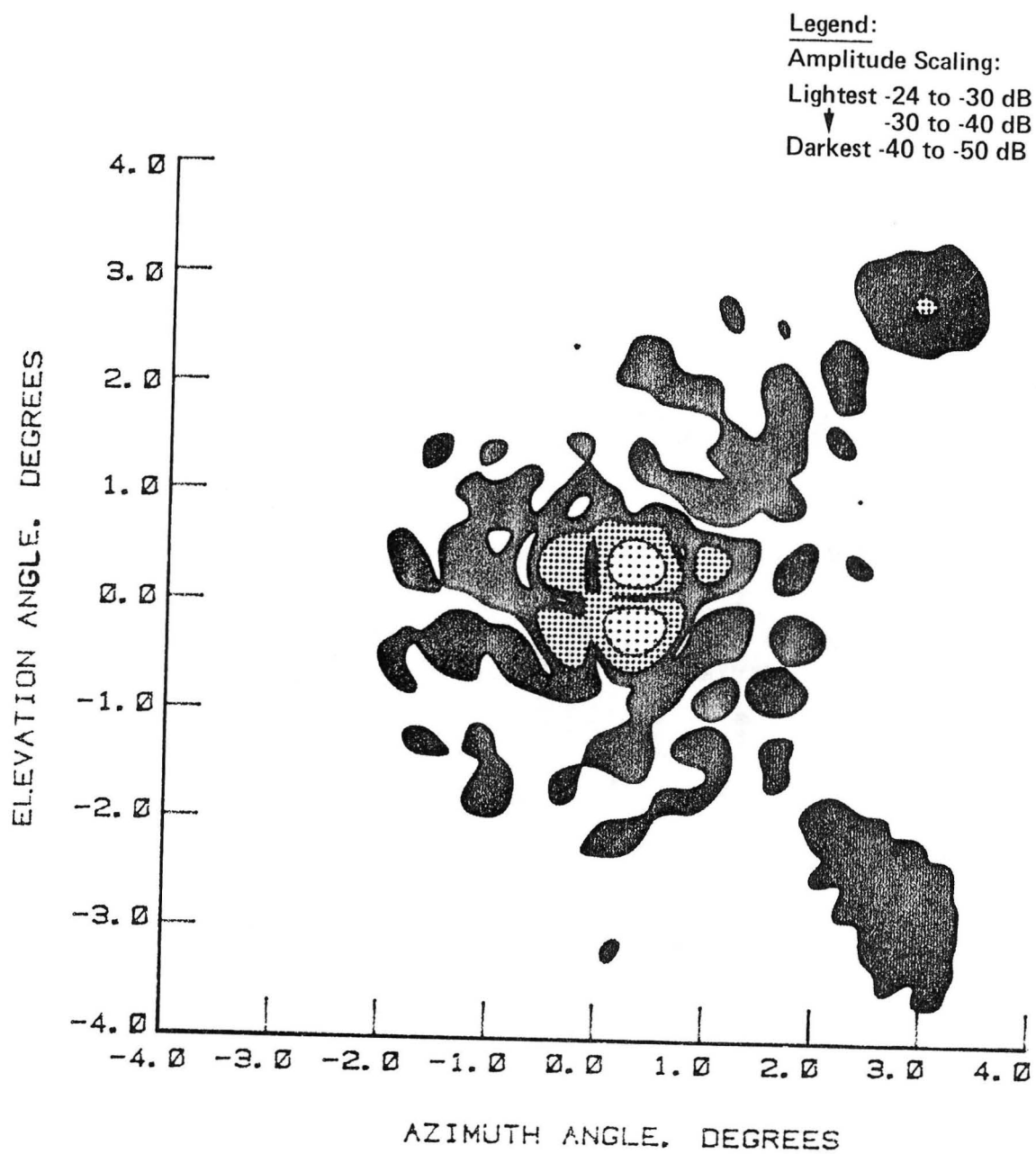
Figure 5-34 Far-Field Contour, 7.73 GHz, Cross-Pol, Test 23, ±4° Scale

73
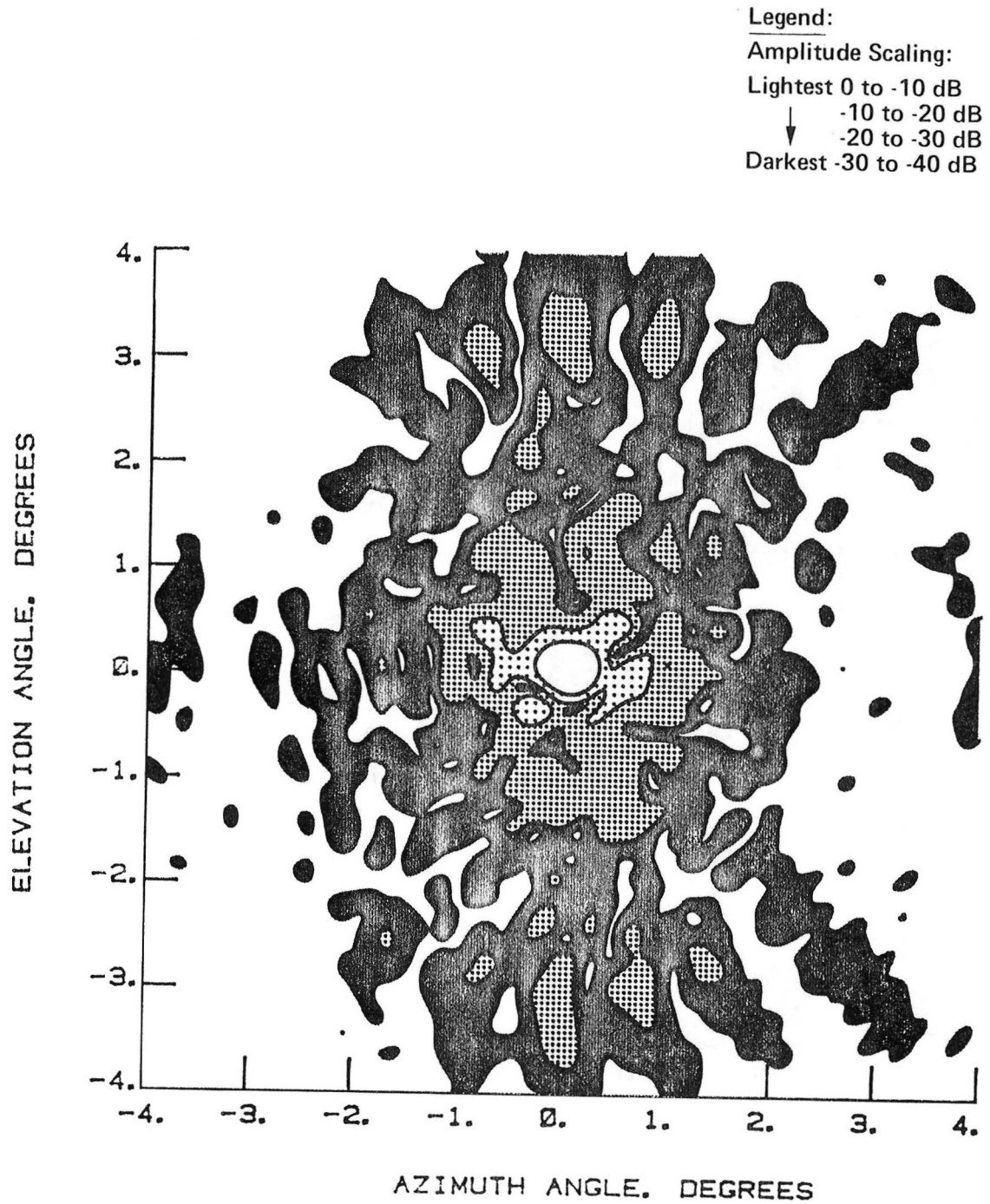
Figure 5-35 Far-Field Contour, 11.6 GHz, Co-Pol, Test 25, ±4° Scale
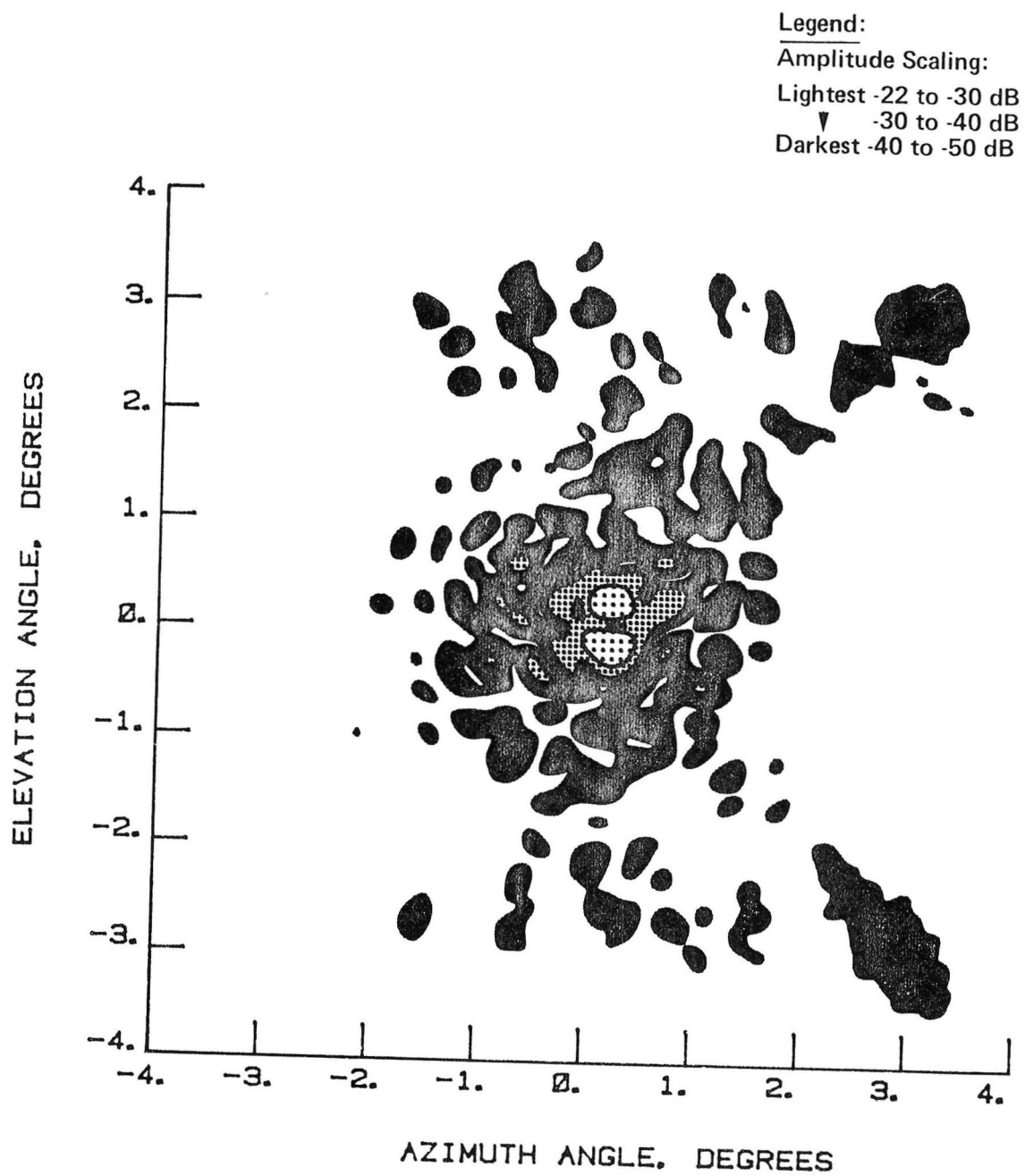
Figure 5-36 Far-Field Contour, 11.6 GHz, Cross-Pol, Test 26, ±4° Scale

MEASUREMENT SAMPLE PLANE

FEED

EFFECT OF
BLISTER ON
PHASE

PROJECTED SAMPLE PLANE

BLISTER

REFLECTOR SURFACE
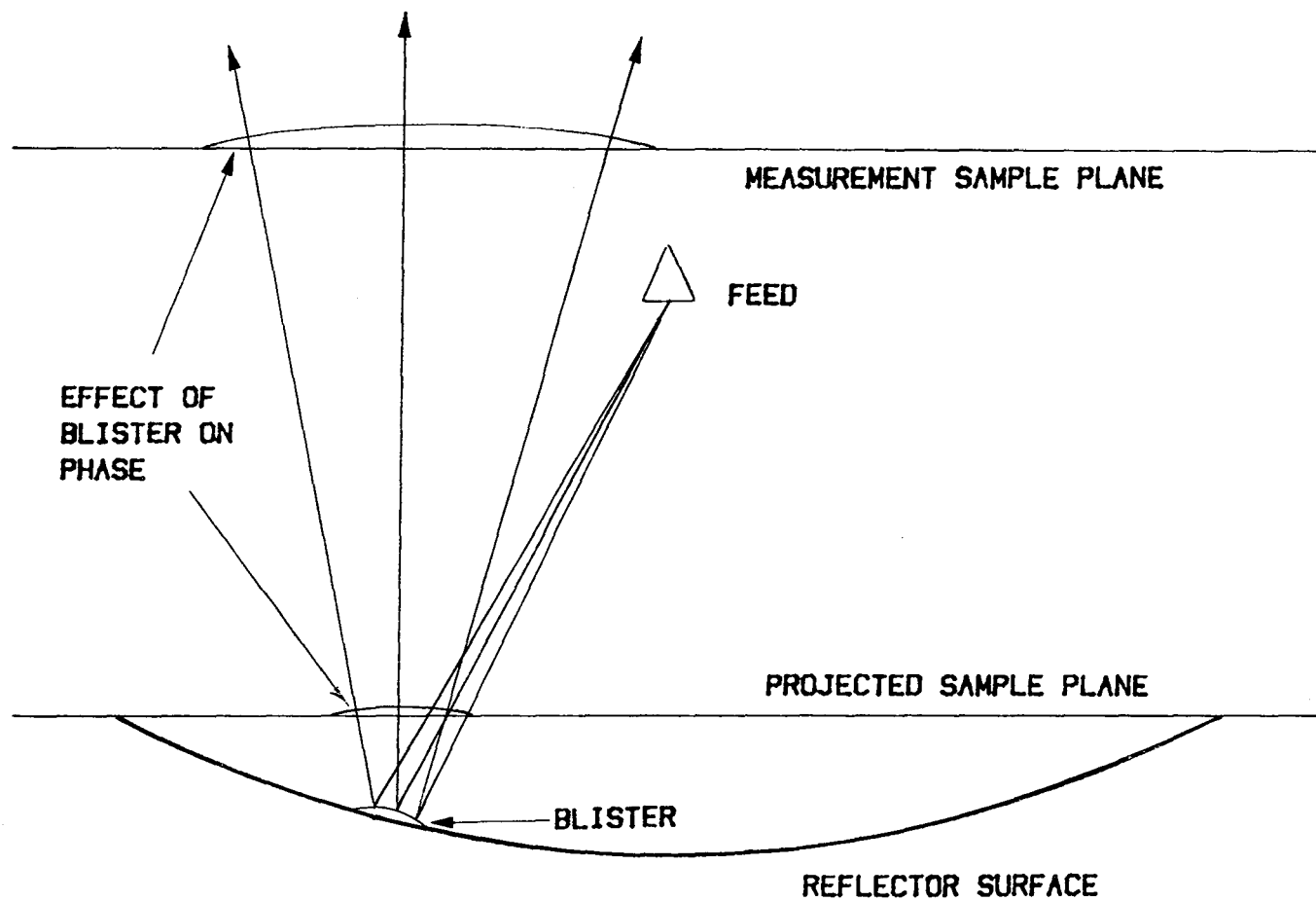
Figure 5-37 Sample Plane Projection

Legend:
Phase Scaling:
Darkest -60 to -30°
-30 to 0°
0 to 30°
Lightest 30 to 60°
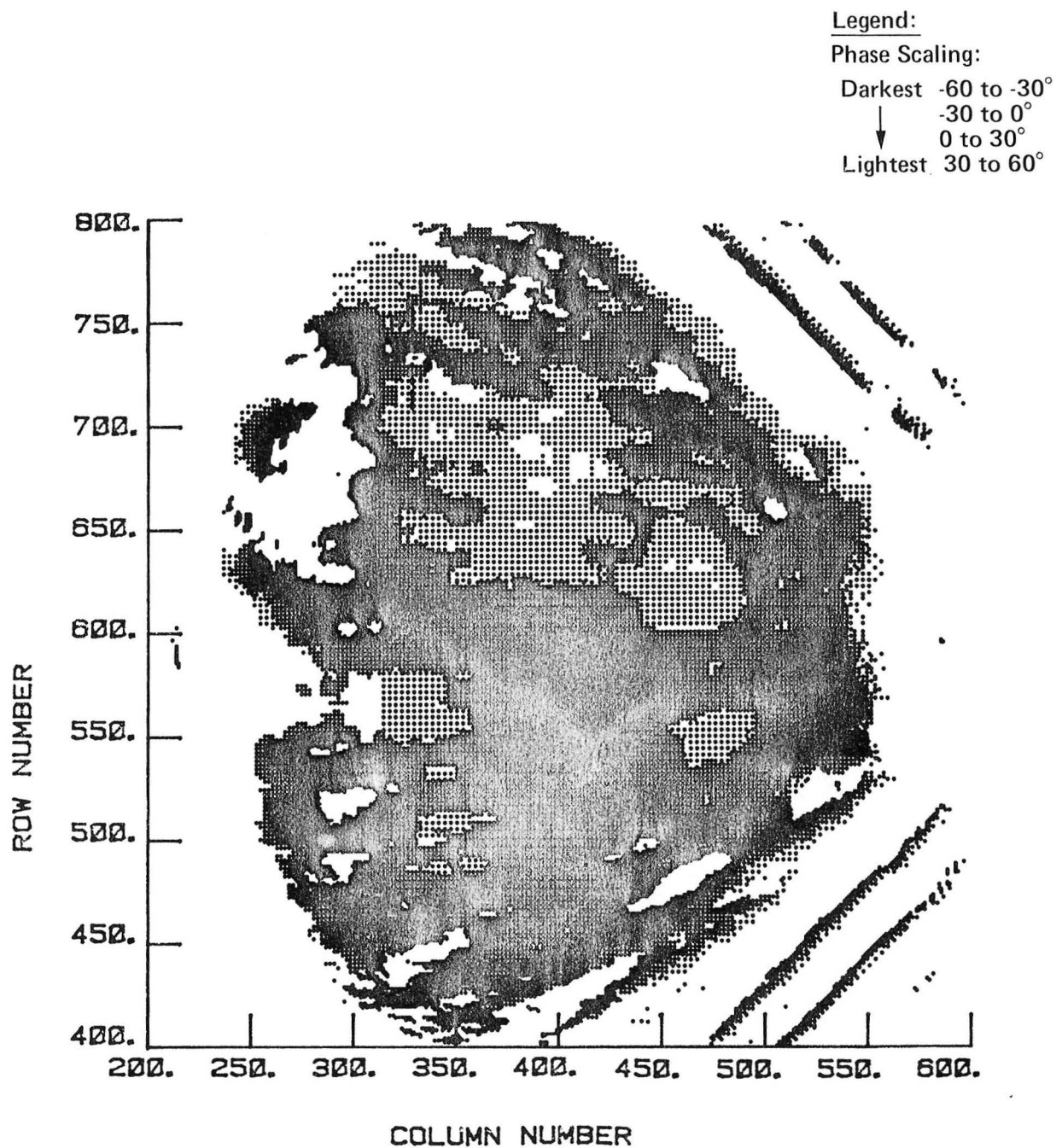
Figure 5-38
Near-Field Phase Contour in the Near-Field Measurement Plane (31.2 ft above the Plane of the Hoop)
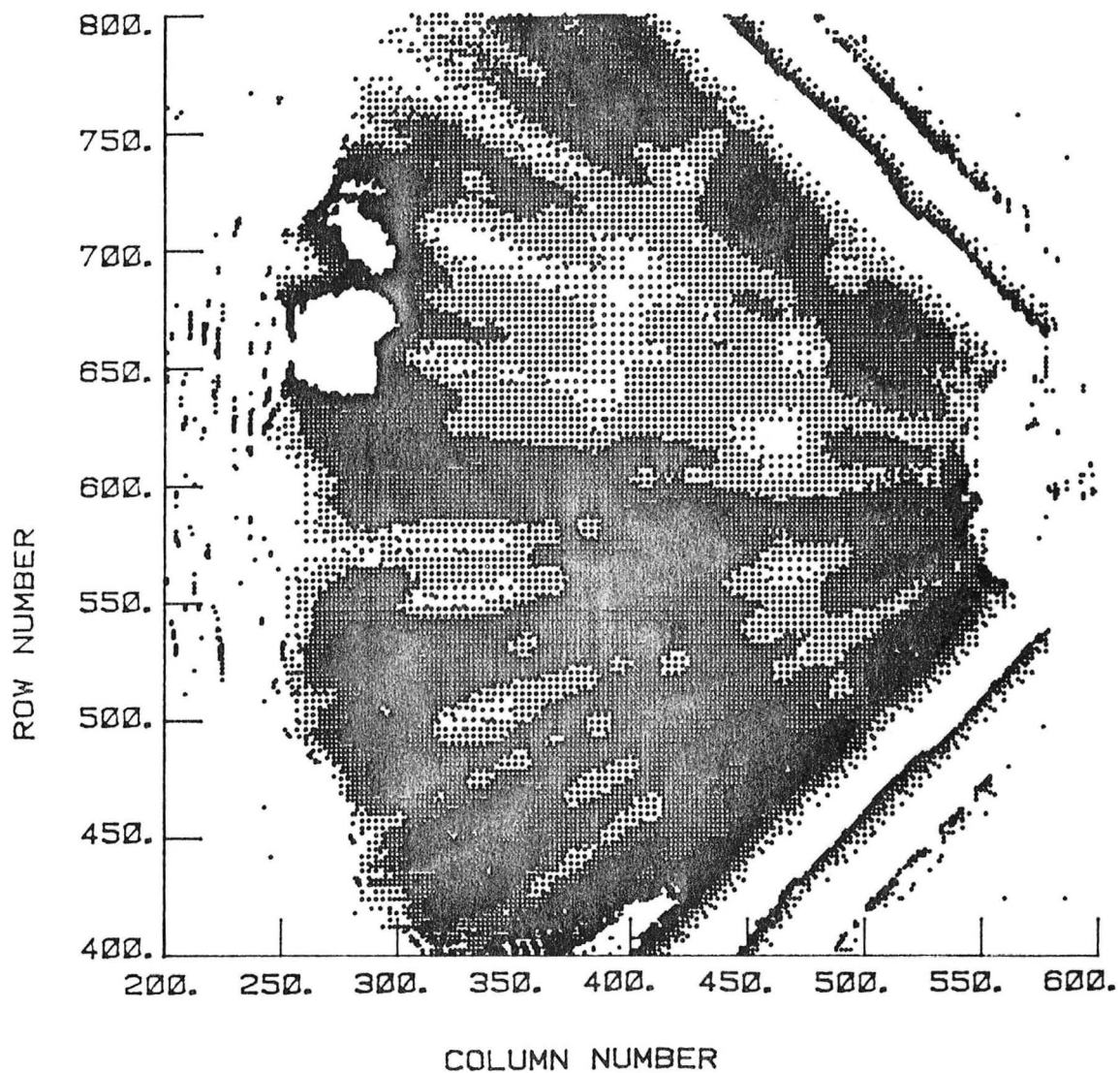
Figure 5-39 Near-Field Phase Contour Projected into the Aperture Plane (Plane of the Hoop)

PATH LENGTH
DIFFERENCE ≈ 2d

SAMPLE PLANE

INCIDENT RAY
FROM FEED

BLISTER WITH
MAXIMUM THICKNESS = d

IDEAL REFLECTOR
SURFACE
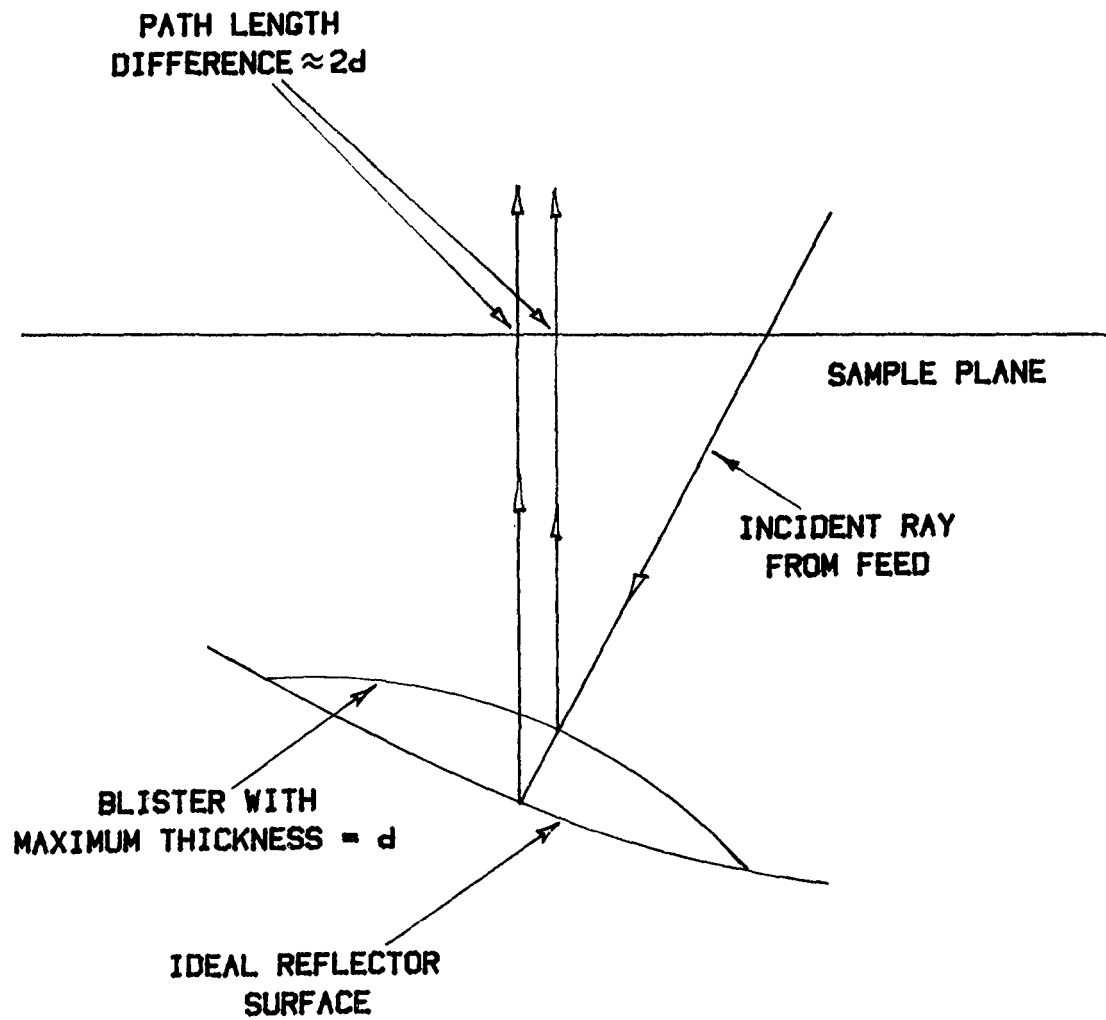
Figure 5-40
Conversion of Projected Phase into Surface Deviation Relative to an Ideal Parabolid

PRIMARY
APERTURE

PARASITIC
APERTURES

REFLECTIVE
MESH
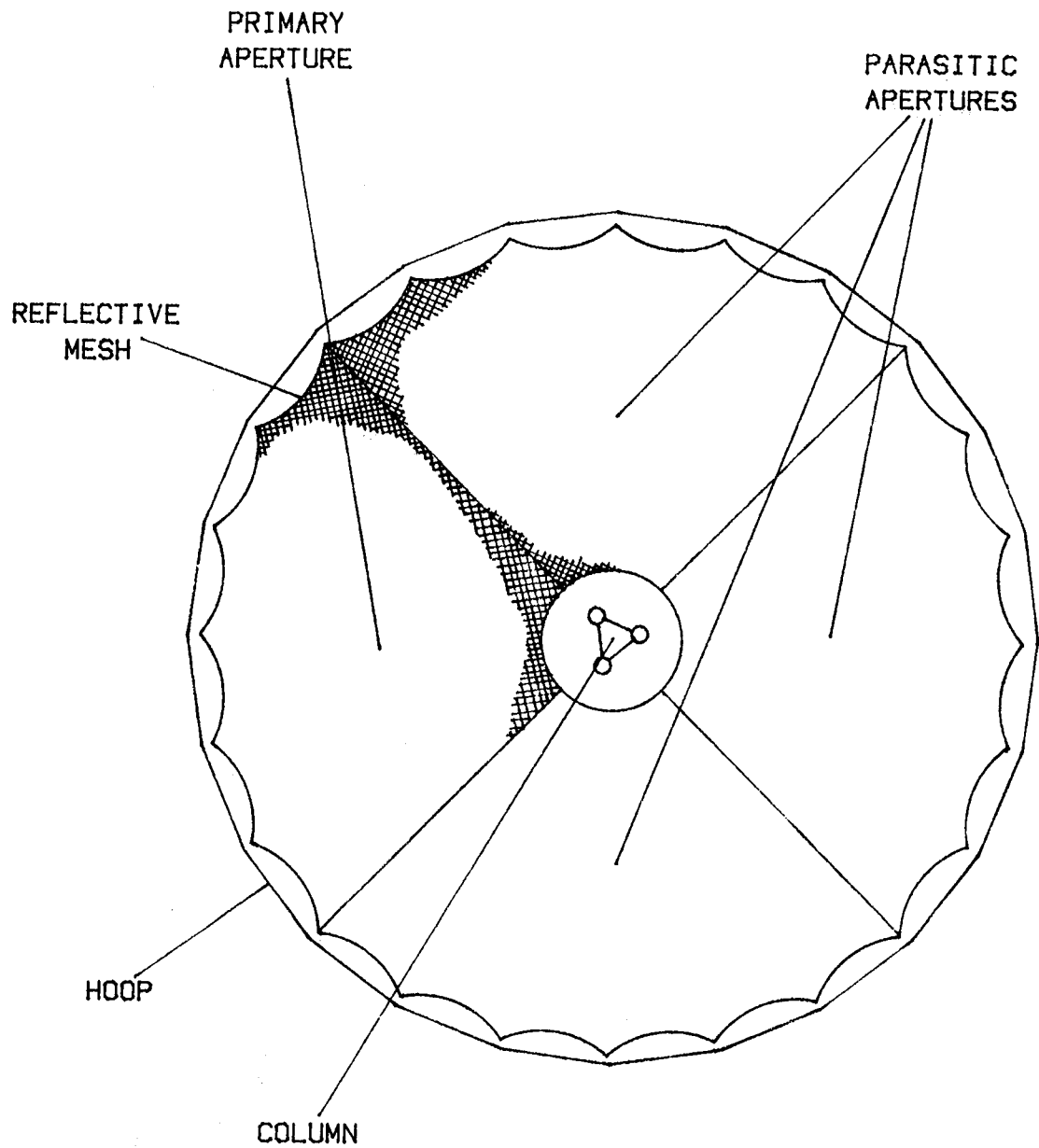
HOOP

COLUMN

Figure 5-41 Quad Aperture Arrangement in the Hoop Column Antenna
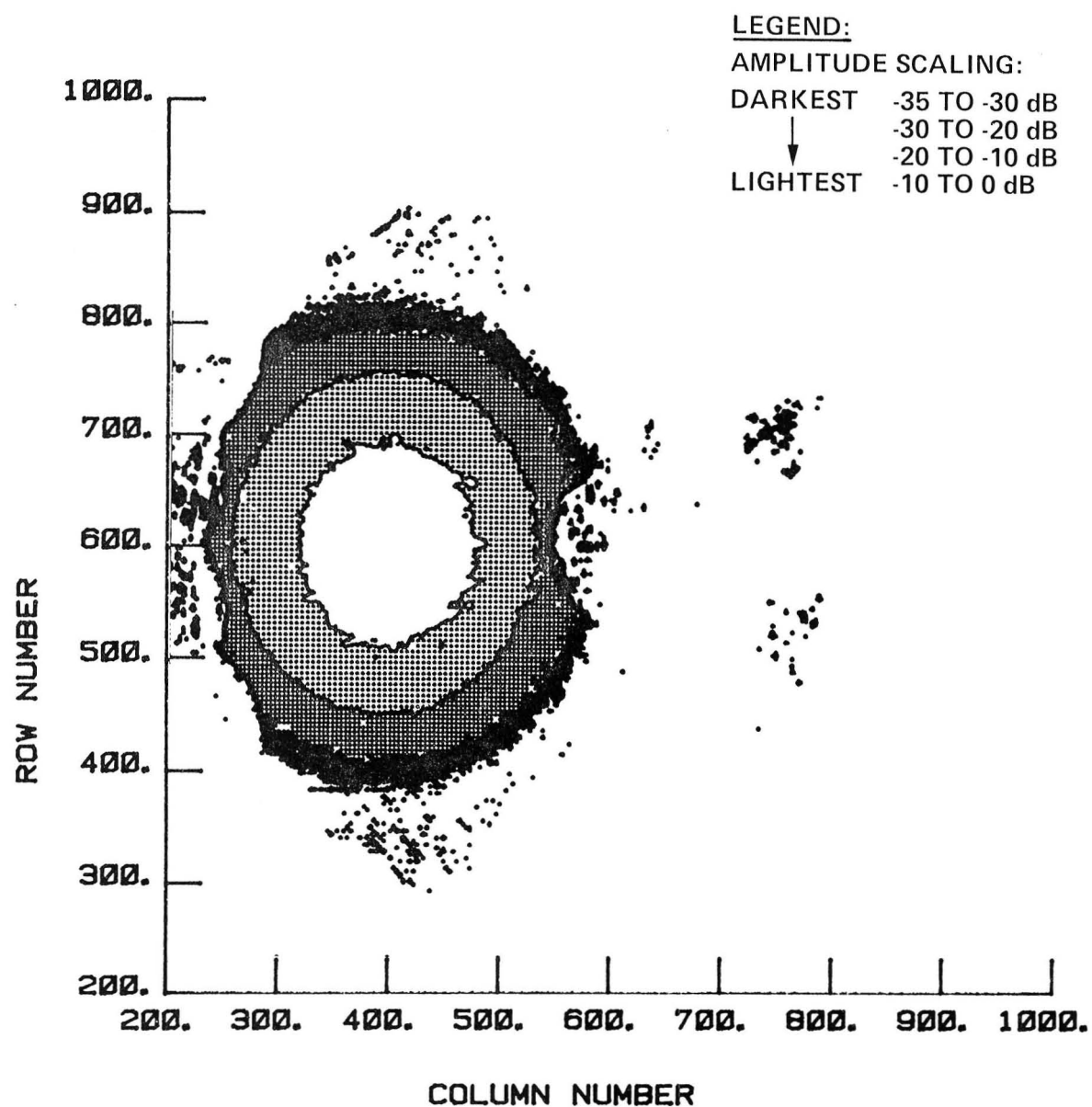
Figure 5-42 Near-Field Amplitude Contour Projected into the Plane of the Hoop (All Four Apertures)

81
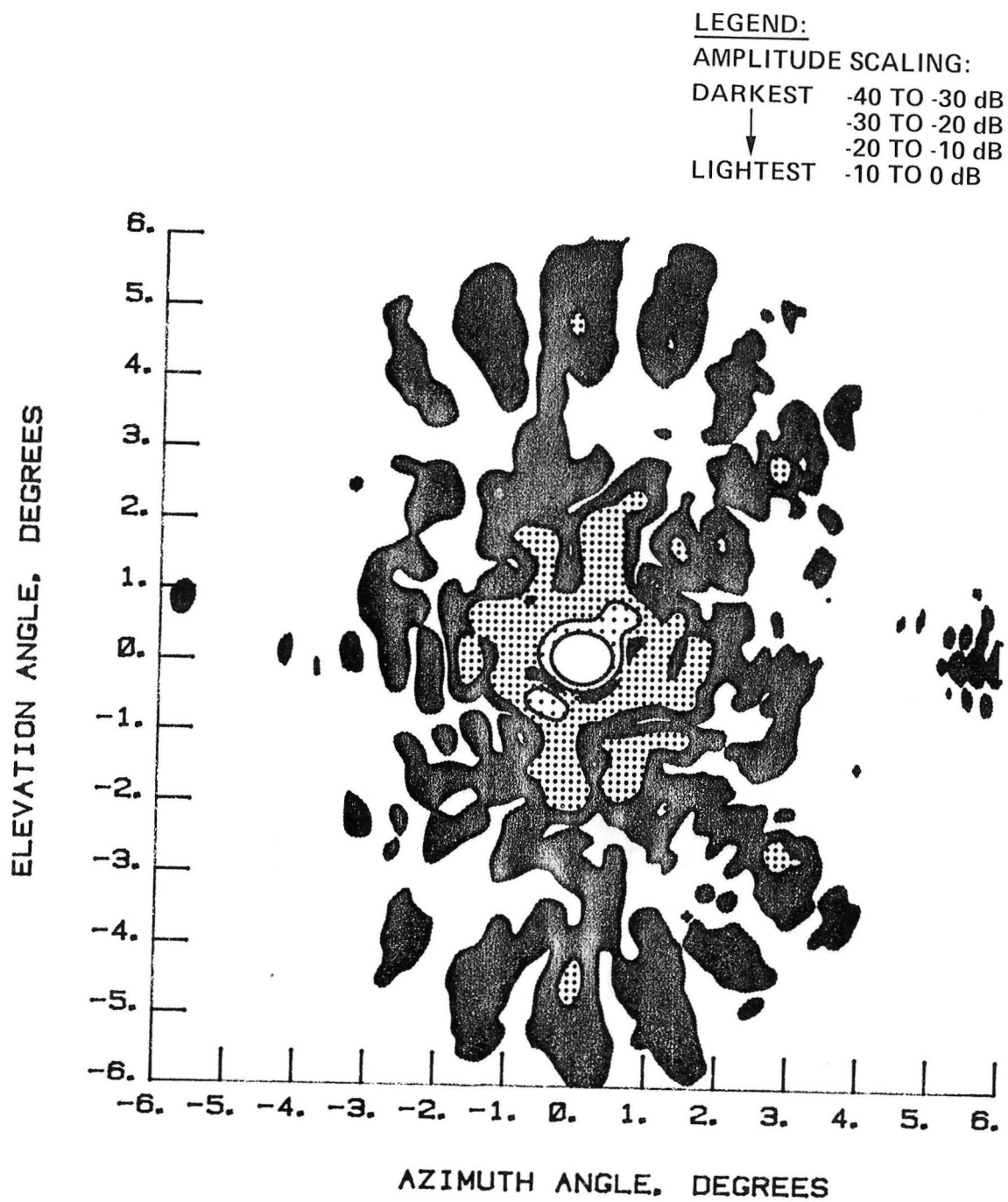
Figure 5-43 Far-Field Amplitude Contour, Total Contribution from All Four Apertures

82

LEGEND:
AMPLITUDE SCALING:
DARKEST   -35 TO -30 dB
           -30 TO -20 dB
           -20 TO -10 dB
LIGHTEST   -10 TO 0 dB
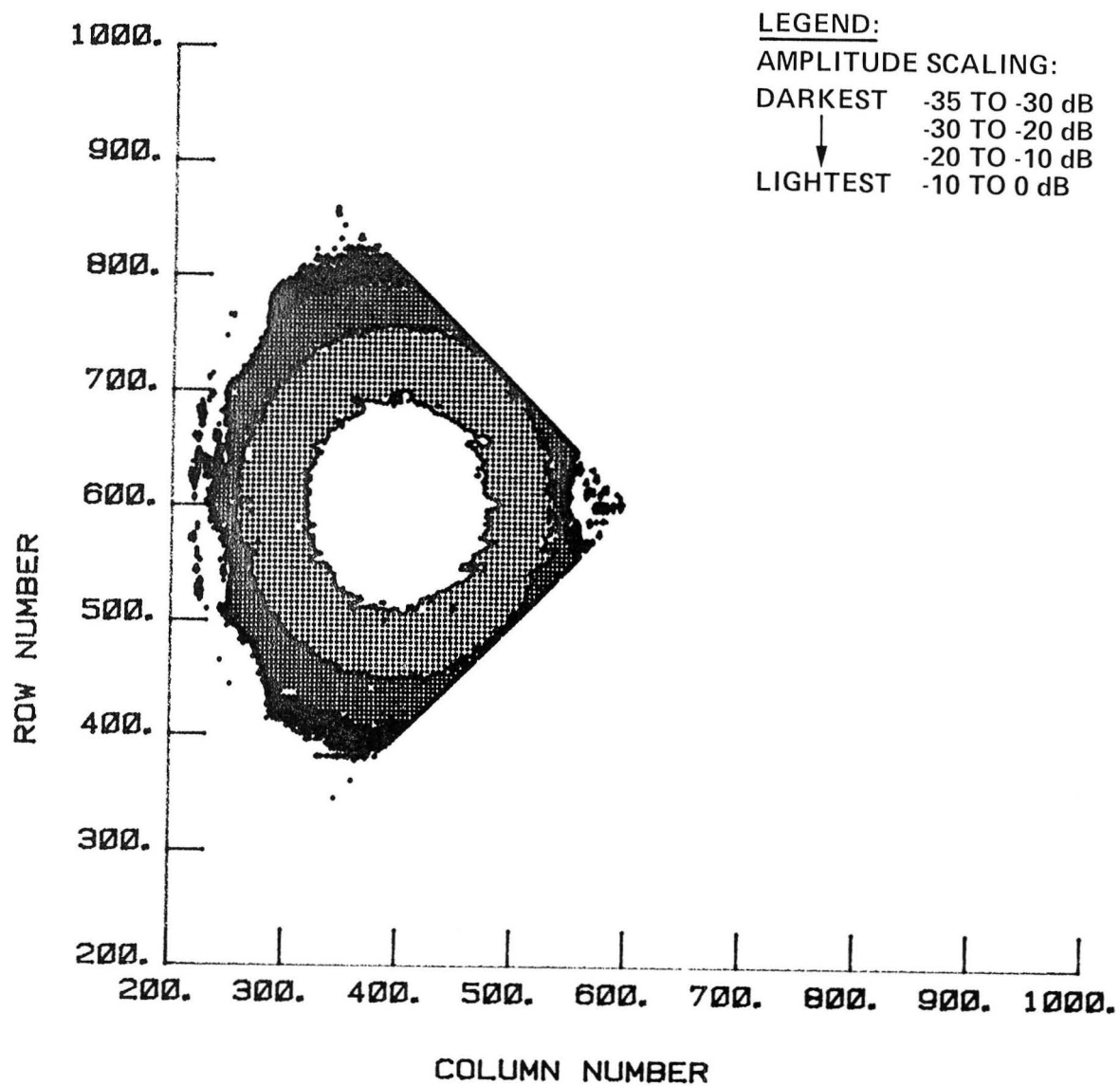
Figure 5-44 Near-Field Amplitude Contour Projected into the Plane of the Hoop Truncated to Include the Principal Quadrant Only

83

LEGEND:
AMPLITUDE SCALING:
DARKEST   -40 TO -30 dB
          -30 TO -20 dB
          -20 TO -10 dB
LIGHTEST -10 TO 0 dB

ELEVATION ANGLE. DEGREES

AZIMUTH ANGLE. DEGREES
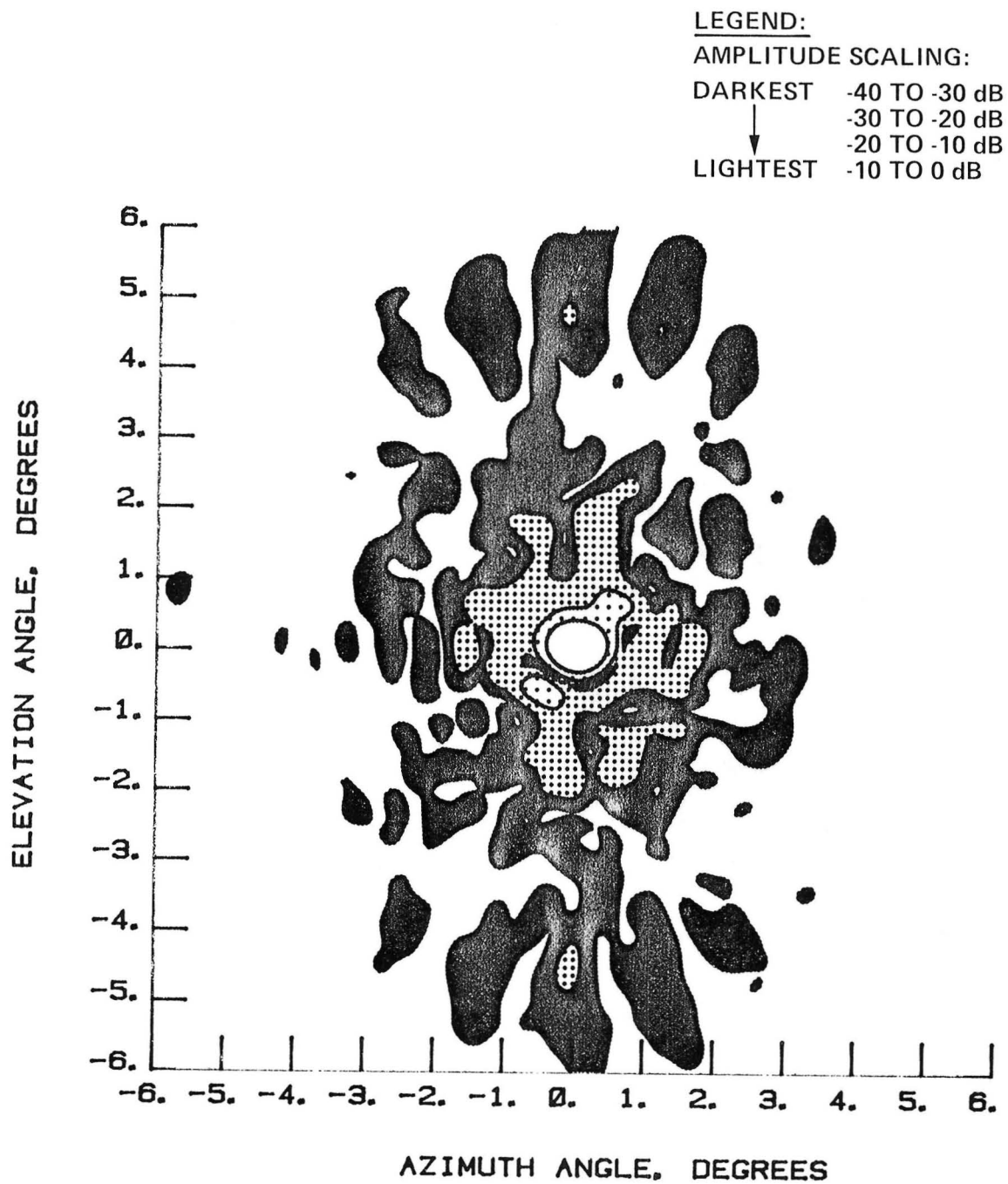
Figure 5-45 Far-Field Amplitude Contour, Principal Quadrant Contribution Only

84
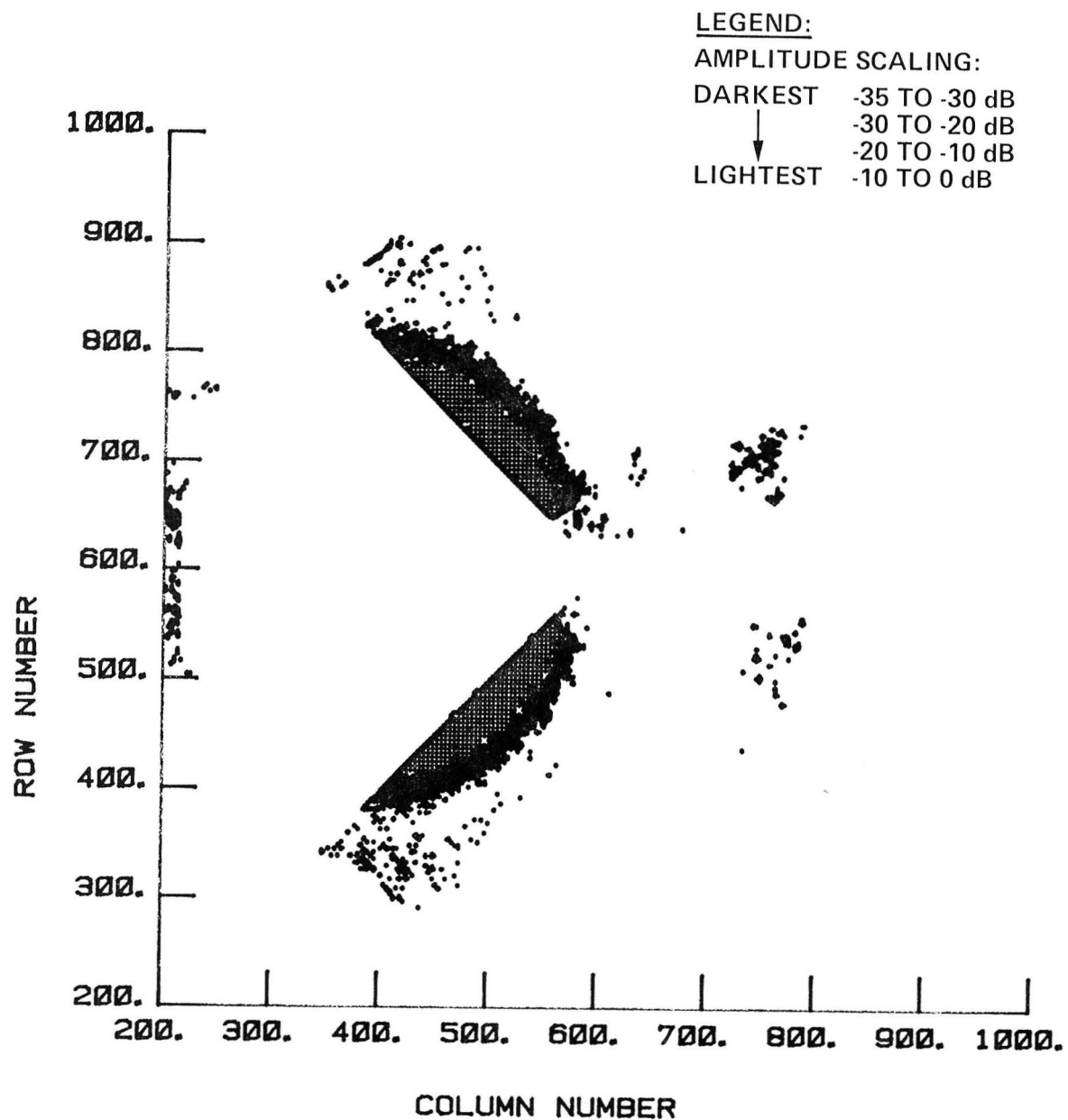
Figure 5-46 *Near-Field Amplitude Contour Projected into the Plane of the Hoop Truncated to Include Parasitic Quadrants Only*
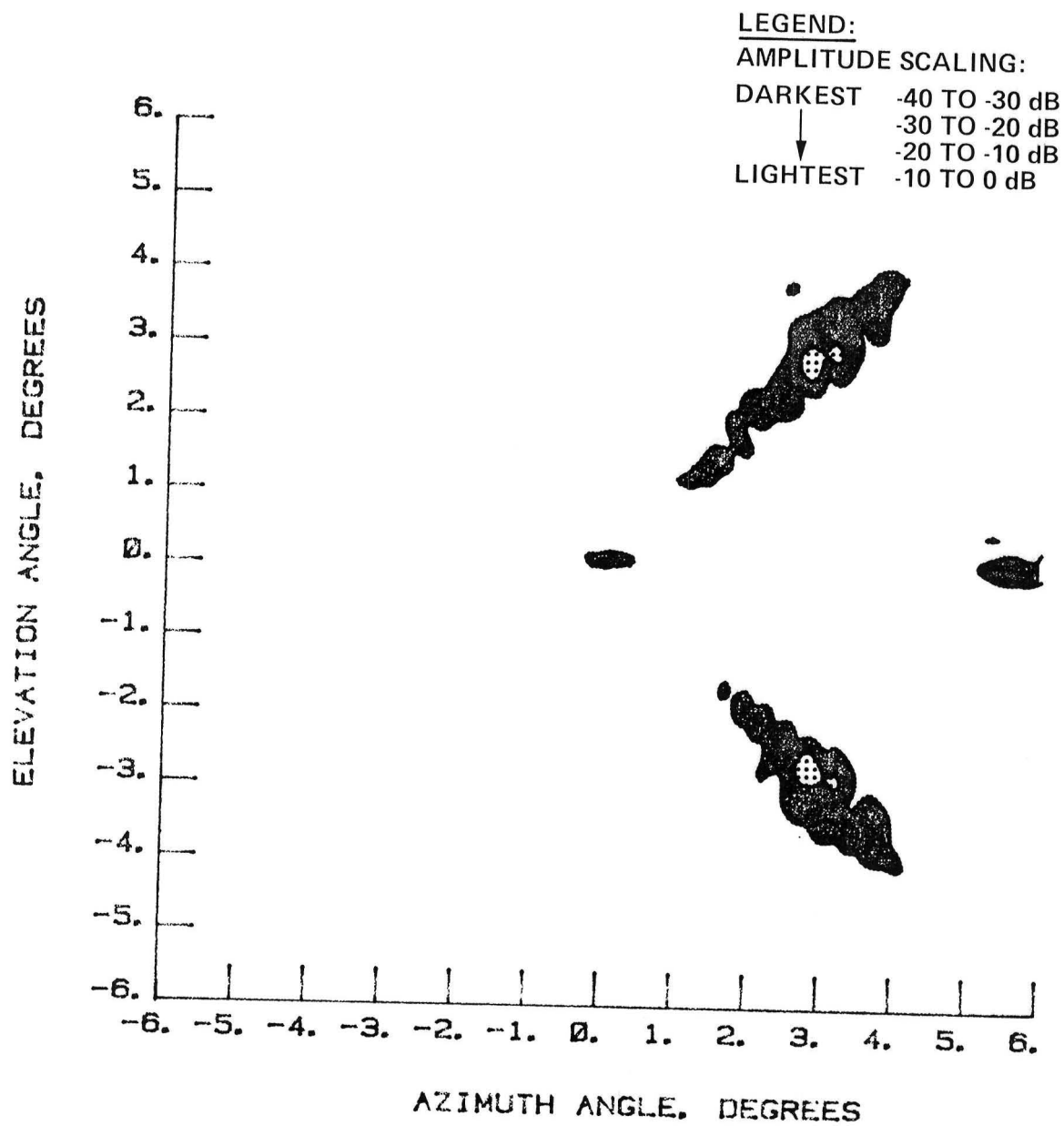
Figure 5-47 *Far-Field Amplitude Contour, Parasitic Quadrant Contribution Only*

86
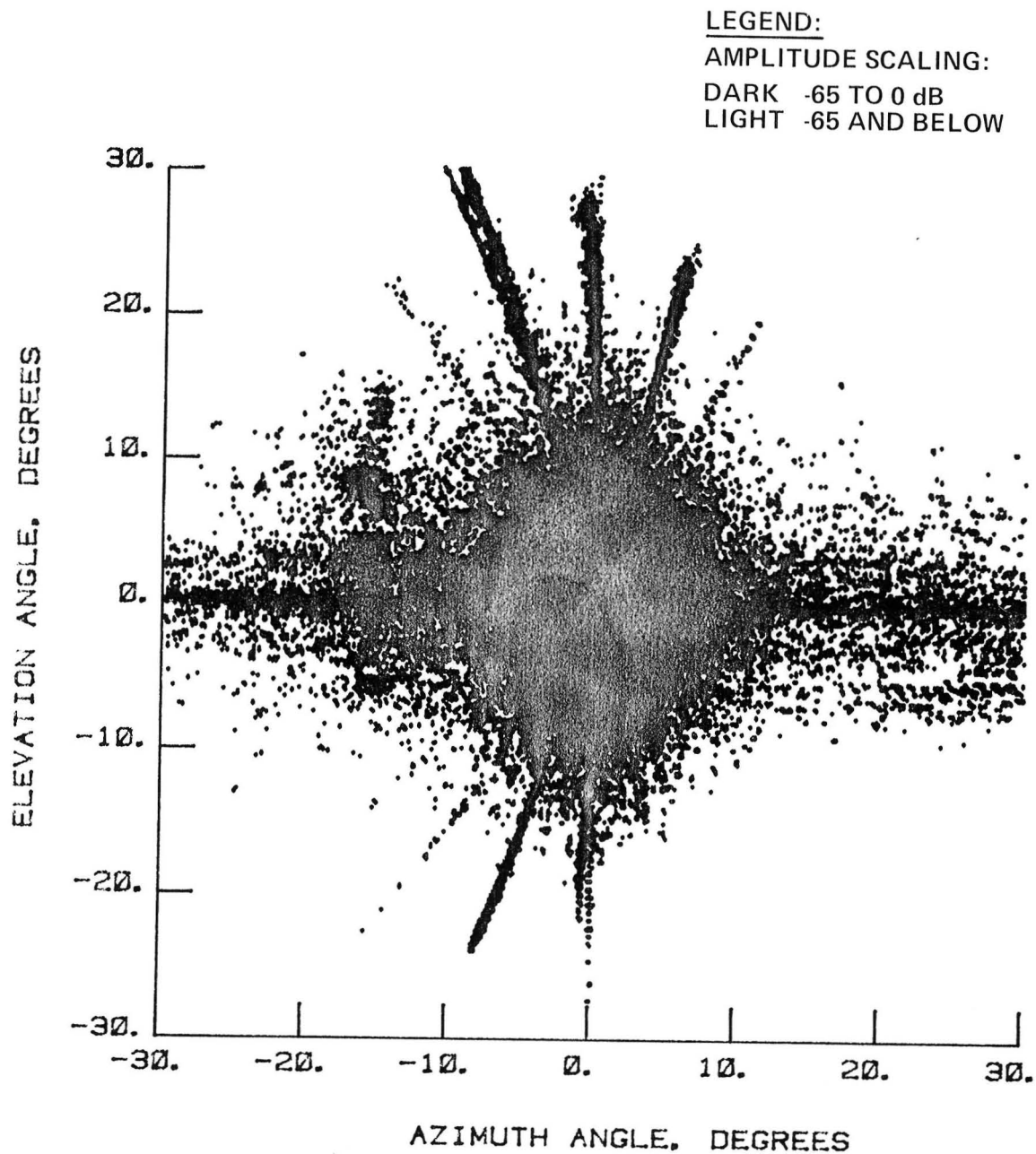
Figure 5-48
Far-Field Contour Plot of the Co-Polarized Component over 0 to 65dB Dynamic Range
Illustrating Quartz Control Cord Scattering at 11.6 GHz
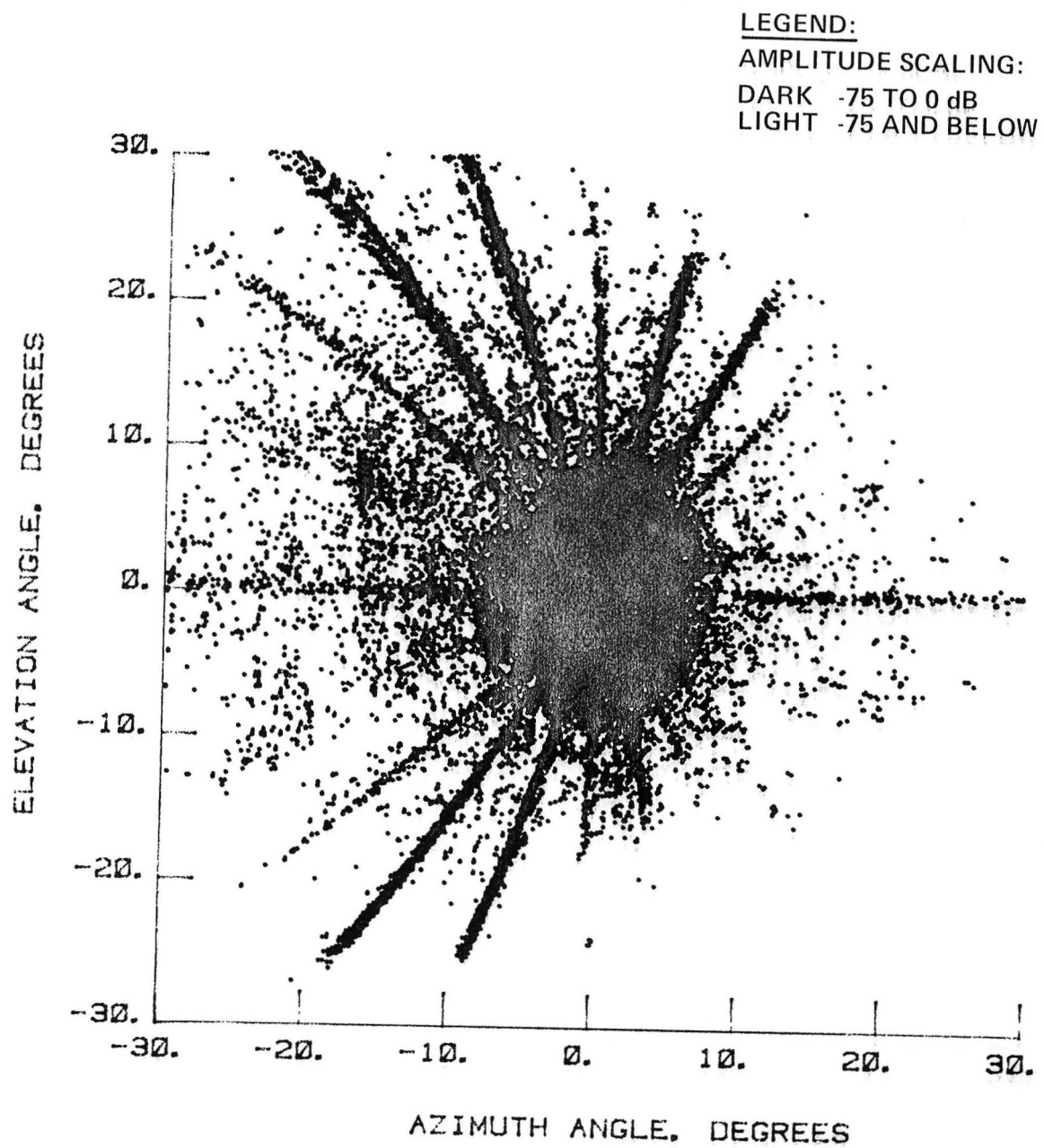
Figure 5-49
*Far-Field Contour of the Cross-Polarized Component over 0 to -75dB Dynamic Range
Illustrating Quartz Control Cord Scattering at 11.6 GHz*

88
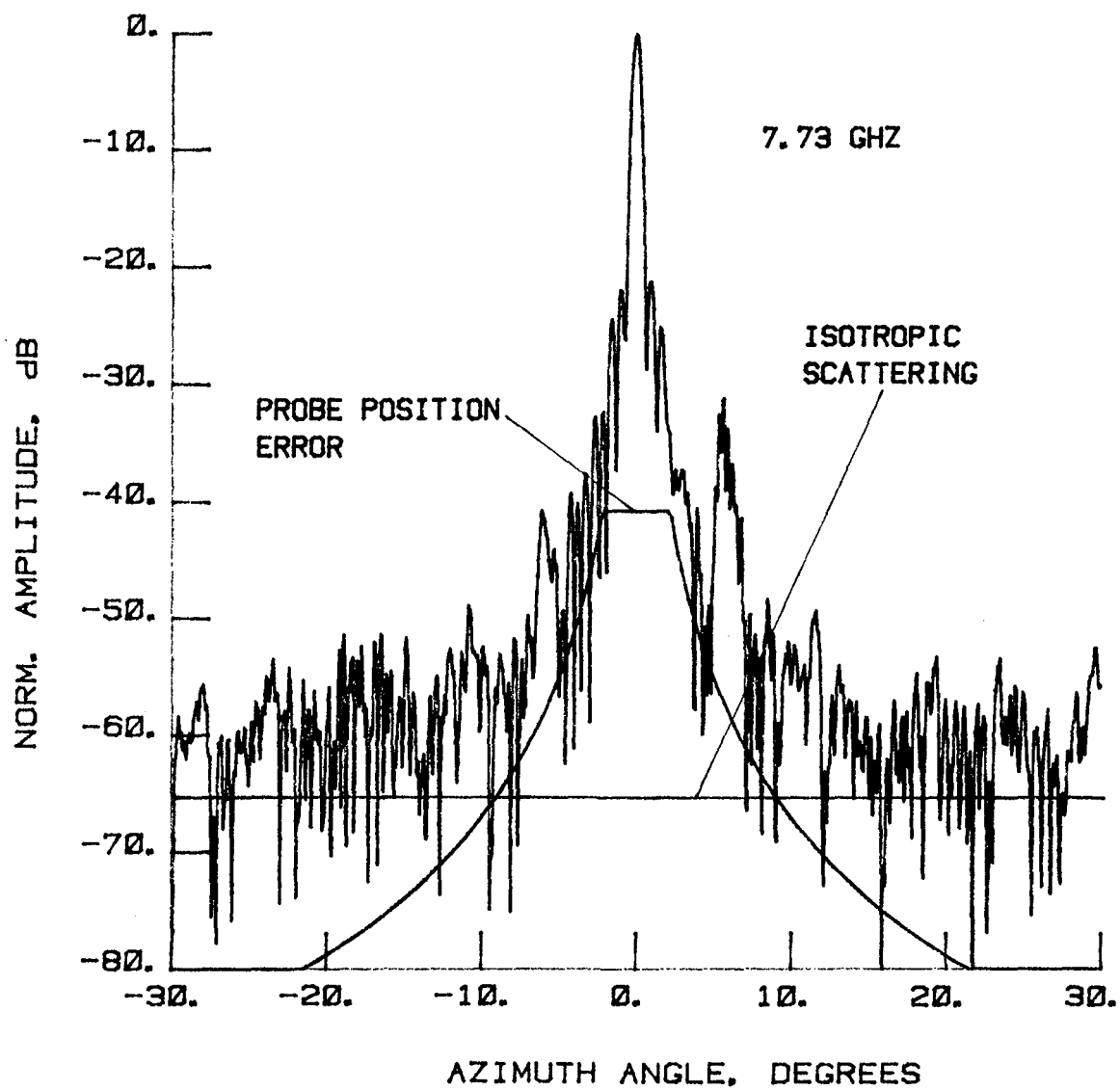
Figure 5-50 Error Envelopes Superimposed on Far-Field Patterns, 7.73 GHz, Test 1

89
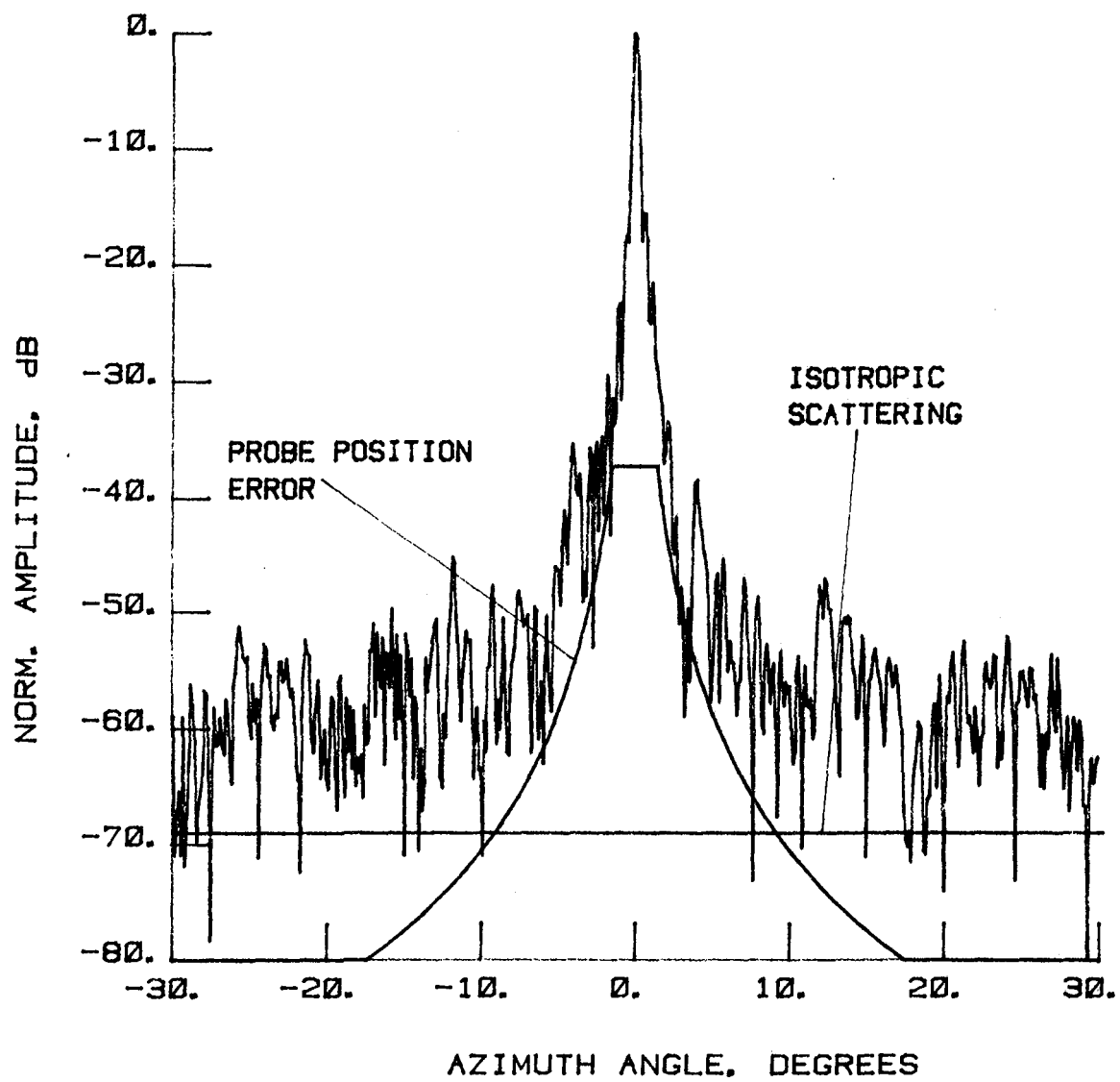
Figure 5-51 Error Envelopes Superimposed on Far-Field Patterns, 11.6 GHz, Test 4
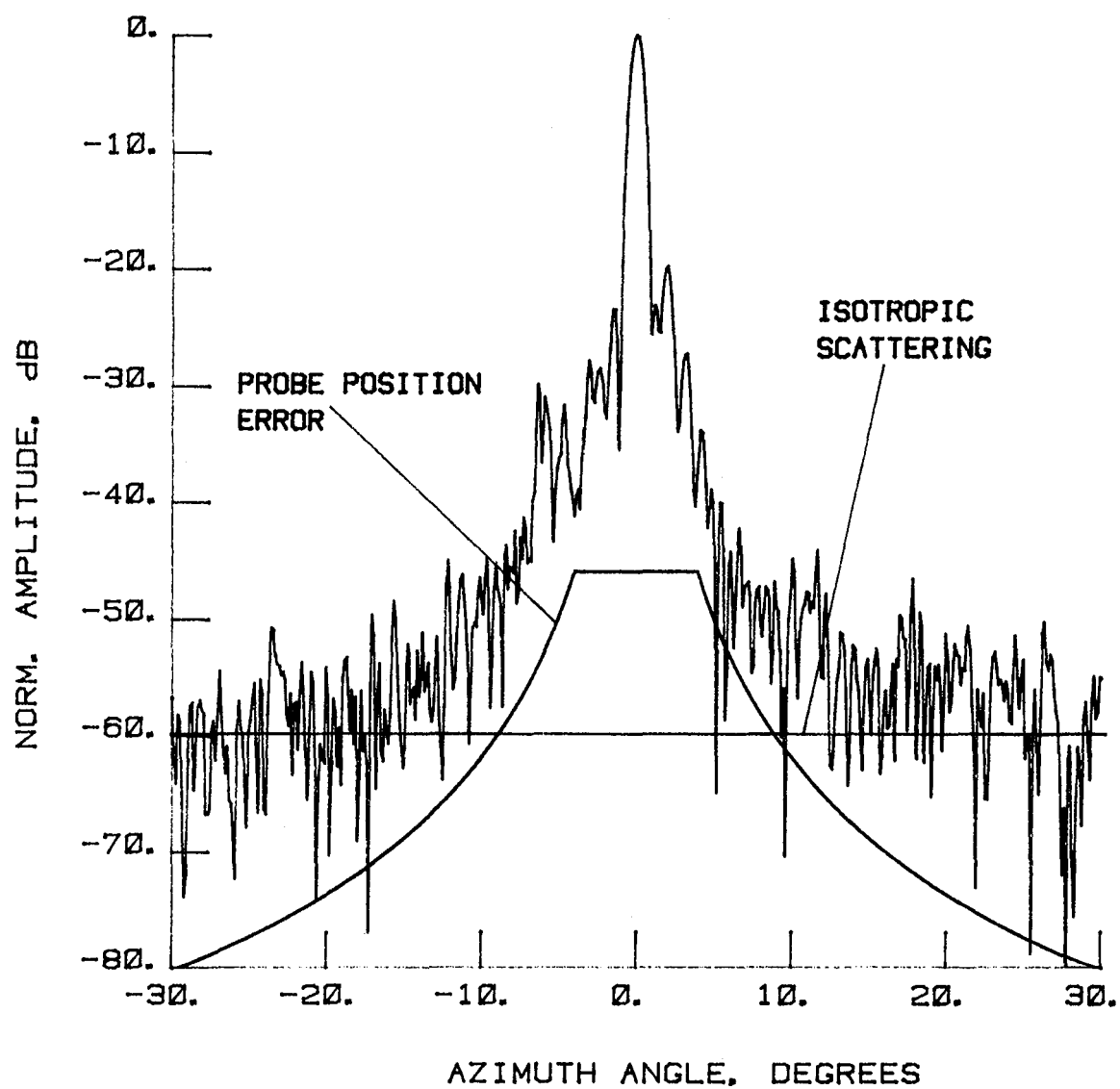
Figure 5-52 Error Envelopes Superimposed on Far-Field Patterns, 4.26 GHz, Test 12
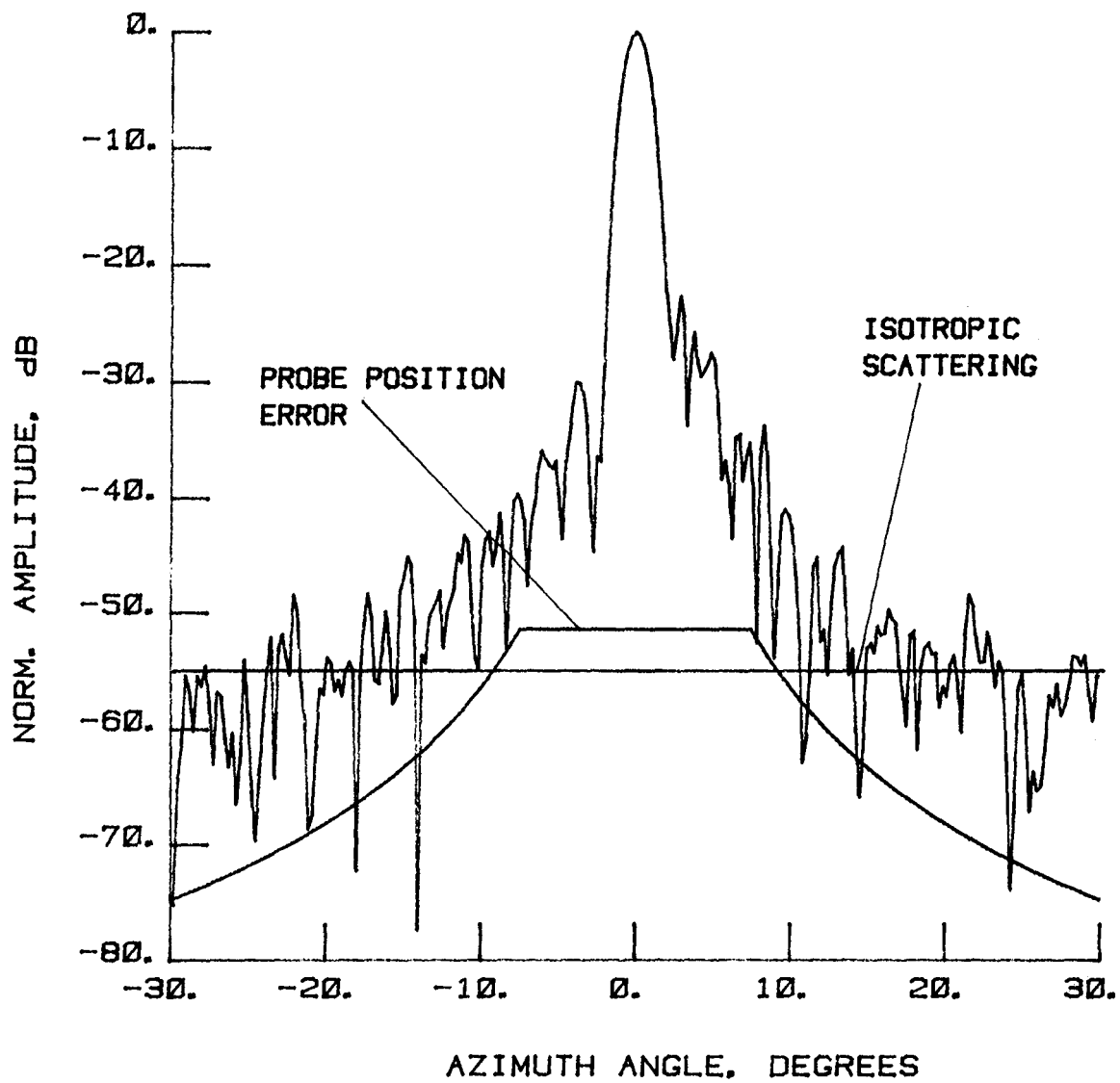
Figure 5-53 Error Envelopes Superimposed on Far-Field Patterns, 2.27 GHz, Test 5

92

6.0   SUMMARY AND CONCLUSIONS

Recalling introductory comments, the objectives of this program were to demonstrate that relatively high performance deployable antennas can be built and to demonstrate that the antenna performance can be accurately measured. The test results given in Section 5.0 of this report show that both objectives have been successfully achieved. For the second objective we have provided an error analysis to support claims of measurement accuracy. To further substantiate claims of accuracy, each test was continually analyzed and evaluated as it progressed. This parallel effort identified and solved problems, freeing the measurements of extraneous errors. The antenna and measurement system were continually monitored for problems, and several were identified and solved as the tests progressed. The diagnostics in Section 5.4 report some of the activity and results from the effort. The measurements performed showed a consistency typical of a refined and trouble-free measurement system. The near-field measurements presented in this report are state-of-the-art, representing years of technology development.

This program produced many important conclusions regarding the antenna and the measurement system. For the antenna the following conclusions are of importance:

o   Antenna performance is high.

o   First sidelobes are dependent on the quality of the reflecting surface. A -20 dB relative to the main beam peak is typical at 7.73 GHz.

o   Mechanical oscillations within the hoop column structure appear as errors in the wide-angle, low-level sidelobes, contributing little or no error to the main beam or principal sidelobes. The far-field angles are beyond approximately $\pm 10°$, and the levels are in the -50- to -60-dB range (Fig. 5-4). The angles and levels are somewhat dependent on plane of the far-field pattern and are, of course, dependent on operating frequency.

o   Pattern distortion resulting from beam steering is minimal.

o   Lobes generated by the parasitic apertures are minimal.

o   Cross-polarized far-field radiation occurs at low levels, typical of a quality antenna system.

For the measurement system the following conclusions are of importance:

o Accuracy has been achieved over wide dynamic ranges in the far-field in a large-scale system.

o Measurement stability/repeatability over extended periods has been achieved.

o Accurate gain measurements have been made.

o Near-field diagnoses have been demonstrated as powerful tools in optimizing antenna performance. The phase maps presented here using near-field measurements can shape mesh surfaces.

One of the more striking outputs from the measurements is the plot of scattering from the quartz cords supporting the hoop structure. Figures 5-48 and 5-49 demonstrate that the antenna can plot far-field patterns over dynamic ranges not available on far-field antenna range facilities.

Acceleration tests were conducted to verify that the antenna could sustain the near-field rotab translation and rotation-induced loads. The first acceleration measurements used two accelerometers. One was positioned at the base of the antenna on the rotational table (rotab), and the other was attached to the top of the antenna feed column. To simulate the effect of the heaviest feed, a 260-lb weight was temporarily installed on top of the feed column for these initial measurements. Because the heaviest feed weighed only 197 lb, the feed column was loaded to 130% of the maximum load present during the near-field measurements. Figure A-1 shows the configuration of the equipment involved in the acceleration tests. Figure A-2 shows a block diagram of the accelerometer instruments used for this measurement.
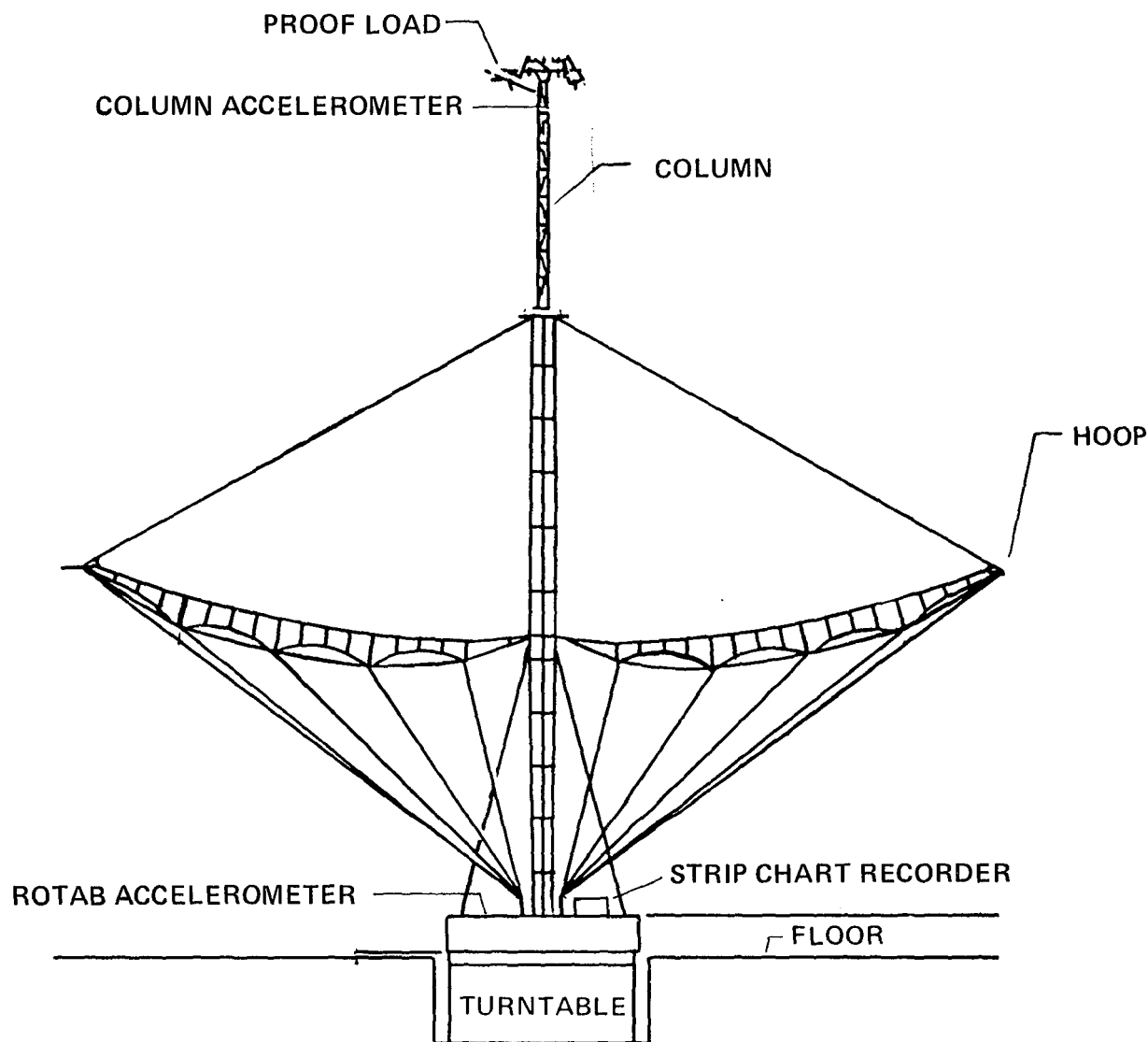
Figure A-1 Acceleration Test Configuration
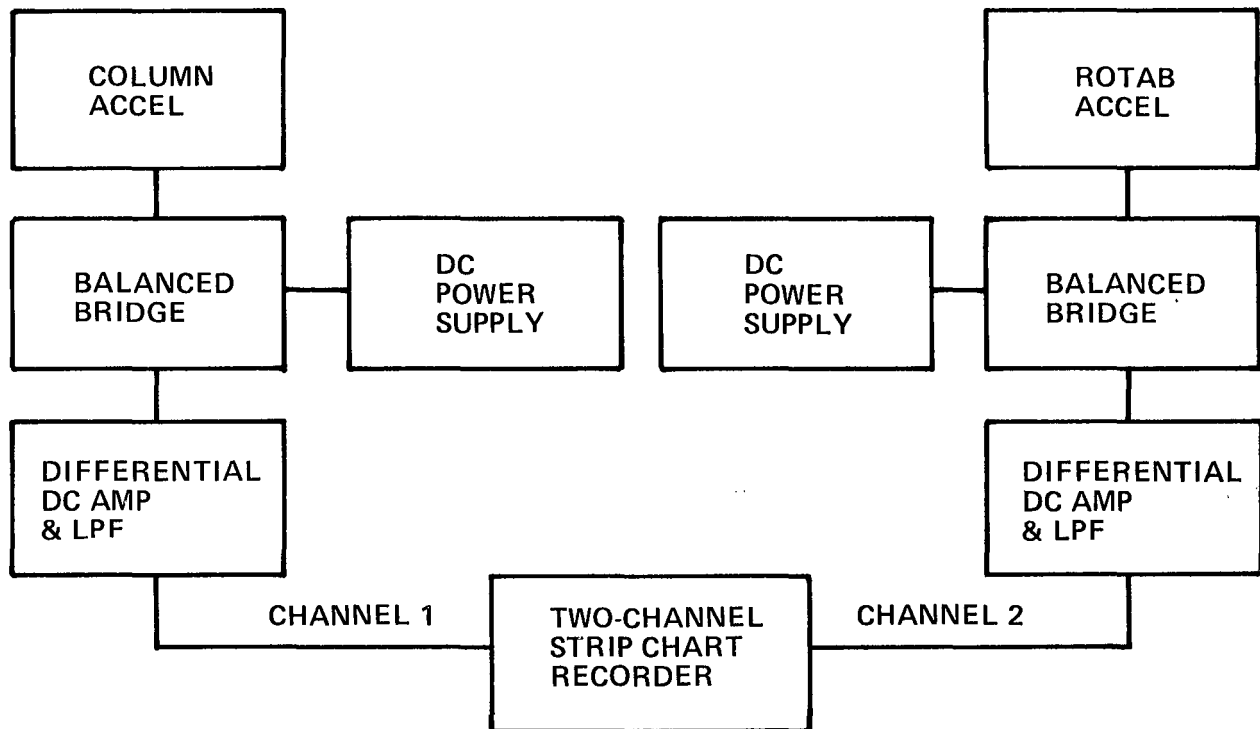
Figure A-2 Accelerometer Measurement Block Diagram

Altering the x-axis motor controller ramping function can change the acceleration of the rotab by rotating the index-speed-control variable resistor located on the front panel of the x-axis motor controller. This adjustment not only controls the acceleration of the rotab, but also controls the velocity of the rotab during x-axis translations. The velocity of the rotab is important because it has a large impact on the near-field data collection time.

The index speed control knob and its graduations are shown in Figure A-3. Minimum acceleration occurs when the control knob is rotated fully counterclockwise to Position 1. Turning the control knob fully clockwise to Position 10 will result in maximum rotab velocity and acceleration.

Two types of movement of the antenna occur during the near-field measurements: forward and reverse increments. Forward increments occur when the antenna is translated between data lines that are approximately one-half wavelength apart in the near-field array. Reverse increments occur when the antenna translation changes direction. For example, the antenna translates past the designated position by at least 0.005 in. and must reverse direction to arrive at the correct position. Another example occurs when the antenna reverses direction between the collection of two quadrants of data. The major difference between forward and reverse increments of antenna translation is that large acceleration is caused by gear backlash when the direction is reversed.

96
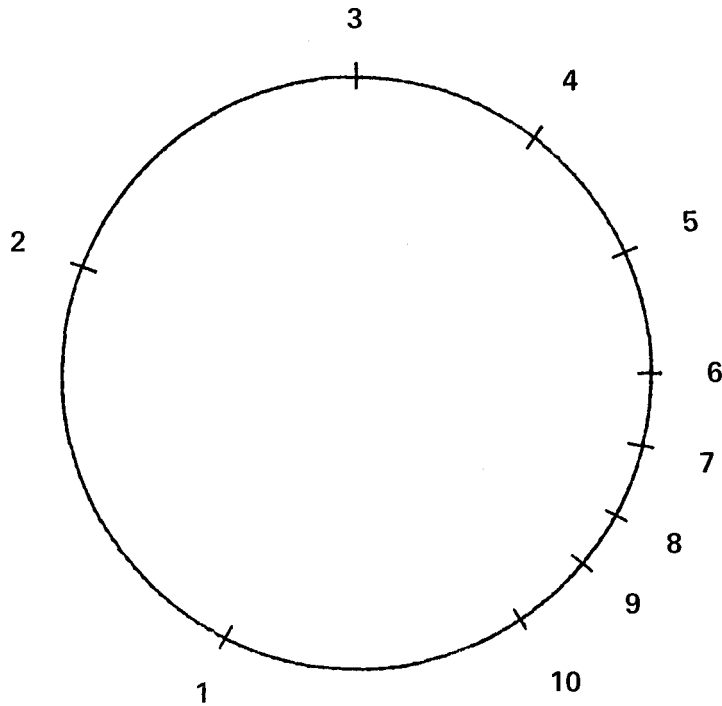
Figure A-3
X-Axis Motor Controller Index Speed Control Knob

Since the deployed antenna had not been subjected to acceleration tests in the past, the NFTL antenna translating system was initially set for minimum acceleration. At all times during antenna movement an NFTL staff member was positioned to turn off the power to the rotab drive motor if any potentially damaging situation occurred. Adjustment of the index-speed-control knob was restricted to two members of the NFTL Staff as a further control during the tests.

Using the theodolites to monitor the hoop movement and the accelerometer equipment to record and monitor the acceleration, several antenna movements were made at the minimum acceleration. It was determined that the acceleration and hoop movements were at safe levels and the index speed control was set to Position 2. The measurements were repeated for each position until the maximum allowable acceleration of 6 milli gs was obtained at Position 9. The sensitivity of the hoop movement measurements was determined to be the width of the theodolite cross-hairs, or approximately 10 mils. Hoop movement could not be detected until the index speed control was set to Position 6. At the speed (approximately 0.62 in./s) used in the actual near-field data collections, the hoop movement was approximately 30 to 50 mils.

Table A-1 shows a summary of the measurements that were performed. The accelerometer mounted at the top of the antenna feed mast showed acceleration amplitude curves similar to those recorded on top of the rotab. However, the accelerometer recordings on the antenna feed mast were slightly delayed in time and had a longer damping rate when compared to those on the rotab. Frequency of oscillation was approximately 3 Hz for the mast. An example move is shown for Index Control Position 6 in Figure A-4.

Table A-1
Initial Acceleration Measurements on the 15-Meter Hoop Column Antenna.

Step Size, in.	Approximate Maximum Speed	Direction	Index Speed Position	Peak Measured Accel, mg		Time, s	Hoop Movement, in.
				Column	Base		
0.4	0.14	same	1	0.7	1.0	5.7	*
0.8	0.16	s	1	0.7	1.0	10.0	*
1.3	0.17	s	1	0.8	1.0	15.0	*
2.6	0.15	s	1	0.5	1.8	35.8	*
0.2	--	s	2	1.0	1.0	--	*
0.4	0.15	s	2	--	--	5.3	*
0.8	0.18	s	2	0.8	1.0	9.0	*
1.3	0.19	s	2	1.0	0.5	13.5	*
2.6	0.21	s	2	1.0	1.0	25.2	*
0.1	0.11	change	3	2.3	2.5	1.8	*
0.4	0.21	s	3	1.0	1.0	3.8	*
0.8	0.20	s	3	1.0	2.0	8.0	*
1.3	0.22	s	3	1.0	2.0	11.8	*
2.6	0.24	s	3	0.6	2.0	22.0	*
0.4	0.20	c	4	2.2	3.0	4.1	*
0.4	0.17	s	5	1.0	1.5	4.6	*
0.4	0.21	c	5	3.0	3.5	3.8	0.015
0.4	0.20	s	6	1.8	1.3	4.0	0.020
0.4	0.23	c	6	3.8	4.7	3.5	0.030
0.4	0.23	s	7	3.8	4.7	3.5	--
0.4	0.21	s	8	--	2.5	3.8	--
0.4	0.29	s	9	--	5.5	2.8	--

* Less than 0.010 inches of movement
-- Not measured
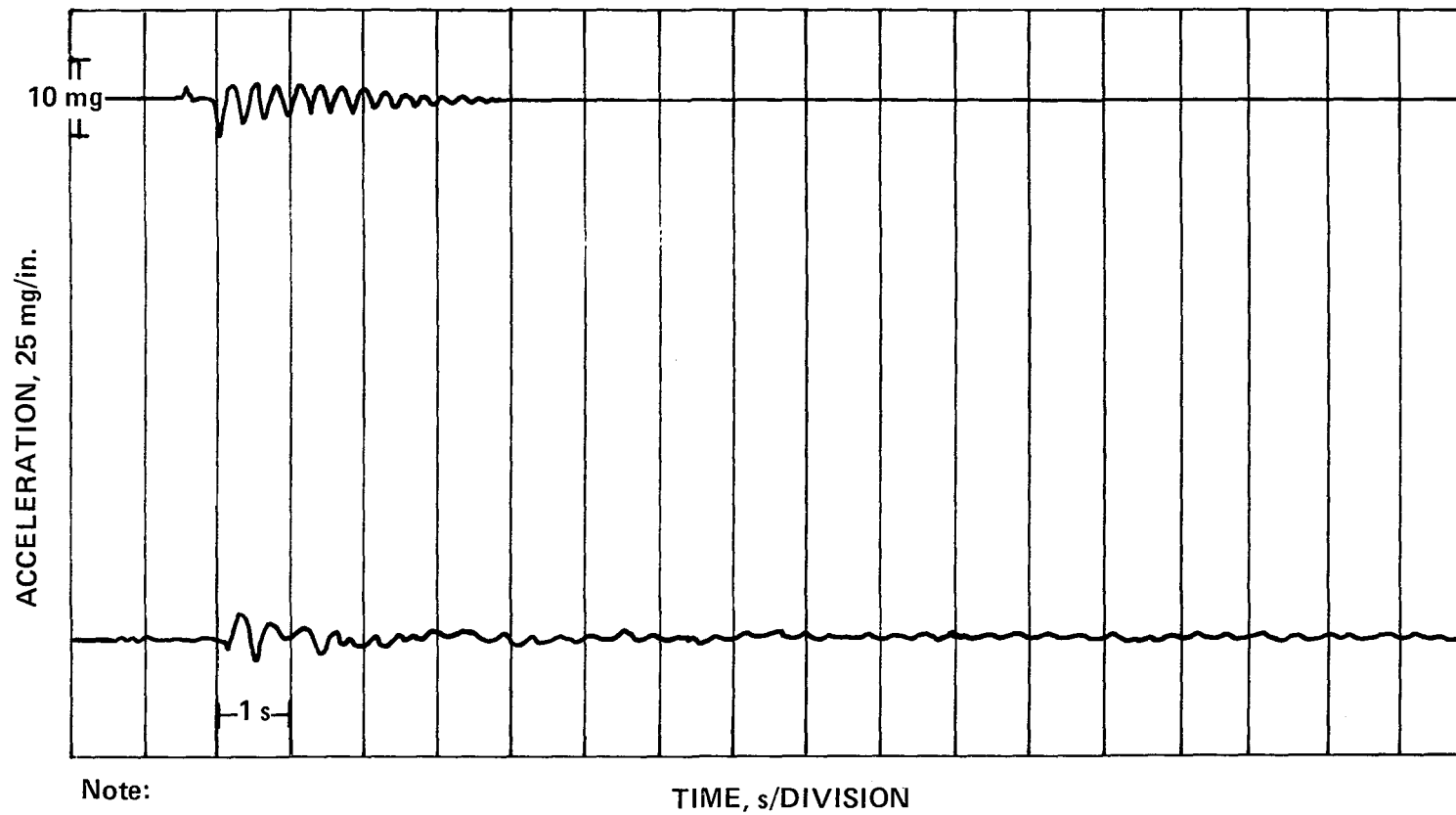
Note:
Top graph is of the rotab acceleration
while the bottom graph is of the top of
the feed column.

Figure A-4 Acceleration versus Time with Index Speed Control Set to Position 6

The actual near-field data collections used only one accelerometer. This accelerometer was mounted on the top of the rotab and needed to be rotated in the middle of each collection to keep its measurement axis properly oriented. Because the maximum magnitude of the acceleration was the major objective during the collections, the recorder speed was greatly reduced to save on the consumption of paper.

The distance of antenna translation had very little effect on the measured acceleration. A typical forward increment produced 3-4 milli g's of acceleration; 13 milli g's was the maximum recorded. An example of rotab acceleration versus time at 10 mm/minute and 40 mm/hour are shown in Figures A-5 and A-6, respectively.
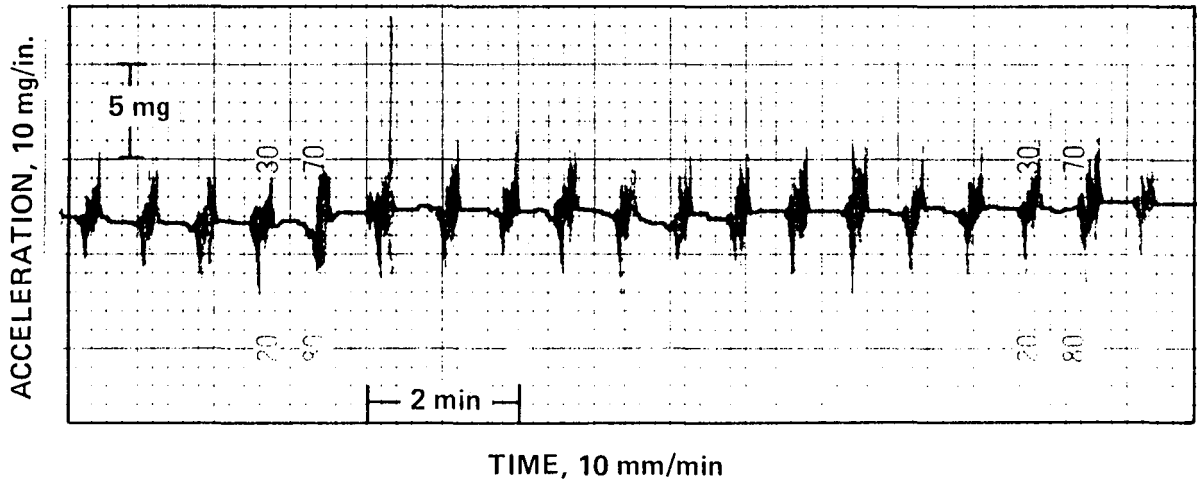

TIME, 10 mm/min

Figure A-5 Acceleration versus Time at Position 6 with Recorder Speed at 10 mm/min
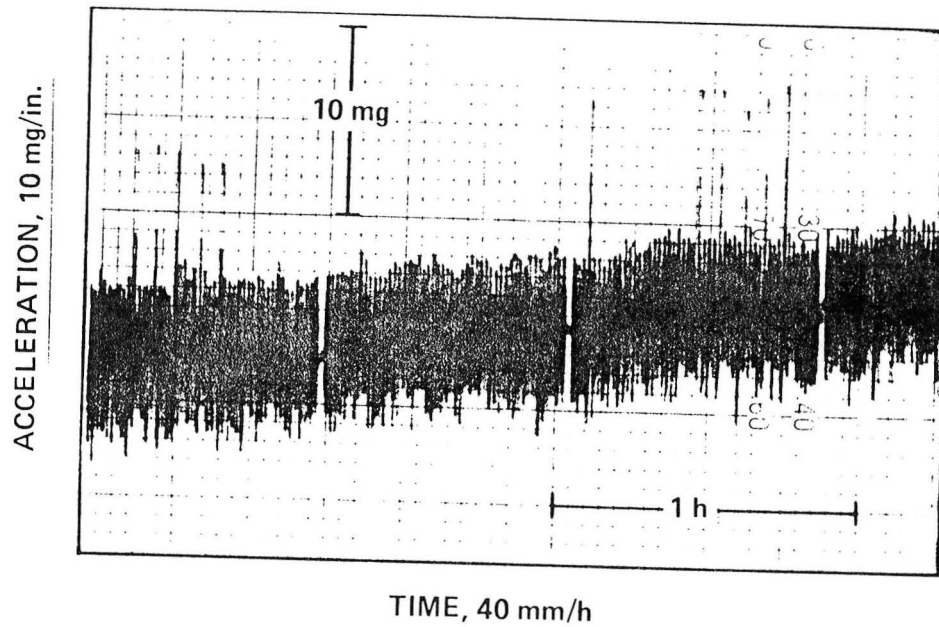
Figure A-6
Acceleration versus Time at Position 6 with Recorder Speed at 40 mm/h

This Page Intentionally Left Blank

APPENDIX B SYNOPSIS OF EQUIPMENT PERFORMANCE

The test program used many different types of equipment. A general
assessment of equipment performance follows, including a discussion of the
near-field laboratory, the test antenna, and program-related support
equipment (primarily man-lifting devices).

B.1 FAILURES AND ANOMALIES

To minimize the number of failures and technical uncertainties in the
near-field laboratory, a number of precautionary measures were taken
before the antenna arrived at the laboratory. The principal activities
included the following: The near-field system was configured for the
first test, system calibration was confirmed, and the first test was
rehearsed. At this point, the system had no technical problems relevant
to the test objectives.

After the antenna was deployed and the test program was underway, two
system failures occurred: (1) an RF mixer in the amplitude/phase meas-
uring receiver degraded over a period of hours and finally failed com-
pletely, and (2) an RF cable in the scanner fractured near the RF con-
nector (0.141 semirigid Teflon-filled copper cable). Some near-field data
was lost because of these failures, and the tests were repeated.

With respect to the antenna, no failures as such occurred. However, a
series of diagnostics was performed (as outlined in Section 5.4), and the
results from the diagnostics were used in measuring and optimizing antenna
performance.

The man-lifting devices used to gain access to the antenna came from two
sources, Martin Marietta Laboratories and local rental companies.
Experience showed that maintenance performed on rental equipment is
generally inadequate for the reliability needs of the program. One piece
of rental equipment failed with the potential for causing antenna damage.

B.2 TEMPERATURE VARIATION

Within the scanner room, the best temperature stability is a nominal
$+1°F$. This was the objective for the test program; however, the air-
conditioning system was turned off for some operations (such as the
photogrammetry), causing wider variations during those periods. These
temperature variations had no known influence on antenna performance.

During the near-field measurements the air-conditioning system was on, and temperature remained reasonably near the tolerance objective. Although it was not used or needed for this program, a capability for removing temperature drift from the measurements is available in the near-field system software.

B.3   EQUIPMENT USED IN THE ANTENNA DEPLOYMENT AND RESTOW OPERATIONS

The deployment, restow, and test activities required human access to every point on the deployment fixture and antenna. To meet all access needs within the confines of the scanner room, no single device had enough versatility. During the course of the program six different man-lifting devices were used, each having different lifting features. See Figure 2-4 for an example of lifting operation during stowed antenna hoisting operations.

APPENDIX C: NEAR-FIELD GAIN MEASUREMENT

_____

When an antenna such as the 15-Meter Hoop Column Antenna has its gain calculated during near-field testing, all terms in the following equation are measured:

$$[C-1] \quad G_a = \left(\frac{4\pi}{\lambda^2}\right)^2 \frac{|1 - \Gamma_m\Gamma_p|^2 |1 - \Gamma_a\Gamma_t|^2 |FFT_{max}|^2 \Delta x^2 \Delta y^2}{|1 - \Gamma_t\Gamma_m|^2(1 - |\Gamma_a|^2)(1 - |\Gamma_p|^2)|a|^2 G_p}$$

G_a = antenna gain

a = peak receiver level

$20 \log |a|$ = IL + RL

IL = insertion loss, difference in level between antenna radiated field and direct connection between Points 1 and 2

RL = field level measured by probe at position where insertion loss was measured

Γ_m = reflection from mixer side of Connection Point 2

Γ_p = reflection from probe side of Connection Point 2

Γ_a = reflection from antenna side of Connection Point 1

Γ_t = reflection from transmitter side of Connection Point 1

Δx = sample spacing along the x-axis
Δy = sample spacing along the y-axis
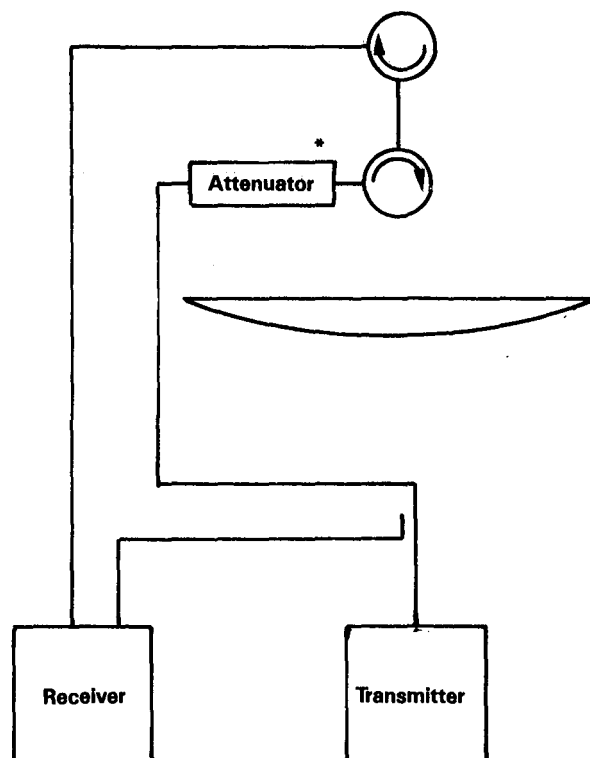λ = wavelength

FFT_{max} = Maximum obtained from Fourier transform of near-field data

G_p = gain of probe

Figure C-1 shows all the reflections and connection points mentioned in equation (C-1)
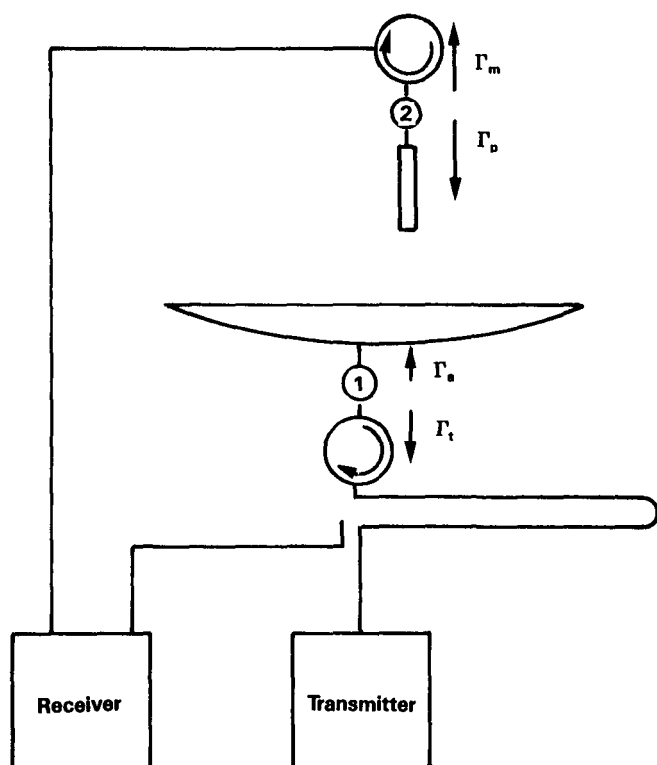
a Near-Field Measurement Circuit

b Insertion Loss Measurement Circuit

Figure C-1   Circuit for Test Antenna Gain Measurement

Note:
*Calibrated Precision Attenuator

Although the gain calculation from near-field data requires precision in all these measurements, the accuracy of values of probe gain and insertion loss will have the most significant effect on the accuracy of gain calculation. Both probe gain and insertion loss values require precise and repeatable RF connections and substitute standards into the RF system to calibrate absolute system response to a reference level. Therefore, the accuracy of the antenna gain becomes closely linked to the reliability of two pieces of RF hardware, the standard gain horn and a precision attenuator. To ensure reliability both devices have been repeatedly measured across their operating spectrum. Any variance in response could usually be attributed to connection repeatability for either device; both devices have flat responses with frequency implying that frequency interpolation results in negligible error. Therefore, gain measurements, based on the NFTL's past experience, have a 0.25-dB error budget for these two measurements, virtually the entire error expected in an antenna gain measurement.

Although calibrating an attenuator accurately for a specific frequency can be accomplished fairly simply as a network measurement, obtaining accurate values for probe gain needs much more care. The NFTL uses low-gain probes to measure near-field patterns of antennas. Although these probes allow accurate measurements to wide angles, the peak gain is relatively sensitive to reflections.

The NFTL determines peak gain by electrical measurement, comparing the response of a standard gain horn to the response of the NFTL open-ended waveguide probe. Figure C-2 shows the RF system configuration used to measure the probe gain. To obtain accurate repeatable data, the reflections were reduced wherever possible. These attempts to reduce reflections included placing an isolator behind the probe to eliminate reflections between the mixer and the probe. To guarantee maximum repeatability in the data, the same configuration was used for the probe every time, and the standard gain horn was connected to the same isolator as the probe. Both the horn and the probe were aligned mechanically and when mounted in the same bracket, their direction of peak, gain should coincide.

The antennas are then swept in frequency, and the amplitude of the response is recorded every 50 MHz. Gain of the probe is then determined by the equation:

[C-2] $$G_P = \frac{P_P\,G_H}{P_H\,(1 - |\Gamma_P|^2)}$$

P_P = Power received by probe

G_P = Probe gain

Γ_P = Complex reflection coefficient of the probe

P_H = Power received by standard gain horn

G_H = Gain of standard gain horn
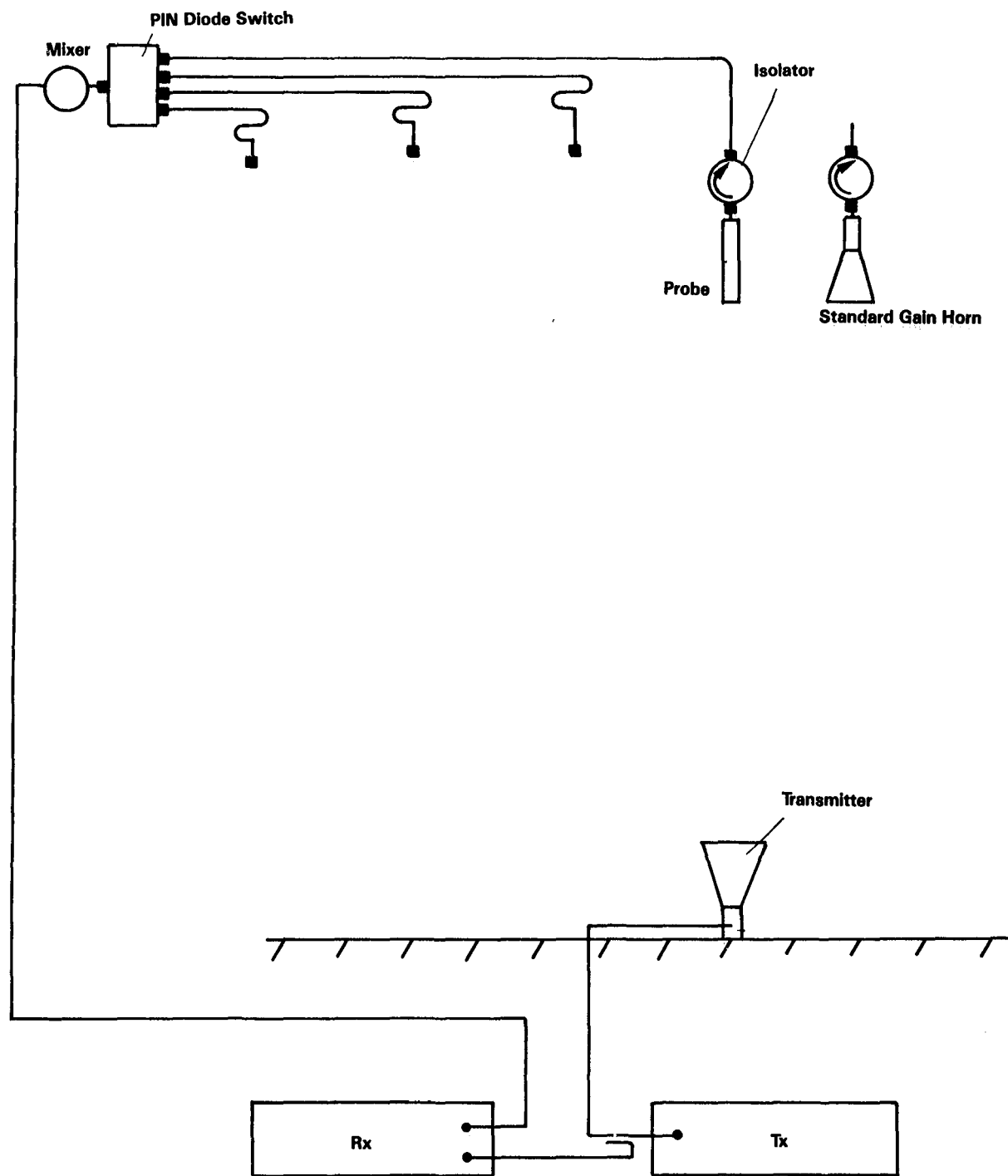
Figure C-2   Probe Gain Measurement Circuit

The only assumptions made in this equation are that (1) the field received by the horn comes strictly in the direction of peak gain, and (2) horn reflections cause negligible change in the response of the horn. These assumptions can cause a maximum of 0.05-dB error in probe gain measurements; also, the exchange of the two antennas in the system requires breaking an RF connection, which break can also cause 0.05-dB error, bringing the total probe gain error budget to 0.1 dB. This accuracy is typical for any measurement done by comparison. Attempting to measure gain more accurately for the probe is a meaningless effort, since the probe will have to be reconfigured and reconnected during every collection. Therefore, the primary source of improved accuracy in near-field gain measurement will come from increased accuracy of the insertion loss measurement.

This Page Intentionally Left Blank

D.1   THEORY OF PLANAR NEAR-FIELD

The planar near-field method of measuring antennas has been rigorously developed using the general solution to Maxwell's equations in a Cartesian coordinate system. In free space, these equations can be easily manipulated because the medium is linear and homogeneous and contains no sources. The manipulation produces the Helmholtz wave equation which, in the Cartesian coordinate system, can be solved by separation of variables. This separation of variables yields the result that a summation of functions can uniquely express the fields anywhere in free space. The equation below defines the fields E (x, y, z) on the near-field plane as (Ref 9)

[D-1] $\underline{E}(x,y,z) = \sum_{k_x} \sum_{k_y} \underline{A}(k_x, k_y) e^{jk_x x} e^{jk_y y} e^{jk_z z}$

where   x, y, and z are as defined for Figure 5-1.

k_x, k_y, and k_z are the x, y, and z components of the vector defining direction of propagation.

A (k_x, k_y) is the plane wave spectrum.

To determine $\underline{A}(k_x, k_y)$ the near-field method reverses the above equation, without loss of generality, yielding in the sampled case

[D-2] $\underline{A}(k_x, k_y) = \sum_x \sum_y \underline{E}(x,y,0) e^{-j(k_x x + k_y y)}$

which is a two-dimensional discrete Fourier transform.

This equation generates the set of functions, equivalent to plane waves, that uniquely defines the fields originating from the antenna anywhere in free space. To generate the fields at an arbitrary plane, the $\underline{A}(k_x, k_y)$ determined by near-field measurement is substituted into equation D-1, where the new z is entered into the equation. The change in z only affects one term in equation D-1 ($e^{jk_z z}$), and when z becomes non-zero, this term represents only a change in phase. The NFTL adds this phase change caused by the new z directly onto the spectrum and then inversely transforms the spectrum to yield the fields on the new plane.

111

D.2   Error in Projection Technique

In actual application, this projection has many possible error sources, but a high-quality near-field scanner can minimize these errors. The most basic assumption of near-field theory, that the measurements are made in free space, has always only approximated actual conditions. Because near-field scanners have to position over the aperture, and because no surface has a zero reflection level, there are always reflected signals in the measurement. A near-field scanner tries to minimize these signals by covering the entire scan surface with anechoic material. Reflections not only cause errors in the far-field, they can also generate errors in the projection because reflections represent sources above the aperture that cannot be removed from measured data. The NFTL has established in previous measurements that chamber reflections are well below isotropic over the frequencies tested for the 15-meter hoop column antenna. Also, these reflections tend to have minimal spatial coherency, implying that they will not rise to a level high enough in any projected plane to significantly perturb the fields radiating directly from the antenna.

The other major system measurement errors, probe positioning and accuracy of the electrical measurement equipment, have always shown minimal effect on the far-field patterns generated at the NFTL. These errors also have little influence on the field projection to the aperture because, like the reflections, they occur at low levels with respect to the antenna pattern and have no tendency toward spatial coherence. For projections on any near-field set of data, the level of these errors should be verified to establish an accuracy for the projection.

Along with system measurement errors, near-field measurements must also make several mathematical approximations that can cause errors. Scan plane truncation, one of these errors, occurs when a scanner measures fields over only a finite area. However, when the NFTL decreased the scan area over this antenna, it appeared that no significant power radiated beyond the aperture edge, implying that the effect of truncation error will not change either the near- or far-field patterns. In order to process near-field data, the data must be collected discretely, but if these samples are less than a half wavelength apart, the Nyquist theorem states that no information is lost because, in a source-free region, fields cannot vary faster than the highest transmitted frequency.

Two other errors that occur in the projection to the aperture fields arise from the type of antennas used in the measurement. Near-field measurements normally require probe compensation to obtain the true function spectrum. The NFTL probe compensates far-field data when it can cause significant errors in the data. For this program we did not compensate the far-field spectrum because the probe used for near-field measurements, an open-ended waveguide, does not modify the far-field spectrum significantly. Therefore, when the NFTL plots aperture fields for the antenna, the fields are equivalent to those measured by the NFTL probe at the aperture if it could scan the antenna at the aperture. The only remaining error source arises from projecting the fields through a region not completely source-free. For the 15-Meter Hoop Column Antenna the sources between the near-field scan planes and the aperture had minimal effect on the aperture fields. These sources, the direct radiation of the horn and reflections from the quartz support chord, could easily have been isolated if the effects had become significant. Sources in the near-field can be isolated simply by applying boundary conditions at the position of the potential source to remove the source. The projection to the aperture found no significant point sources by using this method to check for ray convergence.

This Page Intentionally Left Blank

REFERENCES

1.   John Hoover, Neill Kefauver, and Tom Cencich, Near-Field Testing of the 15 Meter Model of the Hoop Column Antenna, Volume II - Near- and Far-Field plots for the LaRC Feeds. NASA CR-178060, 1986.

2.   John Hoover, Neill Kefauver, and Tom Cencich, "Near-Field Testing of the 15 Meter Model of the Hoop Column Antenna, Volume III - Near- and Far-Field Plots for the JPL Feeds. NASA CR-178060, 1986.

3.   Allen C. Newell and Myron L. Crawford, Planar Near-field Measurements on High Performance Array Antennas," National Bureau of Standards, Technical Report, NBSTR 74-380, July 1974.

4.   Martin Marietta Denver Aerospace: "Measurements Error Analysis." Interim Progress Report, Project No. 1-28-1570.2379, June 1985.

5.   Martin Marietta Denver Aerospace: "Antenna Pattern Measurement Description." Interim Progress Report Project No. 1-28-1570.2379, April 9, 1985.

6.   E. Oran Brigham, The Fast Fourier Transform. Prentice-Hall, Englewood Cliffs, NJ, 1974, p 148.

7.   Allen C. Newell, "Upper Bound Errors in Far-Field Antenna Parameters Determined from Planar Near-Field Measurements, Part 2: Analysis and Computer Simulation." Lecture Notes for National Bureau of Standards Short Course, Boulder Colorado, July 1975.

8.   Arthur D. Yaghjian, Planar Near-field Measurement Techniques on High Performance Array, Part 1: Error Analysis for Nonscanning Beam Patterns. AFAL-TR-75-67, July 1974.

9.   Roger F. Harrington, Time-Harmonic Electromagnetic Fields. McGraw-Hill, Inc., New York, NY, 1961, p 143.

1. Report No. NASA CR-178059	2. Government Accession No.	3. Recipient's Catalog No.
4. Title and Subtitle Near-Field Testing of the 15-Meter Model of the Hoop Column Antenna, Volume I - Final Technical Report		5. Report Date March 1986
		6. Performing Organization Code
7. Author(s) John Hoover, Neill Kefauver, Tom Cencich, and Jim Osborn		8. Performing Organization Report No. MCR-85-640
9. Performing Organization Name and Address Martin Marietta Denver Aerospace P.O. Box 179 Denver, CO 80201		10. Work Unit No.
		11. Contract or Grant No. NAS1-18016
12. Sponsoring Agency Name and Address National Aeronautics and Space Administration Washington, DC 20546		13. Type of Report and Period Covered Contractor Report
		14. Sponsoring Agency Code 506-58-23-01

15. Supplementary Notes

Technical Monitor--Lyle C. Schroeder, NASA Langley Research Center
Hampton, VA 23665-5225

16. Abstract

This report documents the technical results from near-field testing of the 15-meter model of the hoop column antenna at the Martin Marietta Denver Aerospace facility. The antenna consists of a deployable central column and a 15 meter hoop, stiffened by cables into a structure with a high tolerance repeatable surface and offset feed location. The surface has been configured to have four offset parabolic apertures, each about 6 meters in diameter, and is made of gold plated molybdenum wire mesh. Pattern measurements were made with feed systems radiating at frequencies of 7.73, 11.60, 2.27, 2.225, and 4.26 (all in GHz). This report (Volume I) covers the testing from an overall viewpoint and contains information of generalized interest for testing large antennas. This volume discusses the deployment of the antenna in the Martin Facility and the measurements to determine mechanical stability and trueness of the reflector surface, gives the test program outline, and gives a synopsis of antenna electromagnetic performance. Three techniques for measuring surface mechanical tolerances were used (theodolites, metric cameras, and near-field phase), but only the near-field phase approach is included. The report includes an error analysis. A detailed listing of the antenna patterns are provided for the 2.225 Ghz feed in Volume III of this report, and for all other feeds in Volume II.

17. Key Words (Suggested by Authors(s)) Large space deployable antenna Near field antenna patterns Cable stiffened hoop/column Quad aperture, offset feeds	18. Distribution Statement Unclassified-Unlimited Subject Category 15
19. Security Classif.(of this report) Unclassified	20. Security Classif.(of this page) Unclassified	21. No. of Pages 123	22. Price A06

NASA Langley Form 63 (June 1985)